

## **ABSTRACT**

EMANUEL, AKO YANOMAA. A Novel Covalent Nanoglue and Whole Wafer Self-Alignment Based Upon Self-Assembled Monolayers. (Under the direction of Dr. Hans Hallen).

New methodologies for fabrication of multilevel packaging, particularly for RF signal analysis, are investigated. A new method for “gluing” silicon wafers together with a Self Assembled Monolayers (SAMs) based nanoglue are measured and discussed, as are methods to enable its use with non-conforming wafers. Results of bond strength measurements as a function of temperature and process will be presented. Surface area bonded is characterized by infrared (IR) imaging. We will also present a method of inducing self-alignment between whole silicon wafers with micrometer precision. This represents a qualitative departure from alignment of millimeter-sized objects as has been previously demonstrated. Self-alignment is induced by creating hydrophilic and hydrophobic regions on the wafers and using capillary forces of water in these regions to force the wafers to align with little to no outside influence. Results are characterized by IR imaging. Physical ideas that enable the whole-wafer alignment such as flow channels, elimination of secondary minima, large central capture areas and small edge features are discussed. The possibility of aligning with the covalent nanoglue materials as the alignment drivers is discussed.

© Copyright 2012 by Ako Yanomaa Emanuel

All Rights Reserved

A Novel Covalent Nanoglue and Whole Wafer Self-Alignment Based Upon Self-Assembled Monolayers

by  
Ako Yanomaa Emanuel

A dissertation submitted to the Graduate Faculty of  
North Carolina State University  
in partial fulfillment of the  
requirements for the degree of  
Doctor of Philosophy

Physics

Raleigh, North Carolina

2012

APPROVED BY:

---

Hans Hallen  
Committee Chair

---

Keith Weninger

---

David Aspnes

---

Michael Paesler

## **DEDICATION**

I would like to dedicate this work to my wonderful and supporting family: Shawn Anderson, my husband, who is my true love, and who kept me going; Dr. Phyllis Briggs-Emanuel, my mother, who always asked if I were working on my thesis and in whom our one true home resides; Dr. Devon Briggs, my older brother, and the keeper of the spirit and pride of the family; Agyei Briggs-Emanuel, my younger brother, and the heart of the family; Mary Lowe, my grandmother, who was the visionary who started us all on the educational path; and Dr. Lezmore Emanuel, my father, who taught us pride in our heritage and acceptance of who we are.

## **BIOGRAPHY**

Isaac Asimov once compared scientists to toddlers who never learned to stop asking, “Why?” Sometimes explaining that a black hole with an event horizon that is parsecs in diameter is actually a 2 inch white hole spewing antiparticles is just not enough for some 3-year-olds. Curiosity is an undeniable impetus, but one other ingredient is needed...stubbornness. Another great sage, Garfield the Cat, offers the aphorism, “It’s amazing what you can accomplish when you don’t know what you can’t do”. Challenging the unknown and the unexplored is endlessly intoxicating. Let’s not forget the naysayers; bless them all. “You can’t do that” and “you shouldn’t do that”. What greater motivation could a scientist ask for?

## **ACKNOWLEDGMENTS**

I would like to acknowledge my friends and classmates, without whom I would not have had nearly as much fun, nor learned as much physics as I did: Trey Walker, Frisco Rose and Keith Hayward.

I would also like to acknowledge all the excellent teachers I have had at North Carolina State University, who truly followed the spirit of not just scholarship, but also the true meaning of teaching.

## TABLE OF CONTENTS

List of Tables .....	vii
List of Figures .....	viii
Chapter 1: Introduction .....	1
1.1: Introduction .....	1
1.2: Goals .....	8
1.2.1: Self-Alignment .....	8
1.2.2: Bonding .....	6
1.2.3: Integration .....	7
1.3: RF Antenna Array Background .....	9
1.4: Conclusion .....	15
Chapter 2: Materials and Oxidation .....	17
2.1: Introduction .....	17
2.2: Self-Assembled Monolayer Deposition .....	18
2.2.1: General Theory of Deposition .....	21
2.2.2: Wafer Cleaning .....	22
2.2.3: 10-Undecenyltrichloroxysilane Deposition .....	23
2.2.4: PEDDA Deposition .....	24
2.2.5: SAMs Modification .....	25
2.3: Ozonation .....	28
2.3.1: Ozone Generation .....	31
2.3.2: Ultraviolet Light Generation of Ozone .....	31
2.3.3: Corona Discharge Ozone Generation .....	32
2.3.4: Ozone Delivery Apparatus .....	33
2.3.5: Ozone Generator .....	36
2.4: Nylon 6-6 .....	37
2.5: Polymerization .....	42
2.6: Force Table Design .....	43
2.7: Conclusion .....	45
Chapter 3: Bonding with Covalent Glue .....	48
3.1: Introduction .....	48
3.1.1: Bare-SAM Bonding Difficulties .....	51
3.1.2: Bonding Requirements .....	55
3.2: Thin Silicon .....	56
3.3: Intermediary bond .....	58
3.4: Low Magnification View of the Bond .....	59
3.5: High Resolution View of the Bond .....	63
3.6: Producing a Nylon Bond .....	66
3.6.1: Condensed Nylon .....	68
3.6.1.1: Results for Bonding with Condensed Nylon .....	70
3.6.2: Nylon Immersion .....	71
3.6.2.1: Results for Bonding with Nylon Immersion .....	72

3.6.3: Clamped Nylon Bonding .....	73
3.6.3.1: Results for Bonding with Clamped Nylon .....	74
3.6.4: Spun-On Nylon .....	81
3.6.4.1: Results for Bonding with Spun-on Nylon .....	82
3.6.5: Bonding Intermediary – Kevlar .....	85
3.6.5.1: Results for Bonding with Kevlar .....	87
3.7: Conclusion .....	89
Chapter 4: Self Alignment of Wafers .....	91
4.1: Introduction .....	91
4.2: Statement of the Problem .....	93
4.3: Surface Energy .....	93
4.4: Energy Minimization .....	99
4.5: Change in Area .....	105
4.6: Contact Angle Model and Data .....	111
4.7: Measurements of Water Interface .....	114
4.8: Measurement of the Unaligned Wafers Interface .....	120
4.9: Conclusion .....	121
Chapter 5: Alignment Measurements .....	123
5.1: Methods of Alignment Measurement .....	123
5.2: Force Table Redesign .....	126
5.3: Mask Design .....	127
5.4: Alignment Pattern Fabrication .....	129
5.5 Theoretical Calculations of the Alignment Force .....	130
5.6: Experimental Procedure .....	133
5.7: Force vs Displacement .....	135
5.8: Accuracy of Measurement .....	143
5.9: Combining Alignment and Covalent Nanoglue .....	147
5.10: Conclusion .....	149
References .....	150

## LIST OF TABLES

Table 4.1: Measured values of the surface tension, based on concentration of ethanol to water [Vazquez, 1995].....	112
Table 4.2: Calculation of the surface tension based on contact angle, and concentrations of ethanol in water .....	113
Table 5.1: Lengths of the different areas of the pattern.....	131
Table 5.2: Prediction of restoring force.....	132

## LIST OF FIGURES

Figure.1.1: The wafer layers shown are the minimum needed for a functional RF array element. This compact device is the end goal of our study .....	1
Figure 1.2: Frames of a self-assembly event. Part dimensions are 400X400X15 $\mu\text{m}$ . <i>U. Srinivasan, D. Liepmann, and R.T. Howe, J. Microelectromech. Sys</i> <b>10</b> (1) 17-24(2001).....	5
Figure 1.3: With SAMs coating the wafers, the surfaces of these wafers have the proper termination to allow an intermediary to perform the task of bonding.....	6
Figure 1.4: The brick architecture consists of several “sticks” connected to a back-plate and electrically connected to the RF, logic, and DC manifold. Fourikis, Nicholas. (1997). <i>Phased Array-Based Systems and Applications</i> .....	10
Figure1.5: Tile architecture. Fourikis, Nicholas. (1997). <i>Phased Array-Based Systems and Applications</i> .....	11
Figure 1.6: JPL’s membrane antenna has demonstrated aerial densities of less than 2 $\text{kg/m}^3$ which include structure and aperture. This is in comparison to 20 $\text{kg/m}^3$ for the phased array used in the Shuttle Radar Topography Mission (SRTM). <i>Antennas and Propagation Society International Symposium, 2005 IEEE</i> .....	12
Figure 2.1: SAMs form even, predictable layers on silicon and other substrates.....	20
Figure 2.2: The oxidation by ozone of 10-UTS. There is an optimum time of exposure where the carbon double bond is broken, but the layer is not stripped away, at 150s. For this UV/ozone cleaner, the time was $\sim$ 200 seconds. However, this leaves little room for error. <i>Synthesis of Carboxylic Acid Monolayers by Ozonolysis of 10-UTS SAMs</i> , Hallen, M., Hallen, H. (2008).....	28
Figure 2.3: Ozone is a triatomic molecule of oxygen. This configuration is highly unstable and has a tendency to break down to diatomic oxygen and an oxygen atom.....	29
Figure 2.4: Ozone attacks the double bond of carbon.....	29
Figure 2.5: The ozonide disintegrates into other molecules, which, when exposed to water, can yield carboxylic acid.....	30
Figure 2.6: The oxidation of vinyl can take many paths to come to carboxylic acid.....	30
Figure 2.7: Corona discharge is a reliable method for producing ozone.....	32

Figure 2.8: The old apparatus versus the new configuration for the oxidation of vinyl to form carboxylic acid. The UV LEDs were replaced by an ozone generator, which was safer and easier to use.....	35
Figure 2.9: Corona discharge apparatus. This design was not completed, because of a failure of the high voltage source.....	36
Figure 2.10: The layer stripped away versus the time of exposure to ozone. The optimal time fell at ~ 11.5 minutes.....	37
Figure 2.11: Condensation reaction of hexamethylene diamine and adipic acid.....	39
Figure 2.12: Hexamethylene diammonium adipate. This nylon 6,6 salt represents the minimum energy configuration.....	41
Figure 2.13: Polymer chains can fold into quasi-crystalline formations called lamella. From the University of Southern Mississippi.....	42
Figure 2.14: The vacuum collar was replaced by an L-rail stage. Because the stage used the same mounting as the collar, the stage height could also be controlled.....	44
Figure 2.15: When the motor of the table is activated, the measuring program begins simultaneously. The force is measured until the nanoglue breaks or the pulling block comes off.....	44
Figure 3.1: Two different SAMs with amine and carboxylic acid terminations are used to construct the bond.....	48
Figure 3.2: a) The SAM-only bond was achieved in localized, millimeter-sized patches. The strength of the bond exceeded the Si-Si bonds. In 3.2b, dark-field illumination shows where the silicon was removed from one of the samples as a result of the rupture of silicon rather than the bond. The size of the bonded regions is a few millimeters to a side. This is likely due to the fact that the SAM layers were only in contact over such small regions due to their short length and lack of perfect flatness of the wafer .....	50
Figure 3.3 Surface roughness of silicon on the nanometer scale.....	51
Figure 3.4: Monomer molecules are free to move. All documentation on nylon formation is for free molecules. Conventional recipe for nylon requires an autoclave. Such conditions may be unsuitable for wafers.....	52

Figure 3.5: A cut-away example of thin wafer use in the bonding process. SOI wafers are thin enough to conform to the surface of the thicker bottom wafer, eliminating the need to apply pressure for bonding..... 57

Figure 3.6: The SAMs have the same functional groups as the constituent monomers of nylon; therefore, nylon can be used as an intermediary to fill in the gaps between the SAMs that are caused by the roughness of the wafers..... 58

Figure 3.7: Silicon is transparent to infrared in the 1.5 to 8 micron range. *Almaz Optics, Inc.*..... 60

Figure 3.8: The original, low power microscope that was used to view bond. The IR filter was removed and the stage was replaced with a glass platform and incandescent light source..... 61

Figure 3.9: The bonding can be viewed when infrared light is shone through double-side polished silicon. The patterns of light and dark are the result of variations in thickness of the nylon between the wafers..... 61

Figure 3.10: Sudden changes in the pattern may be due to air pockets..... 62

Figure 3.11: To avoid the interference effects, a higher power microscope, with a shorter focal length was used. This high magnification microscope is capable of discerning the interfaces between the nylon and the wafer, and of differentiating between the top and bottom of the 50 micron thick wafers..... 64

Figure 3.12: In this picture interface defects in an arc through the middle of the image. In the top image, a) the discoloration on the top of the wafer is in focus, while the defects are out of focus. Below, in b) the discoloration is out of focus, and the defects are in focus. The thickness of the wafer is approximately 50 microns. The arc of defects in the interface is delineated by the rectangles. This interface is thin enough that we see the whole interface at once..... 65

Figure 3.13: A plot of the force vs displacement pulling data. .... 67

Figure 3.14: In 3.14a, the solution is dilute. Figure 3.14b shows the condensate of nylon at the edges of the top wafer before heating to polymerization temperature..... 68

Figure 3.15: The condensate has turned black at slightly above polymerization temperature. The wafers have been pulled, and the force to break them apart measured..... 69

Figure 3.16: The initial force required to pull the wafers apart peaked at ~ 9.2 N within 1 mm, seen in 3.14 a. A second sample required a force of ~ 11 N, as shown in 3.14 b. The

condensed glue bonded in the same manner as a conventional glue, which is unsuitable for the purposes of this study. Though the strength of the bond was significant, this line of experimentation was not pursued..... 71

3.17: The top wafer was immersed in a 0.0295 M solution of nylon, then placed on the bottom wafer and held in place by a 3 kg weight. Immersion proved ineffective as a method of bonding..... 71

Figure 3.18: The bonding due to nylon immersion was not consistent, ranging from 1 to 12 N of force required to break the bonding..... 72

Figure 3.19: a) The solution is placed, in dilute form, onto the bottom wafer and b) the top wafer is clamped into place with an alligator clip. The solution is then allowed to dry in air to form a thin nylon salt between the layers before polymerization..... 73

Figure 3.20: a) While clamped, the solution is allowed to evaporate overnight, so that the nylon forms a salt between the wafers. b) Then, still clamped, the nylon is heated to 200°C..... 74

Figure 3.21: The force to break this bond was consistently higher than previous methods, centered around 4 and 9 N. This method proved more reliable and easier to fabricate. One pulling sample came off at 24 N..... 75

Figure 3.22: The force required to break the Si wafers apart was greater than the strength of the glue holding the pulling block on to the wafer. The cantilever sensor topped out at 24 N..... 75

Figure 3.23: A separated sample in a) dark field and b) bright field illumination..... 76

Figure 3.24: The bond was strong enough to break the silicon of the one of the wafers, leaving fragments still bonded to the opposite wafer..... 76

Figure 3.25: Different amounts of illumination show the depth of detail of the broken bond in the separated wafers..... 77

Figure 3.26: Identical patterns are a strong indicator of covalent nanoglue..... 78

Figure 3.27: a) A temperature-dependent measurement was conducted to determine the threshold temperature for this type of bond. The bond begins to break down at around 170 deg C. b) There is a correlation between the temperature dependent strength of the bond and the yield stress studied by the Polymer Research Group. There is a downward trend in force due to a rise in temperature..... 79

Figure 3.28: The graphs show instances where the bond did not break, but rather the pulling block, glued onto the top wafer, came off first.....	80
Figure 3.29: Spun-on nylon gave as good a bond as clamped nylon, while yielding the thinnest layer. The top pictures, a) and b) show the actual crystallization of the nylon salt, and the bottom image c) shows a rainbow pattern where the salt has polymerized to a nylon layer.....	82
Figure 3.30: The thicknesses of the spun on nylon, measured with an ellipsometer, at different concentrations. Very thin layers of nylon were achieved, particularly with lower concentrations, but the lowest did not give a good bond.....	83
Figure 3.31: a) Spun-on nylon was not as successful as clamped nylon, giving pulling forces mostly between 2 and 5 N. b) In one instance the pulling block came off, at 13 N, as shown below, but this does not give a definitive measure of comparable strength to dropped nylon.....	84
Figure 3.32: These molecules are the monomer constituents of Kevlar. The end functional groups are the same as nylon monomers, and the intervening structure is a benzene ring. The ring changes the properties of the monomers from those of regular nylon, making Kevlar more difficult to use.....	85
Figure 3.33: Kevlar forms rigid sheets through a form of hydrogen bonding between the long chains. Chemical Structure of Kevlar. <i>Cacycle, 2005</i> .....	86
Figure 3.34: Terephthalic acid will partially dissolve in sulfuric acid.....	87
Figure 3.35: Results for Kevlar pulling. Kevlar did not give a satisfactory bond, due to the insolubility of the terephthalic acid. The solvents required were too hazardous for practical use. The bonds were not as strong as supposed, and polymerization was not assured, due to the fact that terephthalic acid sublimates at high temperatures.....	88
Figure 4.1: Frames of a self-assembly event. Part dimensions are 400X400X15 $\mu\text{m}$ . <i>U. Srinivasan, D. Liepmann, and R.T. Howe, J. Microelectromech. Sys</i> <b>10</b> (1) 17-24(2001).....	91
Figure 4.2: Wafer on wafer alignment, measuring static friction and the force exerted by dry hydrophilic and hydrophobic regions.....	92
Figure 4.3: A representation of the surface tension within a water droplet on a hydrophobic surface. The molecules near the surface do not have attractive forces on the exposed side.....	94

Figure 4.4: Without the simplifying assumption that the vertical separation between the wafers is constant, the height decreases as the wafer is offset to preserve consistency in the volume of fluid.....	95
Figure 4.5: A representation of the radii of curvature of a liquid surface.....	97
Figure 4.6: A graphical representation of the surface of the alignment fluid between the top and bottom alignment wafers. The straight edge $l$ is in the $y$ -direction, and the differential segment $ds$ is in the $x$ - $z$ plane.....	100
Figure 4.7: Calculated shape of the water surface according to the energy minimization process.....	103
Figure 4.8: The coordinate system is oriented so that the wafer offset force can be shown completely in the $x$ direction.....	104
Figure 4.9: An illustration of wafers being pushed out of alignment. a) Only the water surfaces that make an angle to the vertical contribute to the alignment force. b) Both horizontal and vertical displacement, but edges parallel to the motion do not contribute.....	105
Figure 4.10: The water surface, once it reaches the “elastic” extent of the curved surface, begins to flatten out and the area of the surface begins to increase, thereby increasing the surface energy.....	107
Figure 4.11: Calculation of the increase in area with horizontal displacement, given a fixed height.....	107
Figure 4.12: Assuming that the vertical separation between the wafers is constant, as the horizontal component changes, the area increases.....	108
Figure 4.13: Polar space coordinates are convenient to describe the fluid edge as it is displaced in $x$ and $y$ . The displacement of the wafer due to the force table is $R_{disp}$ .....	109
Figure 4.14: A comparison of the displacement of the water edge in $x$ to the displacement in $x$ and $y$ .....	110
Figure 4.15: Images of contact angles for solutions of ethanol in water, by volume, on a hydrophilic surface (PEDA). Increasing the concentration of ethanol results in a decrease in contact angle. Below 60 %, a meaningful contact angle could not be discerned.....	114
Figure 4.16: The pale line that advances with the change in focus is the water edge being measured. After a certain point, the water edge is occluded.....	115

Figure 4.17: Focus marks were scored into the glass slides in 4.17a. In 4.17b, the curve was plotted to ascertain the shape of the water edge..... 116

Figure 4.18: The white line shows the water edge that advances as the focus to the microscope is adjusted. Above is a comparison of the water edge measurement and the calculated shape predicted by energy minimization. There is reasonable agreement between the shapes..... 117

Figure 4.19: The water is confined to one side of the image by the hydrophilic and hydrophobic regions. The shape of the water edge should be the same, however..... 118

Figure 4.20: The pale line that marks the advancing water edge within the complete shadow can be seen to move to the forward edge of the shadow, but disappears after the halfway point. The graph shows another approximate shape of the water edge, but the shape is incomplete..... 119

Figure 4.21: When the curve is misaligned, the water edge seems to take on a shape that suggested an almost flat line. Difficulties in measurement included evaporation of the fluid, as seen here in successive images..... 120

Figure 5.1: These patterns have a large initial capture area and narrow flow channels. Large corner areas allow the fluid to collect, and the small flow channel features let the fluid drain completely when alignment is achieved. This is shown when the wafers are off-set more than one time and eventually fail to realign. For experimental data collection, the final flow channels have been eliminated, so that realignment can be measured several times. The removal of these edge channels slows the release of water from between the wafers, but does not stop it completely..... 123

Figure 5.2: Illustration of buoyancy of silicon wafer due to the alignment fluid. The fluid supports the weight of the top wafer in this simulation..... 124

Figure 5.3: The force table was rebuilt to its original configuration to measure the alignment force between the wafers with the intervening fluid acting as the driving mechanism... 126

Figure 5.4: Alignment patterns from previous study by Walker. There are actually 21 identical patterns in this figure, laid out to maximize the ‘real estate’ of a 3” wafer..... 127

Figure 5.5: The early designs for the mask with flow channels eventually evolved into the angled pattern for greater precision in mask fabrication..... 128

Figure 5.6: The alignment pattern has been developed on the SAMs coated wafer. The silver portions are the silicon with SAMs, and the reddish portions are the photoresist. This wafer is ready to be ozonated to make the pattern active..... 130

Figure 5.7: Lengths of the alignment pattern. Many of the lines are at 45° to the edges, so that both the x and y cosines must be taken into account. Below are the measurements of the periphery of the different shaded areas..... 131

Figure 5.8: The force equation in Chapter 4 (Eqn. 4.43) predicted a relationship of direct proportionality between the surface tension and the force of alignment, akin to a spring restoring force..... 132

Figure 5.9: Portions of the pattern can be seen here, as the hydrophilic surface holds on to the DI water temporarily. .... 134

Figure 5.10: DI water (0 concentration of ethanol). a) The top graph is the actual raw data, and b) the bottom graph shows the behavior of the data using a rolling average of 10 values..... 137

Figure 5.11: a) Above Deionized water force vs displacement chart (0 concentration). The largest slope was 0.9. b) Below, 10 % concentration chart. The largest slope was 0.3..... 138

Figure 5.12: a) Above 20 % water force vs displacement chart. The largest slope was 0.89. b) Below, 30 % concentration chart. The largest slope was 0.85..... 139

Figure 5.13: a) Above 40 % water force vs displacement chart. The largest slope was 0.6. b) Below, 50 % concentration chart. The largest slope was 1.0..... 140

Figure 5.14: a) Above 60 % water force vs displacement chart. The largest slope was 0.98. b) Below, a comparison of all concentrations and their slopes. The largest slope was at 50% concentration at 0.5872..... 141

Figure 5.15: a) The slope showed an upward trend with increasing concentration, indicating consistency in the predicted surface tension. b) There was a correlation shown in the measured force with respect to the surface tension..... 142

Figure 5.16: Here, the average edge-shadow width is 47.2 microns. The pale gray line is the 150.3 micron measuring guide..... 144

Figure 5.16.a: The glass wafers are displaced by about 77.6 microns. Light area indicates space between the edges of the wafers..... 144

Figure 5.17: Guide marks were made, using Adobe Photoshop, on the image of the edge to aid in measurement of the edge shadow. For this initial alignment, the average width of the shadow was 50.51 microns. This image was made at 20x magnification..... 145

Figure 5.17.a: First realignment. The same guide marks were placed and measurements were taken in approximately the same places as the initial alignment image to get an idea of how well the pattern brings the wafers back to the original rest position. The placement of the guide marks is only approximate because the wafers shift during misalignment. The average shadow width is 59.14 microns..... 145

Figure 5.17.b: Second realignment. The average shadow width is 55.51 microns at relaxation..... 145

Figure 5.17.c: Third realignment. The average shadow width is 53.5 microns at relaxation..... 146

Figure 5.17.d: Fourth realignment. The average shadow width is 55.8 microns at relaxation..... 146

Figure 5.18: The spread of the difference in shadow widths was within the tolerance specified by the RF package design..... 147

Figure 5.19: The integrated package using the alignment pattern and the nylon bonding Two wafers with alignment patterns that have been successfully aligned and bonded..... 148

# CHAPTER 1: INTRODUCTION

## 1.1: Introduction

Radio frequency (RF) array manufacturing processes have been making great improvements in simplification, consolidation and miniaturization. Advancement toward these goals can be achieved by an RF 3-D package that overcomes the limitations of conventional RF array manufacture. Currently, land-based arrays are massive devices that combine batteries of antenna elements, transmit/receive (T/R) modules, beam-formers and signal processing modules into a large planar array. These devices are constructed upon many platforms including MEMS structures for the antenna elements and stripline tuners, optical elements for the beam formers, III-IV monolithic microwave integrated circuits (MMIC) for the transmit/receive modules, and amplifier modules, and Si devices for signal processing and lower tasks [Fourikis, 1997; Fourikis, 2000].

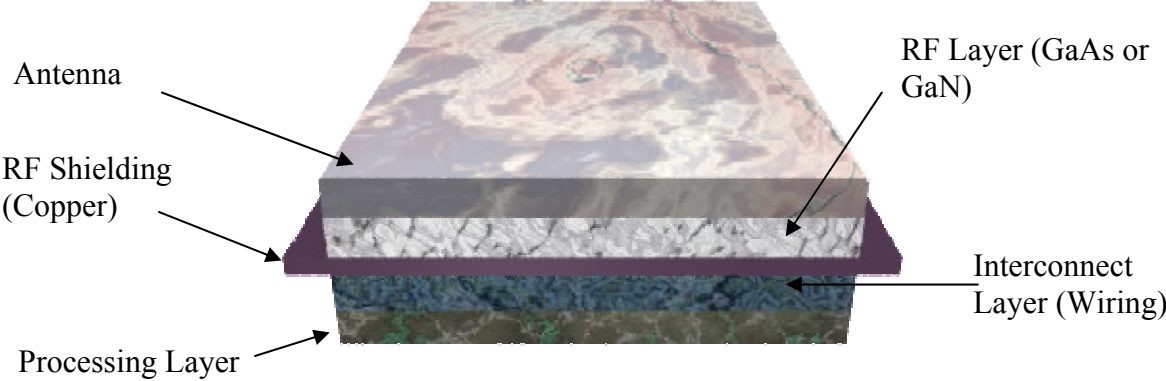


Figure.1.1: The wafer layers shown are the minimum needed for a functional RF array element. This compact device is the end goal of our study.

## 1.2: Goals

The science behind the technology of an integrated self-alignment and bonding mechanism, capable of accurately aligning through-wafer vias and preserving this alignment permanently, and utilizing the intrinsic properties of the SAMs deposited on the wafer surfaces, is the ultimate result of the enquiries posed by this study. With these requirements in mind, the goal of our studies is to understand and develop the following innovations:

- 1) A self-alignment mechanism for wafers in an RF package that is capable of aligning pairs of wafers as they are added in a stack of arbitrary height. It utilizes SAM functional group properties to control capillary forces.
  
- 2) A bonding process that can be integrated with the self-alignment mechanism, and that also makes use of the functional groups of self-assembled monolayers that are covalently bonded to the wafer surfaces. In particular, a line of covalent bonds could link wafers in a permanent bond.

### 1.2.1: Self-Alignment

One critical aspect of the development of this package is wafer self-alignment. One part of the 3-D stack concept that helps differentiate it from conventional RF modules is the miniaturization of the RF package components, which requires circuitry fabrication on the top and bottom of each wafer comprising the stack. Another aspect of this unique package that sets it apart is the communication between the wafers. This includes not only communication from one wafer to another, but from one side of an individual wafer to the

other. This is done through copper-coated vias, passage ways that allow this intra- and inter-communication between substrate layers. Previous to the development of these communication pathways, the movement of data between multi-wafer stacks was handled primarily through wires that were connected to the edges of the wafers.

“Until recently, practical interconnections of chip stacks were achievable only through wire bonding at the periphery, offering little or no benefits in the way of interconnect density or reduction of parasitics. But several new technologies offer the means to cost-effectively achieve very high densities of interconnection between chips in a stack, making true 3D ICs a reality.... An overview of these technologies includes wire bonding, microbumps, through vias and contactless interconnection.” [Davis, 2005]

Through-wafer vias offer shorter and more reliable communication and heat conduction pathways that enable more efficient operation of a wafer stack package. For vias to be a viable option in inter-wafer communication, the pattern of vias must match from one wafer in the stack to the next, and the wafers must be bonded to preserve the pathways made by these matching patterns. The size of these vias, and their alignment tolerance are two of the driving motivations for wafer alignment. However, the complex electronics in the component layers and the RF shielding conducting layer between the antenna layer and the electronics, acting as an antenna ground plane and shielding the electronics from the RF power, make alignment with IR optical “through viewing” difficult or impossible. Reliably stacking many complex layers or stacks with a metal RF shielding layer proved to be problematic [Walker, 2006].

“The wafers can be aligned manually for a two-layer stack. Add more layers, however, and they will all tend to move when trying to move one wafer, and the alignment assessment becomes more complex.” [Walker, 2006]

The alignment of the wafer components of the RF package requires a precision of 20 microns or less between the patterns of vias on each wafer. Manual manipulation on this scale can be attained with the precision needed to complete the functionality of the package, however, the difficulty arises with seeing if the alignment is correct. A mechanism that does not interfere with inter-chip positioning, and that can be relied upon to align the wafers with the requisite precision without needing to be verified, is required to do the work of alignment.

There are many parameters that influence the mechanism necessary for alignment, including via size, via alignment tolerance (how close the patterns of vias have to be to function), the size of the wafers, the types of functional groups needed for alignment SAMs and size of flow channels in the alignment pattern. The alignment process is required to move a 1” wafer, with an average thickness between 450 and 550 microns, without disturbing previously aligned wafers. The mechanism of alignment for the wafers must also incorporate the constituents used in bonding, and must release excess alignment fluid once alignment has been attained. The alignment process should lead directly into the bonding process, wherein the alignment fluid carries the bonding medium, and the surface functional groups used in alignment must also be compatible with bonding. We believe that all these requirements can be met with a self-alignment process.

Self-alignment has been achieved on the micron scale with the use of surface energy minimization [Srinivasan, 2001], as can be seen in figure 1.6. This natural phenomenon will also be used to drive our alignment process. However, until our group became involved, the

aligned surfaces were only millimeter-sized, not wafer-sized, and the scale-ups were not trivial.

“Capillary forces have been shown to be extremely powerful at the sub-millimeter scale... Whiteside and coworkers have made extensive use of the “capillary bond” in their discussion of self-assembly of millimeter scale objects. In a series of their experiments, polydimethylsiloxane objects were made to assemble into predetermined patterns at a liquid-liquid interface by modifying their wall chemistries to generate attractive or repulsive menisci. This application of surface free energy showed that the minimization of the curvature of the menisci formed at the interface was responsible for the assembly of the objects.” [Martin, 2001]

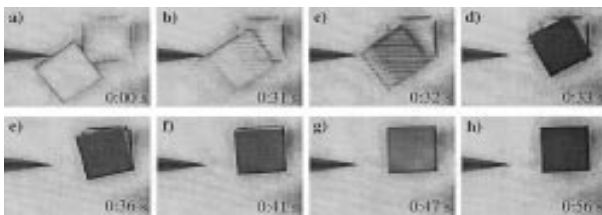


Figure 1.2: Frames of a self-assembly event. Part dimensions are 400X400X15  $\mu\text{m}$ . *U. Srinivasan, D. Liepmann, and R.T. Howe, J. Microelectromech. Sys* **10** (1) 17-24(2001)

Our goal is to achieve self-alignment on a larger scale, utilizing a similar type of energy minimization of the alignment fluid surface. We aim to produce an effective alignment pattern, record an alignment event, build a theoretical model of the energy minimization process, and measure the alignment force. The types of functional groups (hydrophilic and hydrophobic) available on the terminating ends of the SAMs will determine whether wafer self-alignment is possible. The development and implementation of this innovation was conducted within the group by previous M.S. student [Walker, 2006]. The continuation of the development of the alignment method of the wafer stack is furthered in this study. In addition to technical changes to the process, the underlying science has been modeled and the process

has been quantified. Also, methods of measuring alignment and measuring the forces required for alignment are of interest.

### 1.2.2: Bonding

Finally, the preparation of a bonding method between the wafers of the 3-D package is necessary, so that once the vias in the stack are properly aligned, the wafers could be permanently held into this configuration. In the model presented here, two different SAMs, 10-UTS and PEDDA, with an intermediary layer of nylon, are used to promote this bond.

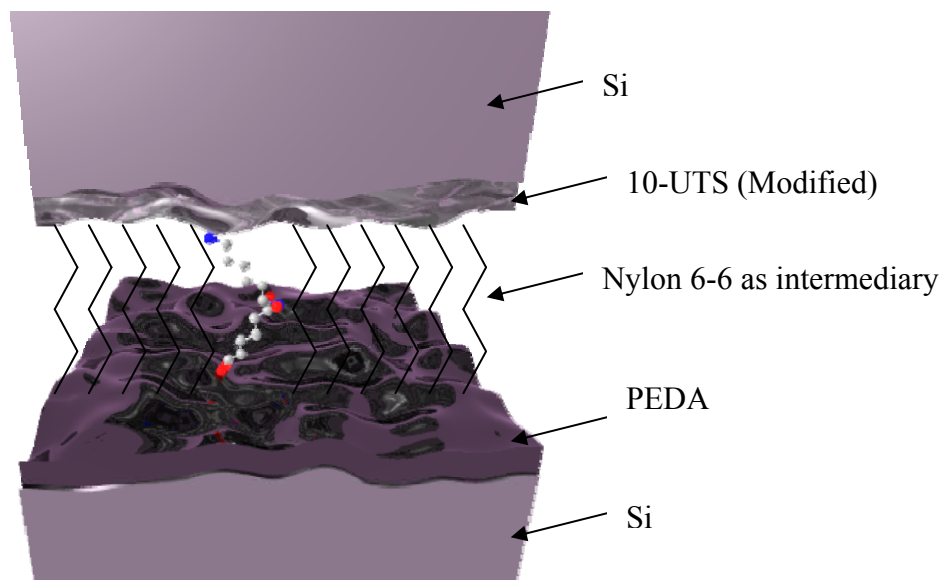


Figure 1.3: With SAMs coating the wafers, the surfaces of these wafers have the proper termination to allow an intermediary to perform the task of bonding.

The bond required cannot be accomplished by thick bonding agents, such as conventional epoxies, that release vapor upon curing, since bubbles will form and will lead to device failure after repeated temperature cycling during use. The mechanism is cyclic stress

fatigue from increased pressure due to repeated heating. [Neiman, 1962; Macan, 2005]. Our bonding instead uses a thin layer and covalent bonds from one wafer to the other, ideally. This provides a bond strength comparable to the strength of the wafers themselves. In order to bond wafers, SAMs with certain functional groups are deposited on cleaned silicon oxide. One of these SAMs must have the functional group modified by oxidation from vinyl to carboxyl acid. Ozone (produced by ultraviolet light), used to make this modification, is an innovation we use in this process. The bonding is characterized by measuring the bond strength and the bonded area, using a mechanical pulling apparatus and of IR-imaging, respectively. Conditions for reliable bonding are documented.

Also, bonding should be as solid as possible, to ensure that the wafers never move out of alignment. A permanent covalent bond between SAMs molecules deposited on the wafers solves this challenge.

### 1.2.3: Integration

It has been hypothesized that for the alignment and bonding to be successful, these two processes must be integrated. This is crucial because once alignment is achieved, no other manipulation of the package should be necessary to bond the wafers together. If these processes are not integrated, there is a risk of misalignment when the bonding process takes place.

Both of these processes utilize energy minimization as their physical basis. For the alignment, the minimization takes the form of the minimum surface energy of a fluid. The bonding uses energy minimization in the form of nylon salt formation. This is the most

important condition that must be met for these processes to achieve the goals of this study. The self-alignment pattern takes full advantage of the fluid's minimum surface energy, the force of cohesion between the molecules of the fluid, and the tendency for the fluid surface to come to a minimum being the driving mechanism behind alignment. For this condition, because of the flow channels built into the design, full alignment can only be achieved at the system's minimum energy. The bonding uses the minimization of the nylon structure between the surfaces, with the crystallization of the nylon solute into a salt.

There are several other conditions that must be met by both processes for successful integration that would make this goal possible. One of these conditions is a dual-purpose fluid. This process requires that the fluid used for alignment also enables bonding once full alignment has been achieved. This fluid must therefore contain the constituents that allow bonding to occur, namely the monomers of nylon 6,6.

Another requirement that must be met is congruent conditions for both processes. The conditions of alignment must also be favorable to the conditions required for bonding. The alignment and bonding both involve hydrophilic surfaces, so the self-assembled monolayers that enable bonding must allow alignment to also occur.

The last condition that both processes share is reliable carboxylic acid generation. Since both processes need a hydrophilic surface, and bonding has successfully been achieved using a carboxylic acid terminated SAM, it is believed that alignment can also be achieved with this SAM. The SAM, however, starts out with a vinyl terminal functional group. Oxidation of vinyl can be achieved by oxidation solution (potassium permanganate, sodium periodate, and potassium carbonate) or ozone produced by corona discharge.

### 1.3: RF Antenna Array Background

Arrays have already evolved from mechanical to electronic steering, accomplished by adjusting the phase within each T/R module to focus the wave front in the desired direction [Fourikis, 1997]. Also, the switch from brick elements to monolithic microwave integrated circuits (MMIC) improves efficiency and makes the array fail-soft, in that the large number of parallel devices allows for compensation for failed modules [Fourikis, 1997]. The MMIC technology also extends the lifetime of the array from hours to years. The next step in evolution is to make the array moldable, so that a smart “skin” of active array elements can be spread onto a curved surface, such as an aircraft wing.

The conventional architectures used today utilize mainly ‘brick’ and ‘tile’ type elements. These systems are designed using modular architectures where the electronic components are individually packaged and integrated onto rigid manifolds or panel [Lu, 2004].

The brick architecture (LITA) has the antenna elements and other subsystems in an orientation that is parallel to the longitudinal direction of the array aperture and that is stacked along a transverse direction [Fourikis, 1997].

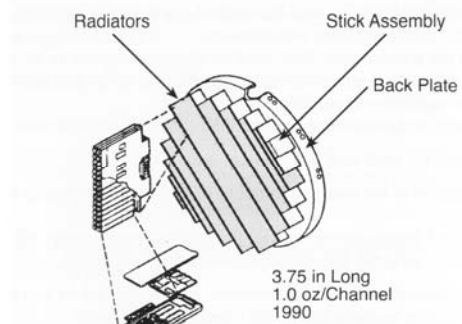


Figure 1.4: The brick architecture consists of several “sticks” connected to a back-plate and electrically connected to the RF, logic, and DC manifold. Fourikis, Nicholas. (1997). *Phased Array-Based Systems and Applications*.

The brick type architecture uses modules for the antenna and RF functions, and is the most space-expensive type of array. It has the most information bottlenecks because the modules must be connected by external, inefficient wires. Integration of this technology into practical military ventures, such as conformation to the skin of an aircraft or to the weight and space sensitivity design of spacecraft, or placement on the mast of a ship, in ground-based systems or the limited space of a missile, presents a significant obstacle to the advancement of passive or active detection capabilities in these ventures [Fourikis, 1997]. According to Fourikis, the cost of interconnecting the assembly of 2000 T/R modules is high, the array weighs several hundred pounds, and is approximately 12 inches long. This assembly is not low profile [Fourikis, 1997].

The tile architecture (TILA) has elements and other subsystems in an orientation that is parallel to the transverse array aperture and that is stacked in a longitudinal direction. The tile type is more compact, using multichip module packaging that puts the antenna, RF

functions and other subsystems on parallel wafers. This architecture is more compact, lightweight and affordable. The weight of a 2000-element array using this technology is less than 75 pounds and has a depth of less than 2 inches [Fourikis, 1997].

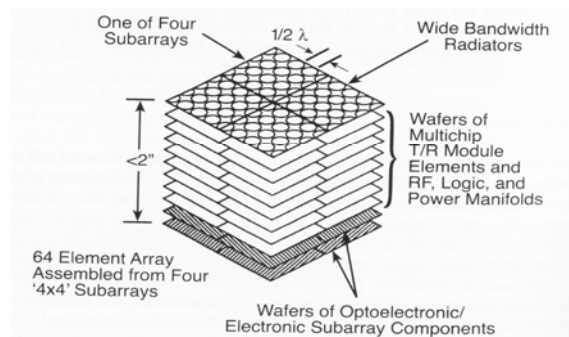


Figure1.5: Tile architecture. Fourikis, Nicholas. (1997). *Phased Array-Based Systems and Applications*.

There are currently passive and active large aperture membrane arrays, produced by the California Institute of Technology Jet Propulsion Laboratory. These membrane arrays consist two Kapton sheets. The outer sheet has a radiating patch of 12 m copper on the 2-mil thick Kapton, while the second sheet has the ground plate and T/R module [Moussessian, 2005]. JPL originally created this array with passive elements. The challenges involved in creating active elements included RF digital and power distribution demands due to the large number of active elements needed, and the high rates of data generation. Heat dissipation was also an issue [Moussessian, 2005]. This large aperture array, however, has applications in space-based Synthetic Aperture Radar (SAR) missions. The study at JPL asserts that with membrane antenna technology, an order-of-magnitude reduction in antenna aerial density can be achieved [Moussessian, 2005].

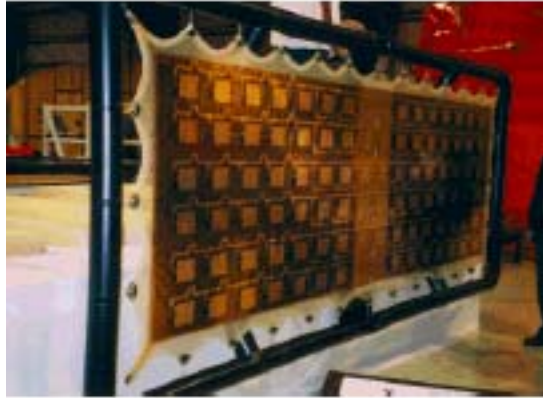


Figure 1.6: JPL's membrane antenna has demonstrated aerial densities of less than  $2 \text{ kg/m}^3$  which include structure and aperture. This is in comparison to  $20 \text{ kg/m}^3$  for the phased array used in the Shuttle Radar Topography Mission (SRTM). *Antennas and Propagation Society International Symposium, 2005 IEEE.*

The integration of a microstrip antenna and other active components is the distinguishing factor between the active array and the passive array.

An even more efficient and compact package would incorporate the high frequency devices and support electronics into a 3-D, wafer-on-contact-with-wafer package. Ultimately, the science and technology developed here would enable construction of a transmit/receive module, a signal processor, and an antenna together in a single package.

A typical front-end architecture for wireless applications contains an RF transceiver subsystem, which is comprised of a radio frequency integrated circuit (RFIC), a low noise amplifier (LNA) which is the receiver, a power amplifier (PA) which is the transmitter, and filters for both. This is generally interconnected to the antenna through a matching network and antenna switch which switches the circuit from the transmit mode to the receive mode

and back [Lu, 2004]. The matching network can be formed on the surface of the PA chip from planar IC elements, if sufficient space is available.

These subsystems, networked together make an element of the antenna array. The differing technologies work well together, but there is considerable delay, manual fabrication effort, and loss of long-term reliability through the wire-bonding and physical links that allow these subsystems to communicate. Although breakthroughs in CMOS and SiGe technologies have resulted in single chip transceivers, wherein the RFIC, LNA, PA and filters have all been printed on the same die, there are still bottlenecks of data transfer that slow the response time of the array, and architectural limitations that stymie the growing demand for even more portable, less expensive, and flexible sensory apparatuses.

System design incompatibilities must also be considered. RF circuits are designed to achieve tight coupling, thereby preventing unwanted field emissions or radiation. The low noise amplifier cannot tolerate noise coupled from the digital signal. Nor can the input of the power amplifier operate with signal noise. Antennae, on the other hand, must be designed to radiate energy efficiently [Lu, 2005]. The digital signal cannot survive the radio frequency from the antenna. This necessitates the use of RF shielding in the design to protect the RF circuitry from the emissions of the antenna.

Because the different subsystems of an individual array element use different semiconductor technologies, it is not at present possible to integrate them all onto a single die. According to Benkart, et al., one solution to the problem of integrating mixed technologies is the concept of 3D stacking. The study by Benkart et. al says further:

“...The designer builds a system by stacking several dies. Using an optimized standard technology, (CMOS or sensor, for example) a manufacturer fabricates each layer of this chip stack, implementing additional processing steps to prepare the individual dies for the stacking process. Interchip connections, which compose a 2D arrangement on both the front and the back-sides of the stacked dies, create electrical connections. Interchip vias provide connectivity between arbitrary layers of the physical architecture, resulting in short communication lengths, which enhance performance and decrease power consumption significantly.” [Benkart, 2005]

In our framework, three different types of wafers, at minimum, will be required to encompass all the different components to make up a single element. With the ability to produce thin wafers, however, stack height is not so much the issue as communication between the wafers in this stack.

The use of chip-stacking would provide more powerful and more efficient array elements. There are inherent difficulties to this method of fabrication, however. Alignment of the different chips so that vias and circuitry line up between the chips is critical. Reliable bonding between the chips that will not fail under normal or extraordinary RF array operating conditions is another significant hurdle. The work presented here describes potential solutions to these particular obstacles.

The enabling technologies for 3D wafer stacking packaging proposed by this study should aid in the construction of active membrane arrays, completely replacing rigid arrays. This may be done by creating a module that incorporates the antenna element, the RF components and supporting signal processing subsystems into a package that is three or more wafers thick and up to full wafer size in lateral extent. Integrated into a membrane, a phased array can be created that are less than 10 pounds, hundreds of microns thick and easily moldable to curved surfaces.

#### 1.4: Conclusion

Radio frequency (RF) array manufacturing processes have been making great improvements in simplification, consolidation and miniaturization. These devices are constructed upon many platforms including MEMS structures for the antenna elements and stripline tuners, optical elements for the beam formers, III-IV monolithic microwave integrated circuits (MMIC) for the transmit/receive modules, and amplifier modules, and Si devices for signal processing and lower tasks. The switch from brick elements to monolithic microwave integrated circuits (MMIC) improves efficiency and makes the array fail soft, in that the large number of parallel devices allows for compensation for failed modules.

Different subsystems, networked together, make an element of an antenna array. The differing technologies work well together, but there is considerable delay, manual fabrication effort, and loss of long-term reliability through the wire-bonding and physical links that allow these subsystems to communicate. A more efficient and compact package would incorporate the high frequency devices and support electronics into a 3-D, wafer-on-contact-with-wafer package. Ultimately, the science and technology developed here would enable construction of a transmit/receive module, a signal processor, and an antenna together in a single package. Three different types of wafers, at minimum, will be required to encompass all the different components to make up a single element. With the ability to produce thin wafers, however, stack height is not so much the issue as communication between the wafers in this stack. The enabling technologies for 3D wafer stacking packaging proposed by this study may be done by creating a module that incorporates the antenna element, the RF

components and supporting signal processing subsystems into a package that is full wafer size in lateral extent.

Through-wafer vias offer shorter and more reliable communication and heat conduction pathways that enable more efficient operation of a wafer stack package. For vias to be a viable option in inter-wafer communication, the pattern of vias must match from one wafer in the stack to the next, and the wafers must be bonded to preserve the pathways made by these matching patterns. The complex electronics in the component layers and the RF shielding make alignment with IR optical “through viewing” difficult or impossible.

The goal of our studies is to understand and develop the following innovations:

- 1) A self-alignment mechanism for wafers in an RF package that is capable of aligning pairs of wafers as they are added in a stack of arbitrary height. It utilizes SAM functional group properties to control capillary forces.
- 2) A bonding process that can be integrated with the self-alignment mechanism, and that also makes use of the functional groups of self-assembled monolayers that are covalently bonded to the wafer surfaces. In particular, a line of covalent bonds could link wafers in a permanent bond.

## CHAPTER 2: MATERIALS AND OXIDATION

### 2.1: Introduction

The RF array 3-D package described here makes novel use of existing, well-developed technologies based upon industrially viable materials. The materials used are shown to be compatible with processing of the finished package. The wafers used do not contain devices, but present similar surfaces to a planarized wafer. These materials include self-assembled monolayers, silicon wafers, nylon 6-6 and ozone. A comprehensive list of materials follows. The chemical hazards are given by the NFPA 704 ratings (H – health, F – flammability, R – reactivity) in the list below.

#### Materials List by Process

##### Process:

##### Cleaning

Sulfuric Acid from Fisher Scientific H:3 , F:0 , R:2

Hydrogen Peroxide from Fisher Scientific H:2 , F:0 , R:1

##### 10-UTS Deposition

10-Undecenyltrichlorosilane from Gelest (vinyl-terminated SAMs) H:3, F:1, R:1

Anhydrous Hexadecane +99% from Fisher Scientific H:2, F:1, R:0, C:3

Isopropanol HPLC grade from Fisher Scientific H:1, F:3, R:0

Dichloromethane ACS grade from Fisher Scientific H:3, F:0, R:2, C:4

Chloroform ACS Grade from Fisher Scientific H:3, F:1, R:1, C:3

#### PEDA Deposition

(Aminoethylaminomethyl)Phenethyltrimethoxysilane from Gelest H:3 , F:1 , R:1

Glacial Acid from Fisher Scientific H:2 , F:2 , R:2

Methanol from Fisher Scientific H:1 , F:3 , R:0

#### Alignment Pattern Fabrication

Microposit S1818 Positive Photoresist from Rohm &Haas H:2, F:2, R:0

Microposit MF319 developer from Rohm & Haas H:3, F:0, R:0

Acetone from Fisher Scientific H:1 , F:3 , R:0

#### Bonding

Adipic Acid from Spectrum H:1 , F:1 , R:0

Hexamethylene Diamine from Spectrum H:3 , F:2 , R:0

Terephthalic Acid from Spectrum H:1 , F:1 , R:0

Para-Phenylene Diamine from Spectrum H:3 , F:1 , R:0

Ethanol from Fisher Scientific H:1 , F:3 , R:0

### 2.2: Self-Assembled Monolayer Deposition

Self-assembled monolayer (SAM) formation on the silicon oxide surface of thin wafers is one of the integral processes used in these experiments. SAMs are long-chain molecules that create a single layer on a surface, formed by liquid or vapor deposition. Though rigidly attached by covalent bonds, the long molecules deform when put under

pressure. SAMs are a unique from ordinary surfactant monolayers by the fact that one end of the molecule is designed to favorably react with the substrate, usually the hydrophilic end, and the other end contains a functional group with specific properties necessary for substrate experimentation [Schwartz, 2001]. Complete coverage of the substrate in effect creates a new surface, composed of the functional groups at the exposed end of the molecules, which is reactive to a wider variety of chemicals than the original wafer. The new overall surface formed by the amalgamation serves to alter the interactive surface energy and properties. Thus, using SAMs, the surface characteristics of the wafer can be changed to field many types of reactions [Wasserman, 1989]. These functional groups are ideal for our study and can be modified according to the demands of the experiments. With these functional groups, an even layer with the correct chemical composition is guaranteed. The two SAMs layers that are used in this study have an amine and a carboxylic acid as the reactive functional groups, respectively. To fabricate our nylon nanoglue, we require a covalent bond between the functional groups of these two self-assembled monolayers. If the functional group needed is hydrophilic, as carboxylic acid is, it must be derived from a nonpolar functional group, because the end reactive with the substrate must also be hydrophilic [Wasserman, 1989], in which case the end that must be manipulated later needs to be hydrophobic. Otherwise, there is no guarantee of creating a uniform monolayer with the correct functional group oriented outward to form the reactive surface. One of the functional groups used in this study, carboxylic acid, is hydrophilic, and while alkyltrichlorosilane monolayers with carboxylic acid functional groups can be synthesized, they cannot be used on silicon oxide because the  $\text{RSiCl}_3$  on one end of the molecule reacts with the  $\text{RCO}_2\text{H}$  on the other end [Schwartz, 2001].

Attempts to use such reacting monomers would result in long-chain molecular structures in the place of uniform monolayers.

SAMs are molecules that create a single, even, reliable layer on a surface. Under the correct conditions, SAMs always produce the same layer coverage in relatively simple, repeatable steps, as opposed to other surface adsorbants that cannot guarantee this level of evenness [Schwartz, 2001].

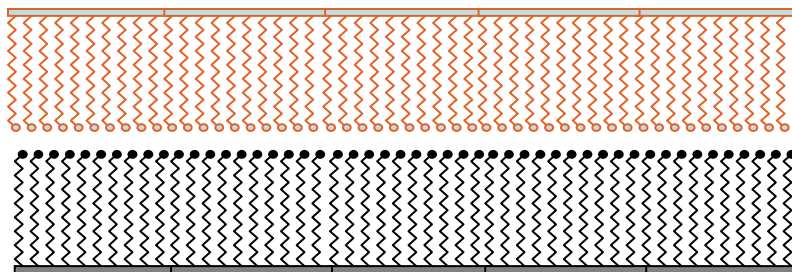


Figure 2.1: SAMs form even, predictable layers on silicon and other substrates.

SAMs molecules are impervious to strong acids and many solvents, and they form a very strong, covalent bond to the substrates. These monolayers, covalently bonded, are very stable. Thus, difficult chemical restructuring can be performed on the surface terminal groups without fear of destruction of the surface. According to Wasserman et al.

“...The formation of these monolayers is driven by the formation of the covalent silicon-oxygen bond rather than by the maximization of van der Waals interactions between adjacent alkyl groups.” [Rubin, 2001]

SAMs formation is sensitive to moisture, thus, they must be grown in a nitrogen environment [Schwartz, 2001]. Not only is the layer formation affected, but also the solutions for the formation of the monolayers. Prepared and stored under nitrogen, these solutions can be used for several weeks, whereas preparation and storage under ambient laboratory

atmosphere, the solutions must be used within 12 hours; after 24 hours a visible precipitate forms [Wasserman, 1989].

Although SAMs stand up to strong acids, they are destroyed by strong basic solutions. Wasserman found that monolayers prepared from  $\text{CH}_3(\text{CH}_2)_{13}\text{SiCl}_3$  were stable in contact with aqueous acid at room temperature and hexadecane at  $75^\circ\text{C}$ . But when these monolayers were exposed to aqueous base at room temperature, approximately 50% of the monolayer had been removed after 80 minutes [Wasserman, 1989].

### 2.2.1: General Theory of Deposition

According to Wasserman, et al., formation of monolayers from organosilicon on a glass or silicon oxide layer is one of several methods for forming organic monolayers.<sup>1</sup> Other methods include adsorption of alkanethiols, dialkyl disulfides and dialkyl sulfides on gold, adsorption of fatty acids on alumina, and adsorption of alcohols and amines on platinum [Wasserman, 2001].

The processes involved in SAMs growth include:

- 1) Preparation of the surface. Preparation of the surface includes the chemical cleaning and rinses. Cleaning and rinses in the case of silicon ensure a uniform oxide layer, or in some cases, change the surface to a uniform hydrogen-terminated layer. Preparation of the surface makes the substrate receptive to the adsorbate molecule by changing the surface energy.
- 2) Transport of the adsorbate molecules to the solid-liquid surface. This includes diffusion and convection within the fluid. The adsorbate molecule is prepared in

solution with a neutral solvent, at a specified concentration. The solvent aids in allowing the molecule three degrees of freedom so that when the substrate is immersed in the solution, the molecules may orient themselves correctly to the surface. The solvent also carries away any resultant by products of the absorption reaction.

- 3) Adsorption onto the surface. This process works to lower the surface energy through the adsorption of molecule onto the substrate. Adsorption is generally not uniform, but occurs by nucleation formation. There is an optimum adsorption time in which 90% of the molecules adsorb onto the surface. Additional time may be allowed for complete coverage, but can also result in multilayering.
- 4) 2-D molecular organization on the substrate surface. This process can include intermediate surface phases [Schwartz, 2001]. The adsorbate molecules might not be oriented at the proper angle with initial adsorption. A relaxation time might be necessary to allow the molecules to shift into the proper orientation [Schwartz, 2001; Wasserman, 1989].

### 2.2.2: Wafer Cleaning

Reactive cleaning of the substrate is the initial step necessary in the preparation of the wafer for deposition. This type of cleaning uses an exothermic reaction of a strong acid and a strong base to remove organic residues and other contaminants from the substrate surface. One reactive cleaner is piranha solution, which consists of hydrogen peroxide and sulfuric acid. The piranha solution is three parts hydrogen peroxide to two parts sulfuric acid. The

peroxide must be placed in the beaker first, and then the sulfuric acid must be added to the peroxide slowly. This reaction produces heat, which aids in the removal of impurities.

The wafers, once cleaved into the requisite shape and size, are placed in a Pyrex beaker and cleaned. The sample wafers must be placed with the polished side facing up, since the polished surface will be used in further procedures. The samples stay in the cleaning solution for an hour. It is important that none of the samples overlap in the cleaning solution. This is because if there is any overlap, the part of the sample that is covered will not be cleaned evenly with the rest of the wafer. The samples must also be completely covered by the solution, or impurities will remain on the uncovered part of the surface. After cleaning, the samples are rinsed twice in deionized water. The second rinsing is done in air using a squirt bottle of deionized water. The back and front of each wafer is rinsed to insure that all traces of the piranha solution are gone. Waste piranha solution must be kept in a container with a vented cap, or pressure from the  $H_2O_2$  generation can dangerously pressurize the container. This also allows water to evaporate, so the sulfuric acid can become highly concentrated and weep from the container under humid conditions.

### 2.2.3: 10-Undecenyltrichloroxysilane Deposition

Once cleaned, the wafers are ready for the deposition procedure. Each wafer must be dried with nitrogen (dry air). Then, for the 10-UTS deposition, the samples are immersed in 99% HPLC isopropanol in a Pyrex beaker. Depending on the size and number of samples, the beakers used ranged in size from 40 mL to 600 mL. Generally, the 40 mL beaker held a single one-inch square sample on the bottom, while the 600 mL beaker held four samples of

this size. No sample holders were used. The beaker is placed in the airlock of the drybox and nitrogen is cycled through for four minutes. This is to bring the airlock under full nitrogen atmosphere. After four minutes, the beaker can be moved from the airlock to the main drybox chamber.

Once the samples are in the main drybox, they must be rinsed in dichloromethane, chloroform and anhydrous hexadecane before being immersed in the 10-UTS solution. Each rinse is five minutes, and these rinses are missible in each other. The samples stay in deposition for a period of 1 to 24 hours.

The 10-UTS solution is a 2% solution composed of hexadecane and the 10-UTS precursor. For every 100 mL of solution, 98 mL of hexadecane for every 2 mL of precursor is used.

After deposition, the samples are rinsed in dichloromethane and chloroform for 5 minutes, and then placed and stored in isopropanol. These samples are now ready for ozonation, described in ‘SAMs modifications’.

#### 2.2.4: PEDAs Deposition

The preparation of wafers for amine-terminated SAMs deposition begins with the same procedure for chemical cleaning, in which either piranha or RCA cleaning solutions are used to remove surface contaminants. Once cleaned and rinsed in 18 ohm deionized water, the samples are immersed in methanol for transfer into the dry environment. Under the nitrogen solution, the wafers can be put directly into the PEDAs solution.

For a 1% PEDA solution, an acidic methanol solution around 1mM of acidic acid is required. This solution is mixed under a nitrogen atmosphere. This requires 406 mL of methanol, 25 mL of deionized water, 5 mL of PEDA, and 1.52 mL of acidic acid (glacial acid).

The methanol and glacial acid should be mixed together first. Let this mixture sit for 30 seconds, then add the PEDA. Wait another 30 seconds, then add the DI water. Pour contents into an amber bottle. This solution should be stored under nitrogen [Hallen].

The PEDA contact angle is around  $30^\circ$  -  $40^\circ$  for PEDA grown on an oxide layer, and  $55^\circ$  -  $70^\circ$  on a hydrogen terminated surface.

For this experiment, the wafers were left in deposition (immersed in the PEDA solution) for 24 hours, using the oxide layer. Then the wafers were immersed in methanol until they were needed for bonding.

#### 2.2.5: SAMs Modification

Development of a reliable oxidation method is required for the modification of our SAMs functional group. Carboxylic acid-terminated SAMs do not bond correctly to  $\text{SiO}_2$  because SAMs with both a trioxysilane and a carboxyl at the ends would have the option of bonding with either functional group, because both are hydrophilic. The terminal end that bonds to the silicon is required to be hydrophilic, so the other end must be hydrophobic. Therefore, the SAM that we use is vinyl- (or methyl-) terminated, and once deposited on the surface, the vinyl-termination must be modified to the required carboxyl termination.

Functional group modification can be accomplished by several means. One method is oxidation by solution. The solution is composed of potassium permanganate, sodium

periodate, and potassium carbonate [Sagiv, 1983]. This method is slow, requiring at least 24 hours. This method is also messy and requires disposal of waste product and does not give 100% modification of the vinyl-termination. In fact, it only gives  $\sim 20\%$  based on contact angle, according to the Cassie equation:

$$\cos \theta_m = \beta \cos \theta_1 + (1 - \beta) \cos \theta_2 \quad (2.1)$$

Where  $\theta_m$  is the measured contact angle,  $\theta_1$  is the contact angle for layer one, and  $\theta_2$  is the contact angle for layer two [Tsukurk, 1999; Cassie, 1944].

Another method is the use of ozonolysis (exposing the surface to ozone) and hydrolyzation. Ozone is a faster, more complete method of oxidation. Ozone has several advantages over an oxidizing solution. First, ozone is a powerful oxidizer. The flow of the ozone can be controlled, so that overall coverage of the substrate surface is more likely. Ozone works faster than the solution, and produces less waste. Also, ozone does not need to be stored, but can be generated at anytime with pure  $O_2$  or dry air. Ozone preferentially attacks a carbon double-bond. The 10-UTS molecule contains one carbon double bond in the terminating vinyl group, so the carboxyl group forms near the terminal end [Hallen, 2008]. This process has a much higher yield (80% or more), but must be calibrated, as too much ozone will remove the layer.

The initial tests using ozone as primary oxidizing agent in our work was done with a UV-ozone cleaner, shown in figure 2.2. Sample wafers with a 10-UTS samples were placed in the UV-ozone cleaner for varying amounts of time, which increased in intervals of 50 seconds, to find the optimum oxidation time. At approximately 150 s the contact angle right after ozonation is high, indicating that the surface is still hydrophobic. The advancing and

receding contact angles are very close to the regular contact angle, about  $25^\circ$ , at 150s. Then after hydrolysis in water for 30 minutes, the receding contact angle for the 150 second mark drops to zero, showing that the surface has become hydrophilic. The ellipsometry graph shows a layer change of 2 angstroms, indicating that there is still some layer present, but some small part of the SAMs has been cleaned off. The carbon double bond is approximately 2 angstroms. However, at 200s, the layer is completely gone. The presence of the SAMs and the drop to zero receding contact angle are good signifiers that the UV-ozone cleaning process, followed by hydrolysis, has successfully changed the SAMs functional group from vinyl to carboxylic acid.

The purpose of a more efficient oxidation procedure is to create hydrophilic regions on the 10-UTS hydrophobic, vinyl-terminated surface. This alteration produces a change in the surface energy of our sample, allowing wetting, where wetting is the ability of a liquid to maintain contact with a solid surface resulting from intermolecular interactions. The degree of wetting is determined by the characteristics of the surface [Sharfrin, 1960].

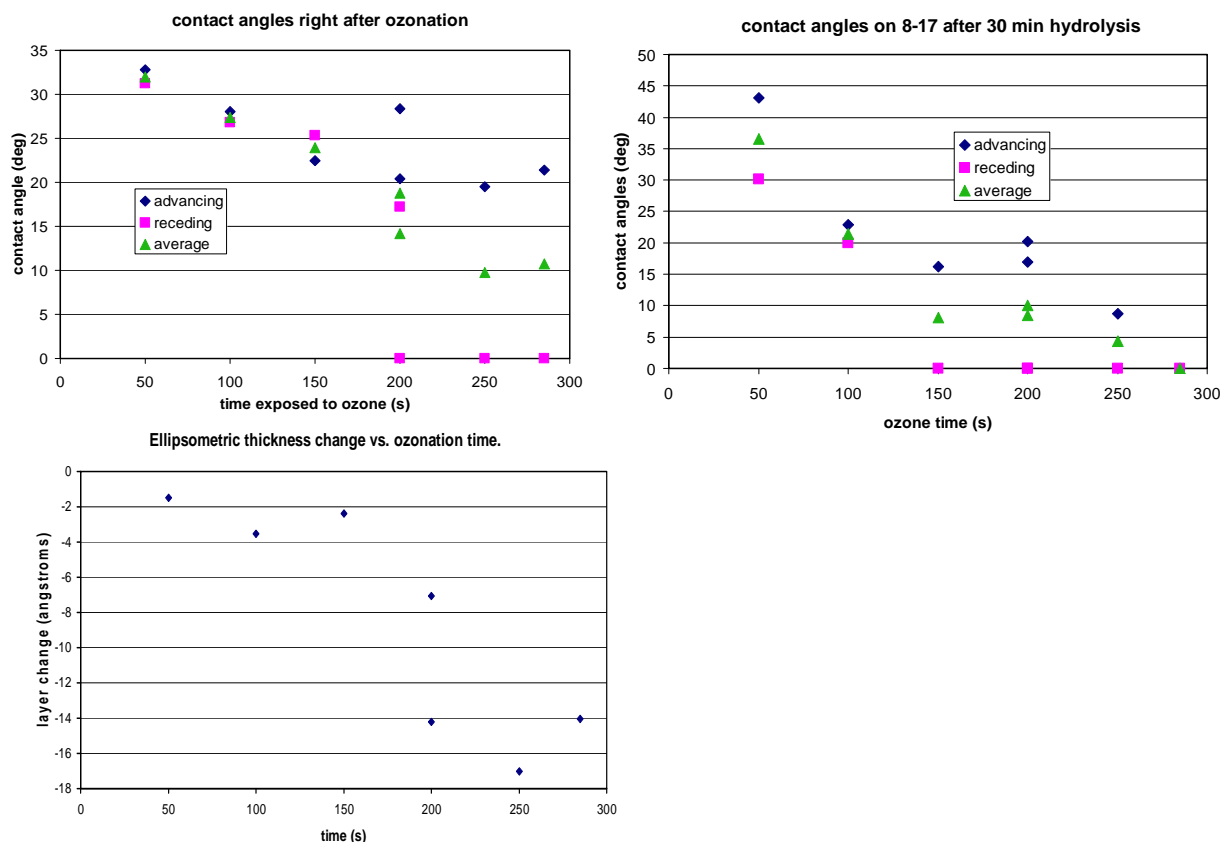


Figure 2.2: The oxidation by ozone of 10-UTS. There is an optimum time of exposure where the carbon double bond is broken, but the layer is not stripped away, at 150s. For this UV/ozone cleaner, the time was ~ 200 seconds. However, this leaves little room for error. *Synthesis of Carboxylic Acid Monolayers by Ozonolysis of 10-UTS SAMs*, Hallen, M., Hallen, H. (2008)

The surface energy of the SAMs must be raised within the prospective hydrophilic pattern, increasing the adhesion between the solution and the SAM functional group.

### 2.3: Ozonation

Ozone is a triatomic molecule that can be found in nature. It consists of three oxygen atoms. The molecule has a bend of  $116.8^\circ$ , and the distribution of electrons makes the molecule polar. One side has double bonds, while the other has a single bond. The bond

lengths are 1.278 Å. Ozone is an allotrope of oxygen, much less stable than diatomic oxygen [Rubin, 2001].

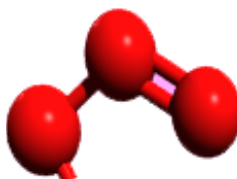


Figure 2.3: Ozone is a triatomic molecule of oxygen. This configuration is highly unstable and has a tendency to break down to diatomic oxygen and an oxygen atom.

Ozone oxidizes by attacking carbon double bonds. Ozone can behave as a 1,3 dipole. Because of its structure, an ozone molecule can undergo a 1-3 dipolar cyclo-addition reaction with saturated compounds. This reaction leads to the formation of an ozonide compound:

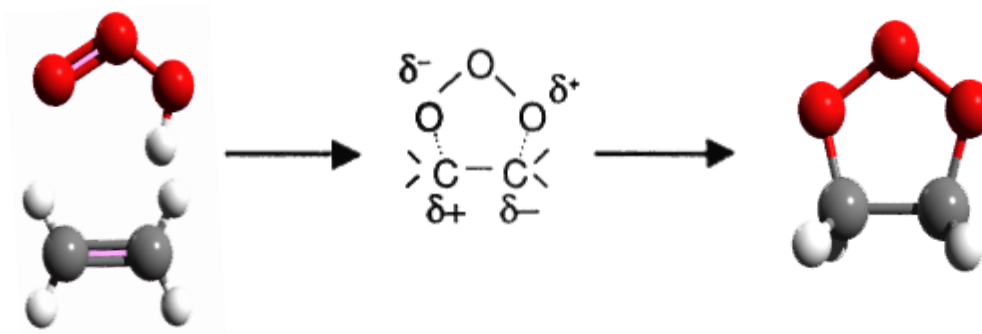


Figure 2.4: Ozone attacks the double bond of carbon.

When immersed in a protonic solution (like water), the primary ozonide disintegrates into an aldehyde, a ketone, or a zwitterion. If it disintegrates into a zwitterion ion, it will disintegrate further into hydrogen peroxide and carboxylic acid compounds [Von Gunten, 2003].

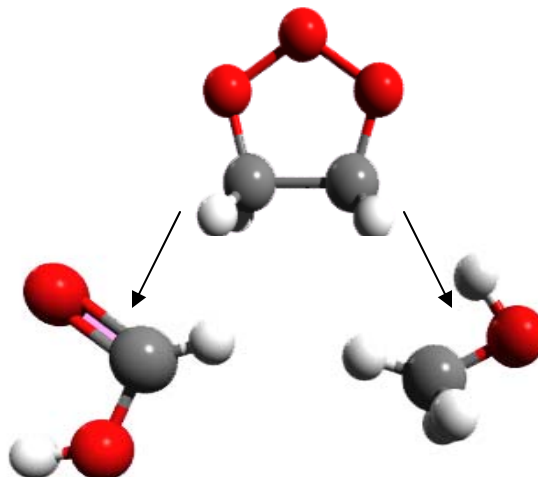


Figure 2.5: The ozonide disintegrates into other molecules, which, when exposed to water, can yield carboxylic acid.

The vinyl functional group has two carbons held by a double bond. Our functional group modification process necessitated the use of ozonolysis to destroy the carbon double-bond of vinyl using ozone and then hydrolysis to produce the carboxylic acid [Von Gunten, 2003].

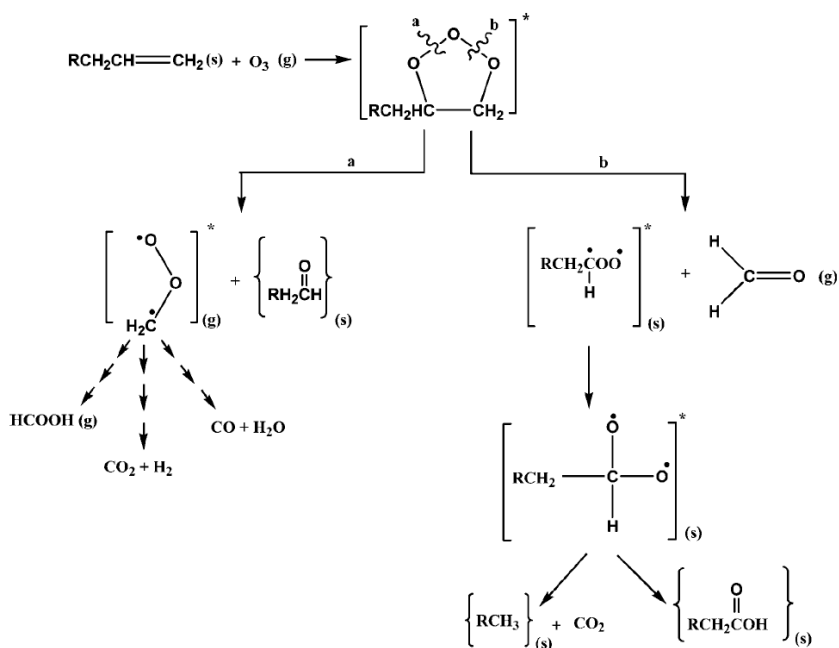


Figure 2.6: The oxidation of vinyl can take many paths to come to carboxylic acid.

### 2.3.1: Ozone Generation

Ozone, because of its instability, cannot be stored or transported like other industrial gases [Kittel, 2005]. Stored O<sub>3</sub> quickly decays into diatomic oxygen, and must therefore be generated on site. Ozone's high reactivity allows only a few materials, such as stainless steel (quality 316L), titanium, aluminum, glass, polytetrafluorethylene, or polyvinylidene fluoride, to be used in its generation or dissemination. Ozone can be produced by several means, the most popular ways being UV absorption and corona discharge.

The success of the modification of the vinyl functional group by ozone can be determined by contact angle. We explored options in making ozone and carefully chose the materials for our ozonation system because of its unstable and reactive nature.

### 2.3.2: Ultraviolet light Generation of Ozone

Ultraviolet light is electromagnetic radiation with a wavelength range of 10 nm to 350 nm, and energies from 3 eV to 124 eV. These light waves are very energetic; their energy is inversely proportional to the wavelength. UV is absorbed by ozone at certain wavelengths. In the atmosphere, this is beneficial, because UV-C, which is UV light of the wavelengths 100-280 nm, is inimical to living cells. By the same token, diatomic oxygen which has a bond length of 121 pm and a bond energy of 498 kJ/mol, when exposed to these same wavelengths, can split apart and reform into ozone. UV radiation excites electrons binding diatomic oxygen, splitting the molecule into oxygen ions. These ions are then capable of recombining into ozone. We created ozone by this method with UV LEDs, but the

intensity was too low, and with the Hg lamps, but the ozone concentration was difficult to regulate. Long term reproducibility was also a concern.

### 2.3.3: Corona Discharge Ozone Generation

This method of producing ozone is based on the principle of applying a strong electric field across two conductors, one of which comes to a sharp point and the other shaped as a large aperture, to generate a very large electric potential. When this potential is large enough, the air around the tip of the sharp conductor becomes ionized, and the ions will be accelerated by the electric field [Halliday, 1997]. These fast-moving ions can cause diatomic oxygen to split and recombine with other  $O_2$  molecules as  $O_3$ . We found that the corona discharge mechanism is stable and reproducible. An ozone meter showed that our initial attempts at using this method gave 7-8 ppm ozone using an OS-1X ozone detector, with a single tip in air over a wide range of tip-sample distances. The bright spot at the end of the tip (at -5kV) is the discharge, which drives air flow. The ozone concentrations should increase with the number of tips and moving to pure oxygen. The voltage can be varied to adjust the ozone concentration in the apparatus.

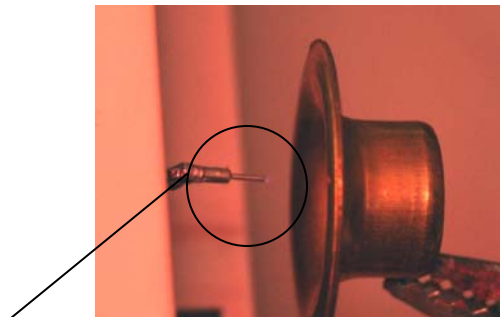


Figure 2.7: Corona discharge is a reliable method for producing ozone. The discharge is dimly seen in the center of the circle.

#### 2.3.4: Ozone Delivery Apparatus

The ozone delivery system consists of three major components: the delivery chamber, the ozone generator, and the dry air source.

The ozone delivery system was lab built. It consists of one quartz tube, one Pyrex glass funnel, two rubber pipe connectors, one PVC pipe connector, and an ozone sensor, Figure 2.9. The quartz tube main part of the ozonator was a fused quartz tube 30 cm in length, with an inner diameter of 10.16 cm and an outer diameter of 10.66 cm. The diameter and length were chosen to create an even ozone flow over the wafer below. The glass funnel was the top cap of the chamber, held in place by one of the rubber pipe connectors. Filter paper was spread across the top of the quartz cylinder at the funnel-tube junction and was used to create the even flow. The glass funnel was connected to the oxygen source by means of plastic tubing. The PVC cylinder was the base of the apparatus. The other rubber pipe connector supported the quartz tube on this base. Evenly spaced notches were cut into the base to allow ozone to flow out uniformly, and also to provide an access port to the ozone sensor. The delivery chamber was designed to allow an evenly distributed flow of ozone to be delivered onto a sample with the vinyl-terminated SAM deposited on its surface. The entire apparatus was located under a fume hood, because ozone is a biohazard. The base of the ozonator was surrounded by a shield to keep the airflow from the fume hood from disrupting the even flow of ozone out of the chamber.

Three modes of operation were used: flowing ozone/dry air into the chamber, generation of ozone by UV absorption in the chamber, and generation of ozone by corona

discharge into the chamber, to determine which method was more effective and reliable. Most of the work reported utilized an external ozone generator.

This apparatus is capable of using UV LEDs to generate ozone from pure oxygen. The quartz of the tube was chosen for its transparency to UV radiation, in addition to being impervious to ozone. It was ideal to transmit the light from the LEDs into the delivery chamber. With oxygen in the tube and the LEDs giving light at the proper wavelength, the UV coming into the quartz chamber acted upon the oxygen flowing into the chamber to produce ozone. The design had three wide emission angle UV (375 nm) LEDs as the UV sources, one UV LED with a narrower beam, combined with a photo-sensor at the other side of the tube, could be used to indicate ozone concentration. A pressure regulator and the operational circuitry to run the LEDs were also available.

The UV LEDs (ultraviolet light emitting diodes) produced light with a wavelength of 375 nm. This was one of the absorption wavelengths of ozone. The top three LEDs had a dispersal angle of 100 degrees. The bottom, test LED had a dispersal angle of 10 degrees. The LEDs are to be located outside the main quartz chamber, held in place by the rubber supports. The main chamber was wrapped in foil, to reflect the UV rays, and to give an even exposure throughout the cross-sectional area of the chamber. The lower LED, held in place by the second rubber support, is necessary to provide a reference for how much ozone is being produced. The oxygen was pressure regulated to control the flow into the chamber. The power output of each LED was at 2 mW at 20 mA supplied current, in a 100° cone angle. The ozone output in this mode was 0.19 ppm.

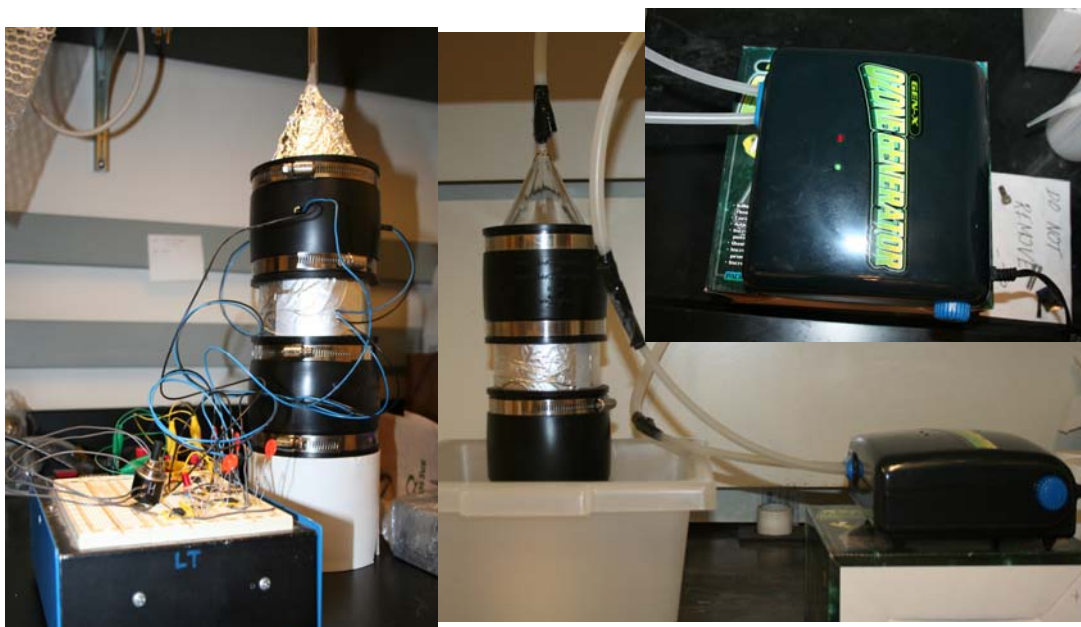


Figure 2.8: The old apparatus versus the new configuration for the oxidation of vinyl to form carboxylic acid. The UV LEDs were replaced by an ozone generator, which was safer and easier to use.

Our delivery apparatus for ozone produced by corona discharge differed from the UV set-up only in the method by which the ozone was produced and the gases used. The quartz tube, funnel and PVC base that served in the UV set-up were also well-suited for the CD set-up. Even though the transparency to UV was no longer required, the quartz tube was retained for its imperviousness to ozone. An arrangement of nickel needle tips were mounted by spot welding onto wires above counter-sunk holes in a brass plate.



Figure 2.9: Corona discharge apparatus. This design was not completed, because of a failure of the high voltage source.

A high voltage (15 kV) produced conditions for corona discharge. This apparatus experienced problems, and would have had to be re-machined to be put to practical use. Other issues included the breaking of the pins that were spot-welded to the discharge apparatus with spatial adjustments and a need to re-engineer the brass plate to fit properly into the PVC sleeve. Also, the voltage multiplier experienced problems with the soldered joints.

### 2.3.5: Ozone Generator

The final method used the same apparatus with an external ozone generator. The generator itself was a Gen X ozone generator, typically used to clean water in aquariums. The air source was dry air instead of pure oxygen, and the ozone output was a uniform 8.25 ppm. This configuration worked very well, and was used for the last 50% of wafers produced for both bonding and alignment.

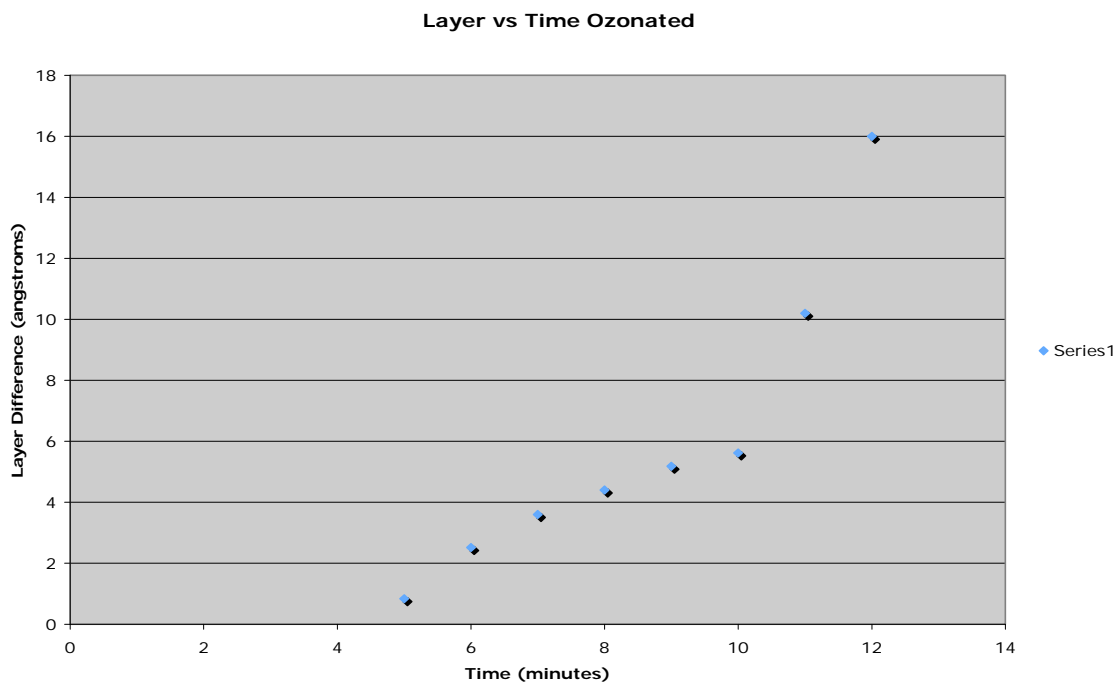


Figure 2.10: The layer stripped away versus the time of exposure to ozone. The optimal time fell at ~ 11.5 minutes.

Unlike the UV/ozone cleaner, which produced ozone at a single rate, the rate of generation with the external source could be regulated and measured with an ozone sensor. The concentration of ozone was adjusted so that the time required to modify the layer was appreciably longer, and more reliably controlled. For this apparatus, 11 minutes and 30 seconds was the required time for breaking of 80% of the carbon double bonds.

#### 2.4: Nylon 6-6

We used the nylon bond as the connecting bond in our covalent nanoglue. Nylon is a generic name for a family of synthetic copolymers. These copolymers are produced by condensation reactions, which are a type of reaction that involves the splitting out of some small molecule from the functional groups of the monomers. For condensation

polymerization, the monomers are different. For our experiments, one monomer is carboxylic acid and the other is an amine [Bettlehiem, 2001]. These match those on the SAMs of either surface.

The nylon bond is created between a carboxylic acid and an amine. The nylon bond is a covalent bond, as is required. Carboxylic acid is a weak acid in solution, characterized by the carbonyl group. It has the formula  $\text{COOH}$ . The amine molecule is a weak base in solution. It has the formula  $\text{NH}_2$ . To form nylon, the carboxylic acid loses a  $\text{OH}^-$  molecule, and the amine loses an  $\text{H}^+$  [Brady, 1981].

Nylon bonds are formed by condensation reaction, in which a small molecule splits out from the reacting monomers. For condensation polymerization, the monomers are different. The fundamental reaction is the splitting out of water between the carboxyl functional group and the amino functional group to form an amide [Bettleheim, 2001]. For our experiments, one monomer is a dicarboxylic acid and the other is a diamine. Diamines and dicarboxylic acids are molecules that have the same functional group on both ends. The dicarboxyl can bond to a diamine on either end, and vice versa. This is what gives these monomers the ability to make long chain fibers. The most well known is nylon 6-6, formed by the reaction of hexamethylene diamine and adipic acid. In the synthesis of nylon 6,6, hexanedioic acid (AA for adipic acid) and hexamethylene diamine (HMD) are dissolved in aqueous ethanol and heated. The 6-6 designation comes from the fact that each constituent molecule contains six carbon bonds between the end functional groups. There are different types of nylon, classified by the number of carbon atoms that are contained in the constituent molecules.

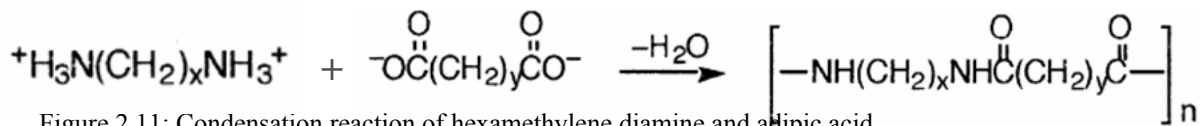


Figure 2.11: Condensation reaction of hexamethylene diamine and adipic acid.

The adipic acid contains the carboxyl and the hexamethylene diamine contains the amine. When the condensation reaction takes place, they form long molecular chains that have remarkable longitudinal strength [Brady, 1981].

Many carboxylic acids are synthesized by oxidizing primary alcohols with a strong oxidizing agent such as potassium permanganate. Carboxylic acid is characterized by the carbonyl group. It has the formula COOH. Because  $-\text{COOH}$  functional groups are acidic, the form in which they exist in an aqueous solution depends on the pH of the solution. If the carboxylic acid is dissolved in water, with an initial pH of 4.0 to 5.0, the solution will be slightly acidic due to ionization of the carboxyl group. If HCl is then added, enough to bring the solution's pH to 2.0 or lower, most of the carboxylic acid molecules will be in their unionized form ( $-\text{COOH}$ ). When the pH of the solution is brought to about 8.0 or higher, (more basic), most of the carboxylic molecules are present in their ionized form ( $-\text{COO}^-$ ) [Bettleheim, 2001]. The carboxylic acid in an aqueous nylon solution is self-catalyzing. Carboxylic acid can be derived from vinyl either chemically, or by ozonolysis and hydrolyzation.

The amine molecule has the formula  $\text{NH}_2$ . The polymerization of nylon is a complicated process of self-catalyzation for the adipic acid and protonation of the hexamethylene diamine. It is illustrated in Appendix A.

Before polymerization, a crystalline, solid “nylon salt” can be formed at room temperature using an exact 1:1 ratio of the acid and the base to neutralize each other. To attain polymerization, the original salt was heated to 260°C in an autoclave at 15 atm. This produced long polymer chains with a molecular density of 10,000 to 20,000 g/mol [Bettleheim, 2001]. Polymerization occurs at temperatures between 150° – 285°C.

The key to the minimization of energy in the covalent nanoglue, and to bridging the gaps between the wafers, is the formation of a nylon salt. Crystallization of this salt can take place either using the functional groups of the SAMs deposited on the sample wafers, or within the bonding intermediary. The most successful intermediary bond was achieved with nylon 6-6.

Before polymerization, nylon 6-6 forms an ionic salt at room temperature, 20°C, called hexamethylene diammonium adipate. In this crystallization process, the hydroxyl of the carboxylic acid functional group gives up its hydrogen nucleus (a proton), making the functional group  $\text{COO}^-$  with a net negative charge. The hydrogen is picked up by the amine, giving it a net positive charge,  $\text{NH}_3^+$ . The salt forms a crystalline lattice that is held together by the electrostatic attraction between the ions. The SAMs on the wafer surfaces have the same functional groups as the monomers, and are included in the crystalline lattice. This ionic attraction is thought to lead to the shortest-distance bridging that is most desirable to create our bond.

Crystalline hexamethylene diammonium adipate has a monoclinic structure, in which the cell dimensions are  $a = 5.57 \text{ \AA}$ ,  $b = 15.48 \text{ \AA}$ , and  $c = 9.07 \text{ \AA}$ . This is a parallelepiped with a parallelogram as the base face. The angle  $\alpha = 114^\circ$  [Hirokawa, 1954].

The cell contains two molecules. Hirokawa et al. contends that the structure may be described as consisting of ionic layers, in each of which both component ions orient their molecular axes nearly parallel to each other. The planes of each zigzag chain, however, are inclined at approximately  $65^\circ$  to each other. The packing of the ions in the layer is a kind of deformed two-dimensional closest packing [Hirokawa, 1954].

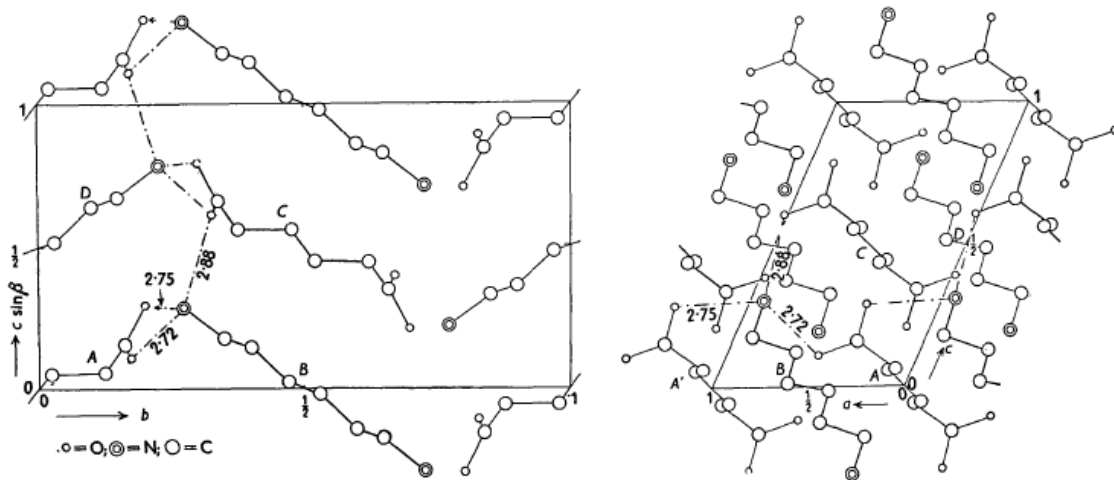


Figure 2.12: Hexamethylene diamonium adipate. This nylon 6,6 salt represents the minimum energy configuration.

The energy being minimized in this crystallization is the interactive electrostatic energy between the ions. According to Kittel, the long-range interaction between ions with charge  $\pm q$  is the electrostatic interaction  $\pm q^2/r$ , attractive between ions of opposite charge and repulsive between ions of the same charge. The ions arrange themselves in whatever crystal structure gives the strongest attractive interaction compatible with the repulsive interaction between ionic cores [Kittel, 2005].

## 2.5: Polymerization

To initiate polymerization, the nylon salt, unstable at high temperatures, must be raised to polymerization temperature. The value of this parameter is not set, according to several sources, ranging from 150°C to 285°C. When free to move and be stretched or rolled, the polymer fibers may line up into a pseudo-crystalline form.

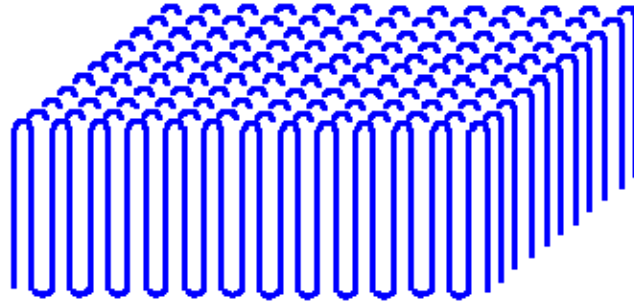


Figure 2.13: Polymer chains can fold into quasi-crystalline formations called lamella. From the University of Southern Mississippi.

“According to X-ray evidence (Bunn 1939; Bunn & Garner 1947) double orientation of the polythene and nylon crystallites is produced on rolling, the chains being oriented in the direction of rolling and, in addition, certain crystalline planes being arranged parallel to the polymer sheet.” [Ambrose, 1949]

The fibers fold up into quasi-crystalline formation called lamella. Therefore, even after polymerization, there can be a quasi-crystalline structure in the nylon.

In this study, the fibers, once polymerized, are not free to move, since they represent the minimum bond and are tied directly from one wafer to the other, so retain the minimum energy formation of the salt phase. The orientation of the polymer chains can be determined by using polarized infrared light absorption or scattering. From this inability to be rearranged after polymerization, we can determine the crystallization orientation of the nylon salt

between the wafers. Silicon, transparent to IR, should pass the polarized light so that the nylon film in between the wafers can be studied.

“Infrared absorptions measurements, using polarized radiation, provide another means of determining the orientation of polymer molecules in a fiber. The effect of drawing on the infrared dichroism of nylon 6,6 filaments has been reported by Quynn and Steele. These workers found that the four absorption bands they studied in the 3-micron region exhibited parallel dichroism at low draw ratios and, as drawing progressed, switched to exhibiting perpendicular dichroism.” [Caroti, 1956]

Though our nylon structures are not undergoing such radical deformation, with the previous crystalline structure in place they should retain the dichroistic properties even after polymerization.

## 2.6: Force Table Design

The apparatus used to measure the force consisted of a servo-driven anti-backlash linear bearing table, built by the previous student [Walker, 2006] for sliding force measurements, and modified for this work to measure normal forces. The vacuum collar was replaced with an L-rail bracket stage and bolted holding clips. The 1 oz sensitivity cantilever force sensor was also replaced, with a 20 lb sensor. The table was recalibrated to gather data from this large-force sensor.

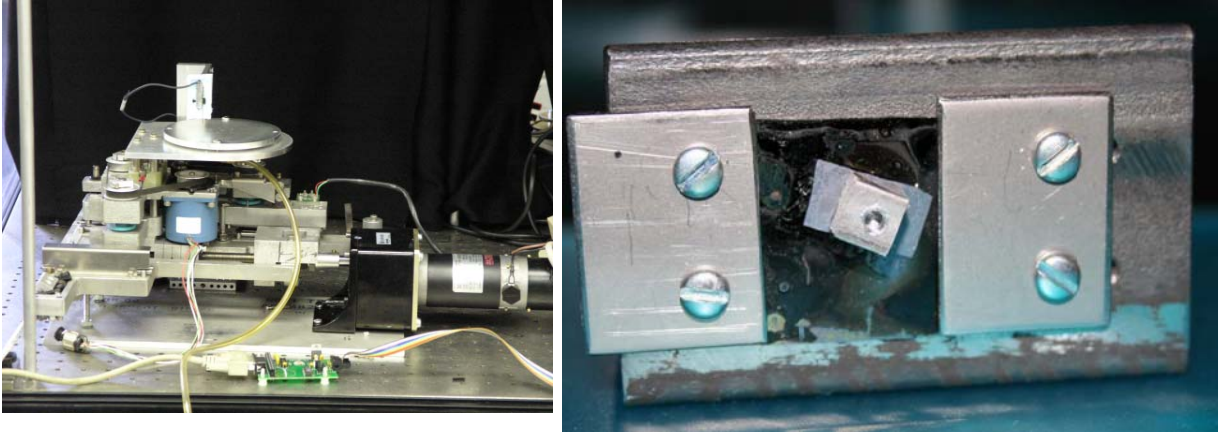


Figure 2.14: The vacuum collar was replaced by an L-rail stage. Because the stage used the same mounting as the collar, the stage height could also be controlled.

The pulling block was mounted to the top wafer with super glue, and connected to the sensor with a 3cm 2-32 thread bolt. The motion of the table provided the mechanism for measuring the amount of force needed to break the nylon bond.

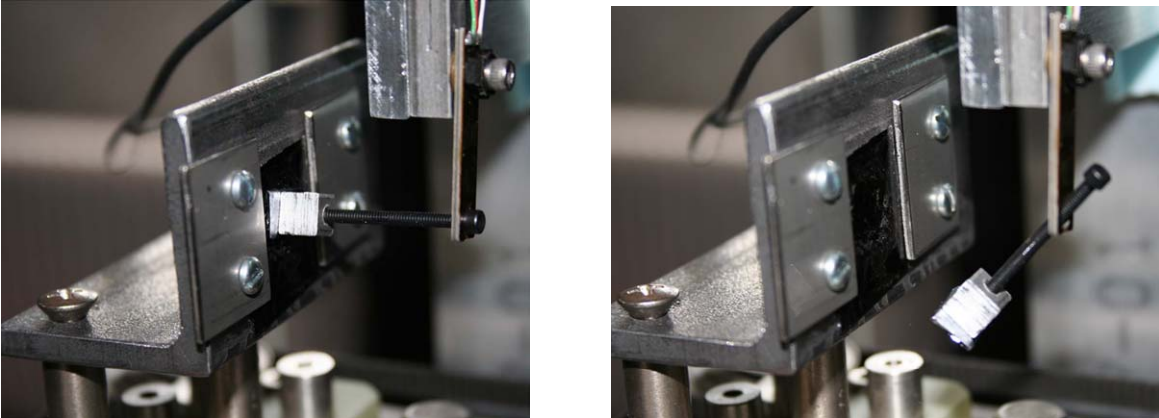


Figure 2.15: When the motor of the table is activated, the measuring program begins simultaneously. The force is measured until the nanoglue breaks or the pulling block comes off.

## 2.7: Conclusion

The RF array 3-D package described here makes novel use of existing, well-developed technologies based upon industrially viable materials. The materials used are shown to be compatible with processing of the finished package. Each process required specific materials, or the end product of another process. These included wafer cleaning, which prepared the wafer surface for other processes; SAMs deposition, which creates a single, uniform and modifiable surface on the wafer; alignment pattern creation; ozonation; and bonding.

Self assembled monolayer (SAM) formation on the silicon oxide surface of thin wafers is one of the integral processes used in these experiments. SAMs are long-chain molecules that create a single layer on a surface, formed by liquid or vapor deposition. Using SAMs, the surface characteristics of the wafer can be changed to field many types of reactions.

Reactive cleaning of the substrate is the initial step necessary in the preparation of the wafer for deposition. This type of cleaning uses an exothermic reaction of a strong acid and a strong base to remove dust and other contaminants from the substrate surface. An effective reactive cleaner is piranha solution.

Development of a reliable oxidation method is required for the modification of our SAMs functional group. One method is oxidation by solution. The solution is composed of potassium permanganate, sodium periodate, and potassium carbonate. This method is slow, requiring at least 24 hours. This method is also messy and requires disposal of waste product and does not give 100% modification of the vinyl-termination. It gives ~ 20% based on

contact angle. Another method is the use of ozonolysis (exposing the surface to ozone) and hydrolization. Ozone is a faster, more complete method of oxidation. Ozone has several advantages over an oxidizing solution. Ozone is a powerful oxidizer. The flow of the ozone can be controlled, so that overall coverage of the substrate surface is more likely. Ozone works faster than the solution, and produces less waste. Also, ozone does not need to be stored, but can be generated at anytime with pure O<sub>2</sub> or dry air. Ozone preferentially attacks a carbon double-bond. The 10-UTS molecule contains one carbon double bond in the terminating vinyl group, so the carboxyl group forms near the terminal end.

The ozone delivery system consists of three major components: the delivery chamber, the ozone generator, and the dry air source. The ozone delivery system was lab built. It consists of one quartz tube, one Pyrex glass funnel, two rubber pipe connectors, one PVC pipe connector, and an ozone sensor. The delivery chamber was designed to allow an evenly distributed flow of ozone to be delivered onto a sample with the vinyl-terminated SAM deposited on its surface. The entire apparatus was located under a fume hood, because ozone is a biohazard. The base of the ozonator was surrounded by a shield to keep the airflow from the fume hood from disrupting the even flow of ozone out of the chamber.

Three modes of operation were used: flowing ozone/dry air into the chamber, generation of ozone by UV absorption in the chamber, and generation of ozone by corona discharge into the chamber, to determine which method was more effective and reliable. Most of the work reported utilized an external ozone generator.

The nylon bond was used as the connecting bond in our covalent nanoglue. Nylon is a generic name for a family of synthetic copolymers. These copolymers are produced by

condensation reactions, which is a type of reaction that involves the splitting out of some small molecule from the functional groups of the monomers. The key to the minimization of energy in the covalent nanoglue, and to bridging the gaps between the wafers, is the formation of a nylon salt. Crystallization of this salt can take place either using the functional groups of the SAMs deposited on the sample wafers, or within the bonding intermediary. The most successful intermediary bond was achieved with nylon 6-6.



achieved, bonding the wafers together could take place with additional lithography or deposition steps. Finally, using this type of bonding would improve thermal conductivity within the unit, because the adhesion takes place between a very thin layer of integral components of the unit, rather than through additional layers of intermediary materials. The SAMs utilized to create the nylon bond were 10-undecenyltrichlorosilane and (Aminoethyl aminomethyl) Phenethyl trimethoxysilane. This bond is formed in the reaction of the two different functional groups, or monomers, located at the ends of the two organic SAMs molecules. The functional groups at the ends of these SAMs, a carboxylic acid and an amine, combine through a process called a condensation reaction, as was noted in previous chapters. Amino acids form bonds in the same way, called peptide bonds. The chances of getting covalent bonding between the layers are favorable, under the right conditions. The SAMs layers are very regular and it is possible to construct a single, predictable layer upon the substrates. This makes it possible to get a very close correspondence between the terminating functional groups that would be needed to make the covalent bond as effective as possible.

In figure 3.2a, two-inch wafers were bonded without the use of an intermediary. On the left, the wafer was coated with carboxylic acid-terminated SAMs, and on the right, the wafer carried the amine-terminated SAMs. These samples were produced in accordance with the procedure described in [Walker, 2006].

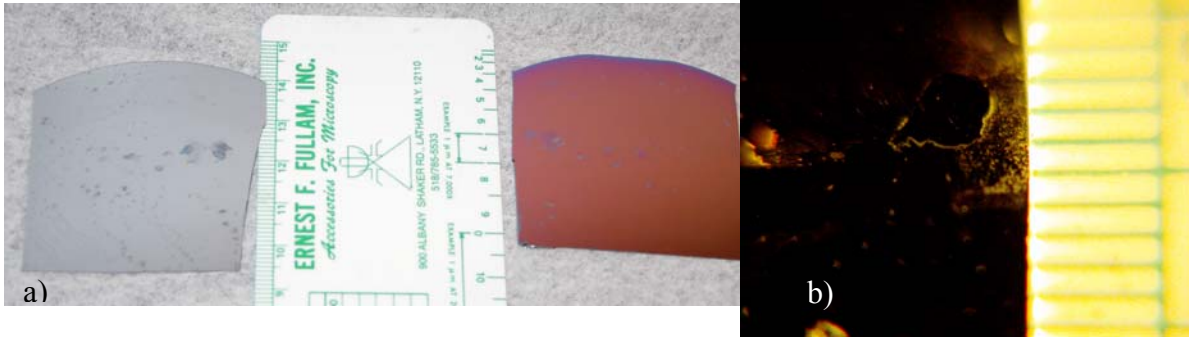


Figure 3.2: a) The SAM-only bond was achieved in localized, millimeter-sized patches. The strength of the bond exceeded the Si-Si bonds. 3.2b) dark-field illumination shows where the silicon was removed from one of the samples as a result of the rupture of silicon rather than the bond. The size of the bonded regions is a few millimeters to a side. This is likely due to the fact that the SAM layers were only in contact over such small regions due to their short length and lack of perfect flatness of the wafer.

To make this bond, the following procedure was used:

- 1) Each 2-inch wafer was cleaned as previous described.
- 2) The top wafer was coated with 10-UTS and the bottom wafer was coated with PEDA.
- 3) The termination of the 10-UTS was modified by oxidation solution.
- 4) The wafers were placed active terminated sides together, on a heat source at 285°C. A weight of 125.673 N was placed on the samples. This weight consisted of a foil-covered lead block.
- 5) The wafers were heated under weight for one hour.

The “bare” bond was achieved. This sample was pulled apart manually, using a sharp implement to pry apart the wafers. The bonding occurred in millimeter-sized regions. The bonding of the SAMs exceeded the silicon-silicon bonds, as shown in figure 3.2b. The delicacy of the wafers proved to be a challenge to provide sufficient pressure to deform the Si

and increase the area of the bond, but this could be over-come by use of a thinner top wafer, which would require less pressure to bring the surfaces together. It is important to note that the wafers did not bond without heat and pressure, which supports our contention that it is a covalent bond forming as we discussed. We next elaborate on the obvious problems with this approach and their solutions.

### 3.1.1: Bare-SAM Bonding Difficulties

Making this bond with only SAM layers presents certain challenges. One of the difficulties comes in with the variations or irregularities in the substrate surfaces that are orders of magnitude larger than the combined lengths of the deposited monolayers.

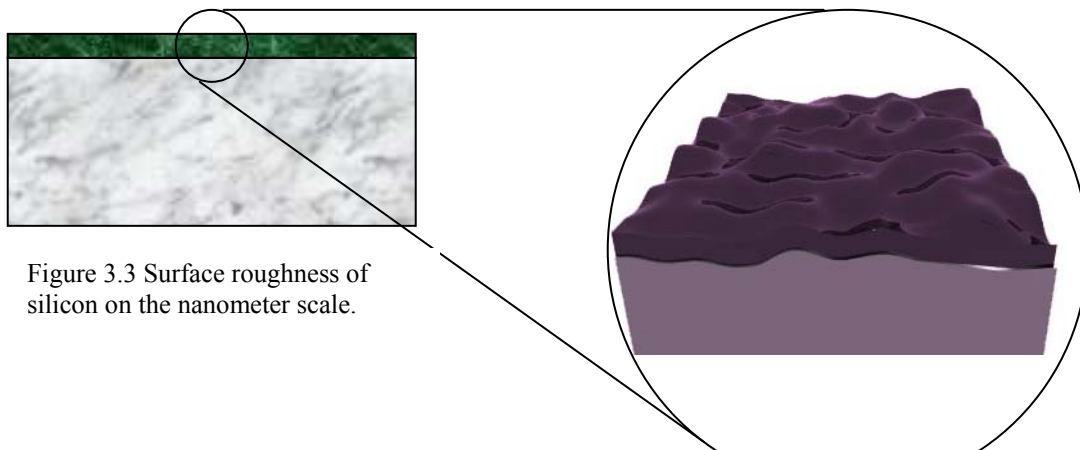


Figure 3.3 Surface roughness of silicon on the nanometer scale.

The surfaces of the experimental silicon wafers, though polished, were still rough on the micron scale as slow undulations on 10's of nanometers, much larger than the 25 nm thickness of the SAMs. Variations in the surfaces of these wafers kept nylon from forming across the whole surface of a rigid sample, as was observed in figure 3.2 in the bare bond. The height of the SAMs molecules, 9 nm and 16 nm, had a total height that was less than the surface features of the wafer surfaces, an average of  $\lambda/10$  or  $\lambda/20$ , where  $\lambda \sim 500$  to 700 nm, a

25 to 75 nm variation. This is a possible explanation for the spotty bonding of the SAMs-only samples.

Two solutions are evident: use of a very thin, deformable wafer or use of an intermediary can be used to bridge the gap, so that the bond will form, regardless of the surface roughness on the nano-scale.

Another difficulty was finding the right conditions under which the nylon bond will form. The use of molecules anchored to a fixed surface restricts the motion of the molecule. Conventionally, the condensation reaction takes place in an aqueous solution,

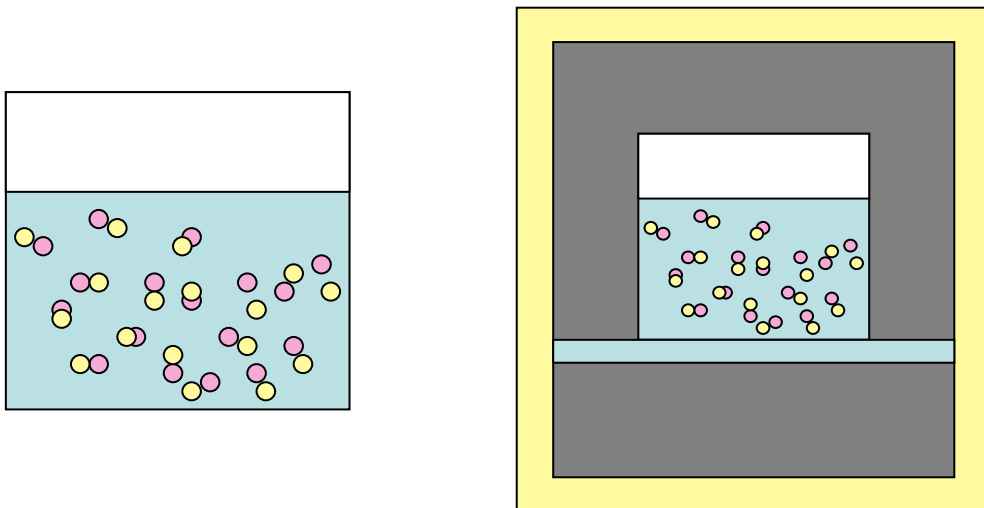


Figure 3.4: Monomer molecules are free to move. All documentation on nylon formation is for free molecules. Conventional recipe for nylon requires an autoclave. Such conditions may be unsuitable for wafers.

which does not restrict the available angles and positions coordinating for bonding. All documentation on nylon formation has been for molecules that are free to move, not molecules anchored to a surface, which raises questions of configuration issues during the bonding process. Thus the constraints, both in motion and relative angles between the molecules, have not been explored. The fact that strong nylon bonds were observed in the SAMs-only case (even if spotty, due to other reasons), indicates that the orientation constraints are not significant.

A “wet” environment was needed to make the bond form between fixed molecules. Attempting to reproduce the conditions to form nylon using two flat surfaces in which different surface properties were involved was problematic. The production of the original nylon fiber commonly known nylon 6,6 fiber required heating in an autoclave to 250°C and 15 atm. This created nylon of a high molecular weight. Attempting to reproduce these conditions with silicon wafers would result in damage to the samples and any circuitry printed on the wafers. Fibers of high density would be ideal for the bonding requirements. The intermediary fibers should be short, and they need to extend straight across from one surface to the other. Controlling the growth of the fibers to these specifications was achieved by allowing the solution to crystallize (section 3.6.3).

A final difficulty was ensuring that the 10-UTS SAM is correctly terminated with carboxyl. The self-assembled monolayer produced by the 10-UTS molecule was vinyl-terminated, as described in [Wasserman, 1989]. There are different ways to convert the vinyl to carboxylic acid, including immersion of the sample in an oxidizing solution. The wet

chemical method, however, was slow and gave a relatively low carboxyl yield, which can affect the effectiveness of the bonding procedure. We use the previously described ozone method. In later trials, carboxylic acid was produced using ozone. This method of carboxyl production proved faster, cleaner, and more effective than previous methods.

Several strategies that were devised in this work to counter these problems:

- 1) Applying pressure to the top wafer, making it deform without breaking, to conform the topography of the bottom wafer;
- 2) Using an ultra-thin top wafer, (polished to 30-60 microns or silicon on insulator which is 2 to 5 microns thick) which, if thin enough, naturally conforms to the surface of the bottom wafer;
- 3) Using an “intermediary,” long chains of molecules with the same functional groups to span the gap;
- 4) Reproduce the conditions under which conventional nylon is formed between the wafers either by immersion or titration;
- 5) Using ozone to convert the vinyl functional group to carboxylic acid.
- 6) Combinations of these methods were also be used.

These experimental trials initially used applied pressure to achieve wafer to wafer contact. This method was successful in creating nylon bonding directly between SAMs layers, but the bonding was spotty.

In other trials, an intermediary was used to make the bond. These trials were also successful and more consistent in terms of bonding coverage. The use of the intermediary

also provided the proper conditions for bond formation. Much of the work described in this chapter is the optimization of the crystallization of intermediate layers.

### 3.1.2: Bonding Requirements

The bonding takes place through a process that will create a nylon bond between the stacked wafers when alignment of the vias has been achieved. To be successful in building an RF array module, the bond must meet certain criteria.

The bonding should be semi-permanent to permanent. The goal, therefore, is to make a covalent bond, which is one of the strongest chemical bonds possible. Under normal operating conditions, there should be no change in the bond strength or integrity. Epoxies might change chemically over time, eventually de-bonding. The bond produced in this study should not suffer such changes in composition, nor degradation.

The bond should have mid-range to high temperature tolerance. This bonding must withstand operational temperatures within the module.

The bonding cannot be instantaneous. This process should only take place after the alignment has been completed. Epoxies and cyano-substrates have certain time constraints on their bonding effectiveness. This bond is controlled by the amount of solvent left between the substrates and the moment that the constituents are brought to polymerization temperature, which are entirely in our control.

There must be constituent compatibility in this process. The bonding process should utilize constituents that can be integrated into the chip design. Regular bonding agents do not make use of these constituents, and therefore do not offer as reliable a bond.

Fewer by-products should be produced from this process. By-products from more harsh bonding techniques can collect and cause bond failure. According to [Neiman, 1962], thermal degradation can lead to the evolution of such by-products as carbon monoxide, methane and propylene beginning at 200°C [Brady, 1981]. Acid by-products can cause oxidation of the chips, destroying them. Gaseous by-products can create air pockets that will expand when heated, causing cyclic stress that will reduce the device's lifetime. This prohibits the use of thick layers of many common bonding agents. The by-product from our bonding agent is molecular water, and the amount generated should be small enough to be of negligible effect.

### 3.2: Thin Silicon

One solution to the “bare” bond challenge is to use ultra thin wafers, 10 microns or less thick. Bare bonding using SOI (silicon on insulator) wafers has many advantages. They can deform to match another surface, as shown in the cut-away figure of 10-UTS and PEDAs between silicon and thin silicon in figure 3.5 below.

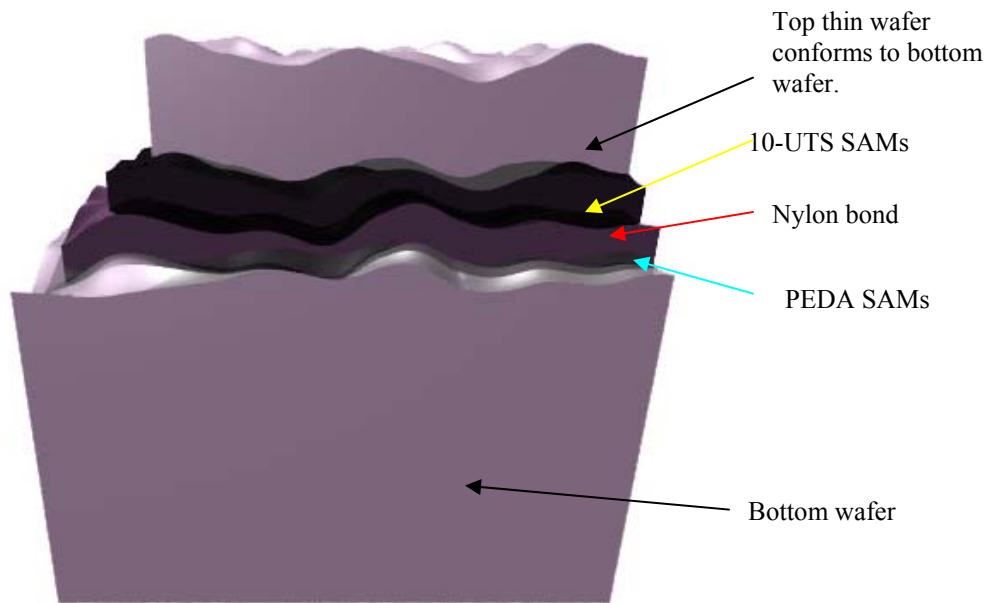


Figure 3.5: A cut-away example of thin wafer use in the bonding process. SOI wafers are thin enough to conform to the surface of the thicker bottom wafer, eliminating the need to apply pressure for bonding.

Using ultra thin wafers has one main disadvantage: the fragility of the top wafer. Though the fragility makes handling the wafer difficult, especially with all the different washing and deposition immersion processes required to produce the final sample, these wafers are ideally suited to the formation of vias, and may be used in the RF package. These wafers have handles that are thick enough to mitigate the fragility issues. When the handles are removed, the wafers are thin enough to conform to the bottom wafer, and get good contact. The removal process, however, which requires the immersion of the entire sample in HF, is inimical to the nylon salt between the wafer.

### 3.3: Intermediary bond

An alternative method to achieving a covalent nanoglue between wafers is through the use of intermediary molecules that possess the same functional end groups that terminate the SAMs molecules. These intervening molecules, bonded end to end, if oriented correctly, can span the gaps between the SAMs.

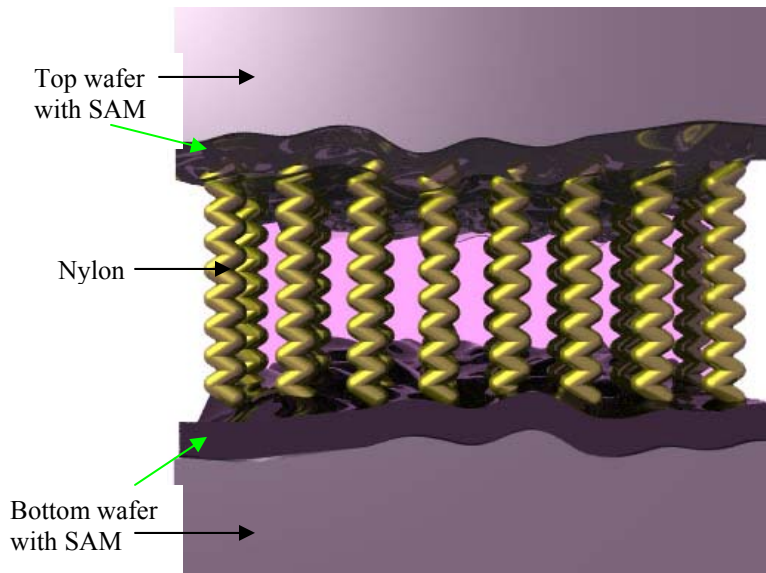


Figure 3.6: The SAMs have the same functional groups as the constituent monomers of nylon; therefore, nylon can be used as an intermediary to fill in the gaps between the SAMs that are caused

As stated previously, the upper and lower SAMs have the functional groups carboxylic acid and amine, respectively. Under the right conditions, these monomers combine to form nylon, but irregularities in the substrate surface are a major hindrance. Regular nylon fibers use dicarboxyls and diamines, such as adipic acid and hexamethylene diamine. These molecules will continue to make chains as long as there are reactants. If these long chains can be made to react within the gaps between the wafers, the PEDAs should react

with chains ending with a carboxyl, and the 10-UTS should react with a chain ending in an amine. If the solution is made dilute enough, it is theoretically possible to limit the length of the chains so that the terminals of each chain links with a wafer molecule instead of another chain. The solution will also have the proper characteristics to be used as the liquid alignment mechanism.

The main disadvantage to using this bonding method is that there would need to be special areas for the bonding solution to act. The flow channels for alignment would have to be in areas where vias are absent, or the nylon salt could cover the vias and prevent contact between substrate layers. This might complicate the design of the circuitry in the wafers to include sections that allow for the solution, whereas bare SAM to SAM bonding would not require such precautions.

#### 3.4: Low Magnification View of the Bond

The bond uniformity can be investigated through IR imaging. Silicon is transparent to infrared radiation. Double-side polished silicon is required for this imaging, because the two polished sides transmit the IR without scattering. Using an IR source, such as an incandescent light bulb, and a Si CCD camera with IR filter removed, the thin film of nylon between the silicon wafers can be viewed. The CCD camera observes a narrow wavelength range of infrared, that which is transmitted through the wafers, but is still detectable with the Si sensor.

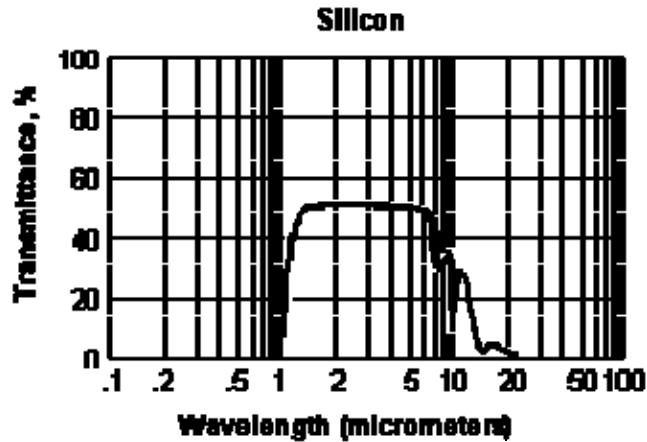


Figure 3.7: Silicon is transparent to infrared in the 1.5 to 8 micron range. *Almaz Optics, Inc.*

We used a Nikon dissection microscope with the CCD camera, mounted on an adaptor and placed into one of the eyepiece tubes. The stage was replaced with a flat glass platform, coated with aluminum foil except for a small aperture. The foil cuts out the overflow brilliance around the edges of the sample from our IR source. A video capture program allows still pictures or short movies to be obtained from the setup. The image is monochromatic because the charge-coupled device in B/W cameras is sensitive to infrared in the 1.1 micron range [Gilblom, 2004].



Figure 3.8: The original, low power microscope that was used to view bond. The IR filter was removed and the stage was replaced with a glass platform and incandescent light source.

The thin film of nylon between the wafers showed interference patterns. The interference fringes, or Newton's rings [Hecht, 1987], are due to the variation of the thin layer of nylon between the silicon wafers. The pattern is composed of different regions of concentric rings. The observation of a strong interference pattern for nm-monochromatic light is unexpected. The reason is that the bandwidth of light is actually quite narrow, given by the competition between the Si absorption at shorter wavelengths and the loss of Si-sensor response at layers' wavelengths. Only wavelengths at the absorption edge will meet both criteria. Although they will be strongly absorbed, the background light level is low, so the pattern is observable.

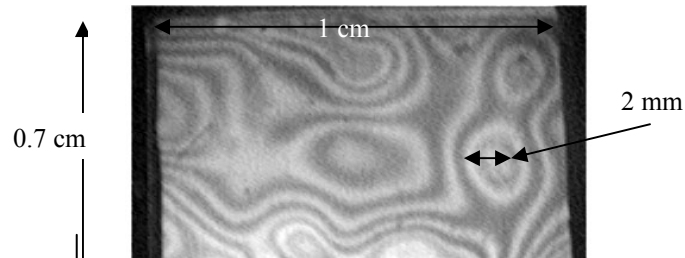


Figure 3.9: The bonding can be viewed when infrared light is shone through double-side polished silicon. The patterns of light and dark are the result of variations in thickness of the nylon between the wafers.

The undulations on the surface of the silicon wafers act as thin convex lenses to the IR, in the Newton's rings analogy with a thin film, the nylon, between them.  $R$  is the radius of curvature of the silicon lens and the radius of the  $m$ th bright ring is  $x_m$ . The thickness of the nylon film is  $d$ .

$$x_m = [(m + 1/2)\lambda_f R]^{1/2} \text{ [Hecht, 1999]} \quad (3.1)$$

In this equation,  $\lambda_f = \lambda_0/n_f$  and  $n_f$  is the index of refraction of the nylon film,  $n_f = 1.565$ .  $\lambda_0$  is the infrared wavelength at the silicon transparency edge,  $\sim 1.1$  microns. From bright to bright or dark to dark is  $1/2$  wavelength divided by the index of refraction for  $\sim 1.1$  micron light.

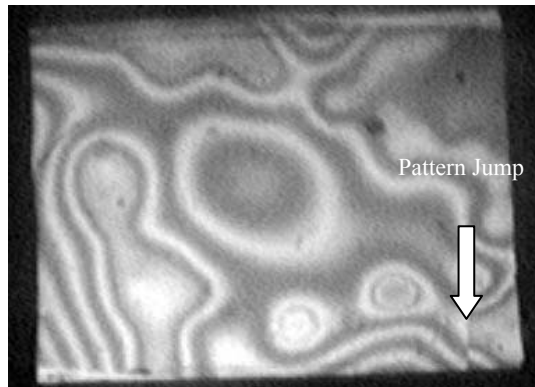


Figure 3.10: Sudden changes in the pattern may be due to air pockets.

Thus  $\lambda_f = 0.70288 \mu\text{m}$ . When  $m = 2$  and  $x_m \sim 2$  mm, as shown in figure 3.6, then the local radius of can be solved for:

$$R = \frac{x_m^2}{\left(m + \frac{1}{2}\right)\lambda_f} \quad (3.2)$$

The local radius  $R = 2.276$  m, and the thickness of the nylon is

$$d = \frac{x^2}{2R}. \quad (3.2)$$

The thickness is  $d = 0.878$  microns at this point. The relative thicknesses of the nylon at different points between the wafers may be calculated in this way.

Any jumps in the pattern are likely due to changes of reflectivity at the interface/index of film due to an air gap, i.e. defects of the nylon layer (such as air bubbles). Low resolution interference imaging is an effective way of screening the whole wafer for large bonding defects. Figure 3.10 shows effective transmission of the bandwidth due to wafer flatness and shows a jump in the pattern at the indicated point. It jumps by  $\frac{1}{2}$  fringe, which corresponds a  $\pi/2$  phase change in the beam reflected from the first surface of the nylon layer.

$$x_f = [(m+1)\lambda_f R]^{1/2} \quad (3.3)$$

From the center of the nearest set of concentric rings to the jump in the pattern is  $x_m \sim 3.3$  mm. The local radius  $R = 3.099$  m and the change in thickness of the layer is  $\Delta d = 0.1755$   $\mu\text{m}$ .

### 3.5: High Resolution View of the Bond

A high resolution, high magnification microscope permits differentiation of surface and interface contributions to the image, due to the shorter focal length used. It can be used to quantify small (point) defects in the bonding layer. This microscope is capable of differentiating between the top and bottom of even the 15 micron thick wafers.



Figure 3.11: To avoid the interference effects, a higher power microscope, with a shorter focal length was used. This high magnification microscope is capable of discerning the interfaces between the nylon and the wafer, and of differentiating between the top and bottom of the 50 micron thick wafers.

Again, IR light from a tungsten lamp and a Si CCD camera are used. The interference pattern due to slow nylon thickness variations is irrelevant at this higher magnification. The infrared filter was removed from the illuminator. Because the nylon layer is thinner than the microscope's depth of focus, the thickness of the nylon cannot be determined without distinctive features being identified at being located at the interfaces. When the interface is in focus, the surface is not in focus. In figure 3.11, interface defects can be seen in an arc through the middle of the image.

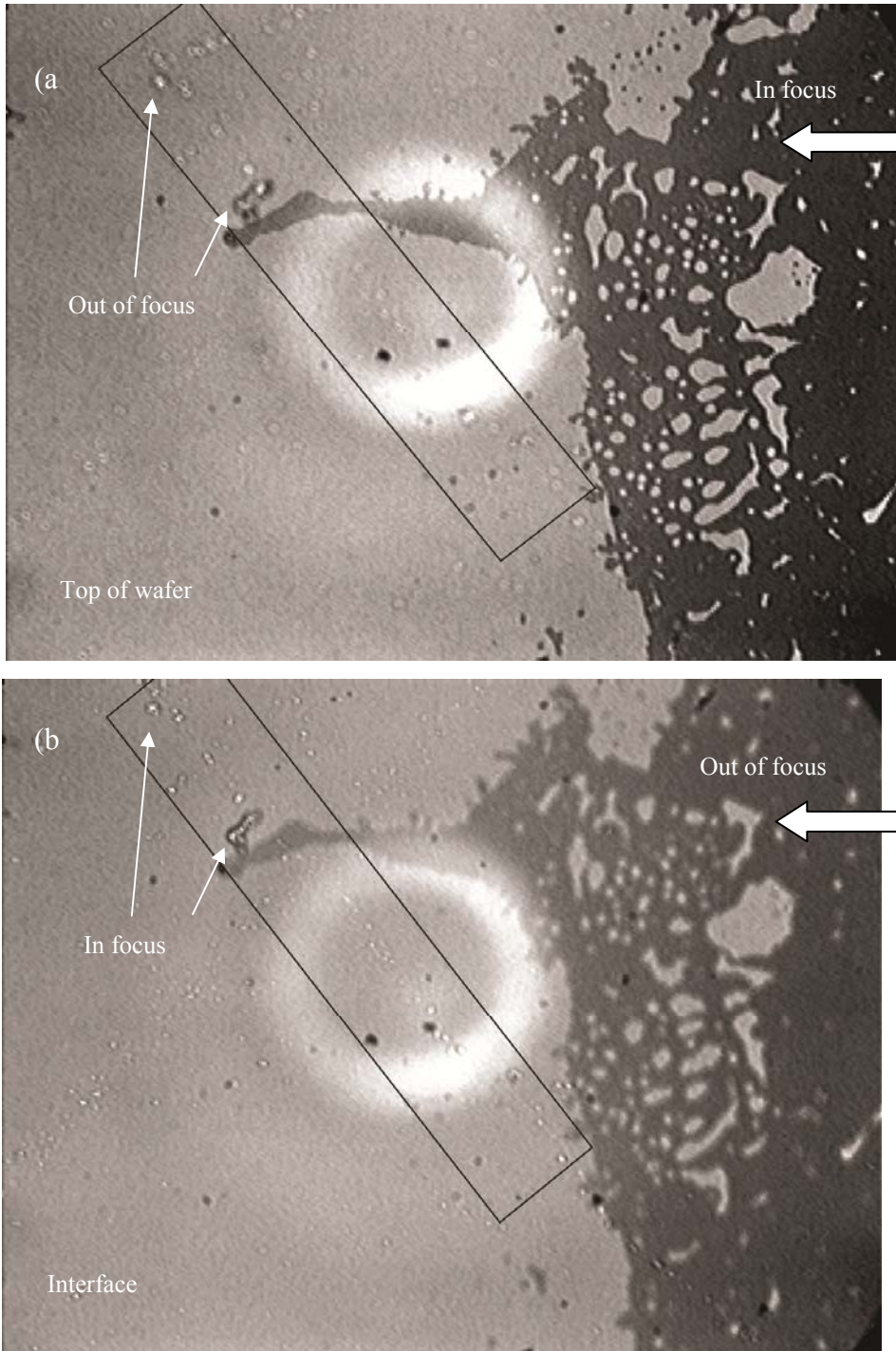


Figure 3.12: In this picture interface defects in an arc through the middle of the image. In the top image, a) the discoloration on the top of the wafer is in focus, while the defects are out of focus. Below, in b) the discoloration is out of focus, and the defects are in focus. The thickness of the wafer is approximately 50 microns. The arc of defects in the interface is delineated by the rectangles. This interface is thin enough that we see the whole interface at once.

### 3.6: Producing a Nylon Bond

To make the covalent nanogluue, several methods were attempted. All procedures used the following preparations. Vinyl- and amino-terminated SAMs were prepared on clean, single-side polished silicon wafers with surfaces of silicon dioxide. The wafers were cleaned in piranha solution, as described in [Walker, 2006] in section 4.2. The smaller top wafers were rinsed in organic solvents, then immersed in a 2% solution of 10-UTS in hexadecane. The smaller top wafer allowed room for the pulling clamps to be set without covering the top wafer. The bottom wafers were immersed in a 1% PEDA solution. Deposition occurred under a nitrogen environment. After a period of 24 hours, the samples were rinsed in solvents and removed from the nitrogen environment. The top samples were subjected to oxidation by solution or by ozonation and hydrolyzation to produce the desired functional group termination of carboxylic acid. Then a solution of adipic acid and hexamethylene diamine was introduced between the wafers using a pipette. In solution, the carboxylic acid of the adipic acid donates a hydrogen to the amine of the hexamethylene diamine at room temperature. Together, they form nylon salt that is ionically bonded.

To form nylon, which drives off a water molecule and covalently bonds the C to the N, the samples were heated to polymerization temperature, which ranged between 150°C to 285°C, depending on the density of the nylon.

Once the bond had been produced, the strength of the bond was measured as an indication of bond quality and reproducibility. An existing force table was modified to hold the sample surfaces for measurement of forces normal to the wafers sufficient to break the bonding between them at ambient and elevated temperatures. Previously, the free wafer

required in-plane lateral (gliding) forces at room temperature. The stage, originally designed move stacked wafers so that the frictional force between them could be determined, was redesigned to hold the bottom wafer in an orientation normal to the pulling force and reconstructed accordingly. Anchor blocks attached to the top wafer connected to the force sensor cantilever, which had a 20 lb capacity. This force table was capable of virtual-instrument computer-controlled force measurement and the acquisition and recording of the results. The force table additionally used a smooth DC motor actuation with encoder to pull the wafers apart. The bond cleavage stress is given by:

$$Stress = \frac{Force}{Area} = \frac{F}{A}$$

Where the area is approximately 1 cm<sup>2</sup>.

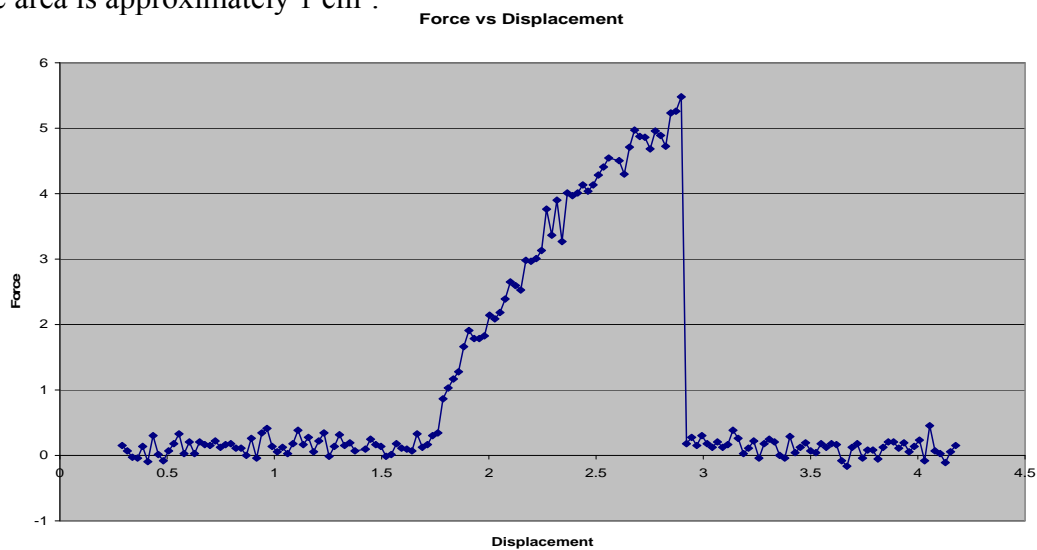


Figure 3.13: A plot of the force vs displacement pulling data.

Once the force sensor is engaged, there is a ramping up in the force reading. The force at the breaking of the bond in figure 3.13 is 5.5 N. Once the bond breaks, the force drops back to zero.

Several methods have been applied to produce an intermediary nylon bond the SAMs. The first of these was the use of condensed nylon, where thick nylon was pooled directly onto the samples. The second was immersion, where the SAM covered wafers underwent deposition by immersing samples in nylon solution. The third was the clamped method, in which dilute nylon applied with a pipette, clamped with alligator clips, allowed to dry in air and heated while clamped. The fourth was spun on nylon, where dilute nylon was spun on with a spin coater. The last method utilized a different family of nylons called aromatic nylon or Kevlar, in which different constituent molecules with same functional end-groups were used to try to achieve the bond.

### 3.6.1: Condensed Nylon

The initial method used was bonding with condensation from solution. Nylon 6,6 salt can be formed in aqueous ethanol. The HMD is soluble in water, and the AA is soluble in ethanol. The nylon salt remains soluble in this solution. The salt molecules in the suspension were used to bridge the gap from surface to surface. The volume of the solution was reduced by boiling, and hence the salt concentration was increased. The salt then condensed out as a slightly milky white substance.

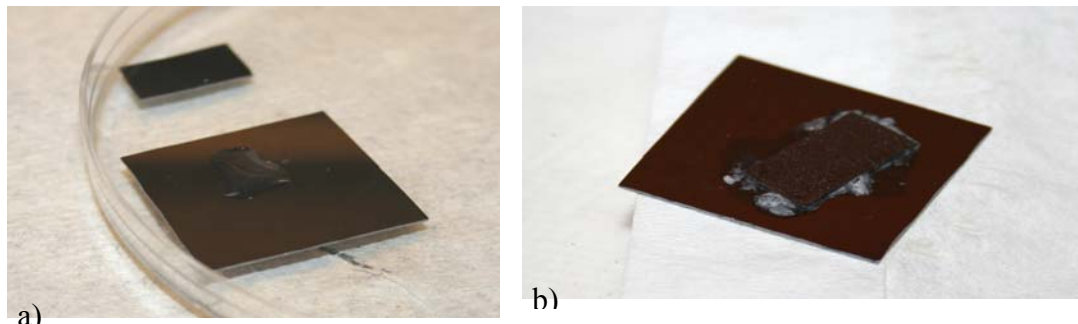


Figure 3.14: In 3.14a, the solution is dilute. Figure 3.14b shows the condensate of nylon at the edges of the top wafer before heating to polymerization temperature.

This condensate was used as the intermediate layer for the samples. It was pooled onto one wafer and the second wafer was placed on top. The condensate was still wet with aqueous ethanol, so that the conditions for nylon formation were believed to be present at the two surfaces. These conditions included having a wet environment to facilitate bond formation, and high pressure (15 atm) and heating to polymerization temperature. The samples were placed on a hotplate to bake off the remaining solvent, at 290 °C, which was slightly above the reaction temperature to form the nylon polymer. When the salt turned black, in approximately 30 minutes, and all the moisture has been driven off, theoretically, bonding should have occurred. The change in color could be observed at the edges where the condensate overflow was visible.



Figure 3.15: The condensate has turned black at slightly above polymerization temperature. The wafers have been pulled, and the force to break them apart measured.

This did not require an autoclave because high-density nylon was not necessary to meet the bonding goal [Bettelheim, 2001]. A covalently bonded chain from surface to surface was the goal, with nylon molecules bonded to the surfaces and to each other. This is unlikely, however, since the layer is thick and amorphous.

### 3.6.1.1: Results for Bonding with Condensed Nylon

While bonding with condensed nylon worked, this method was deemed insufficient to the demands of the 3-D package for several reasons. First, this method gave a crude bond. It is believed that this method did not work as covalently bonded nanoglue, but by long entangled strands that acted as a conventional glue, whereby the long chain polymers of the condensate entangled with each other rather than bonding from surface to surface. It is likely that some SAM-polymer bonding occurred, given the bond strength.

The bond required between 2 to 10 N of force to break apart, equivalent to 5.8 to 29.01 psi. This large variation in the breaking force indicates an unreliable bond, with low reproducibility. The bonding process in this case clearly requires refinement.

This method may still be useful as a removable bond. Such a bond is required for holding a thin wafer to a handle wafer or for holding a wafer during processing. The ability of the bond to soften with increasing temperature and be removable compensates for its reduced reproducibility. We discuss the thermal properties in section 3.6.3.1 for similar material

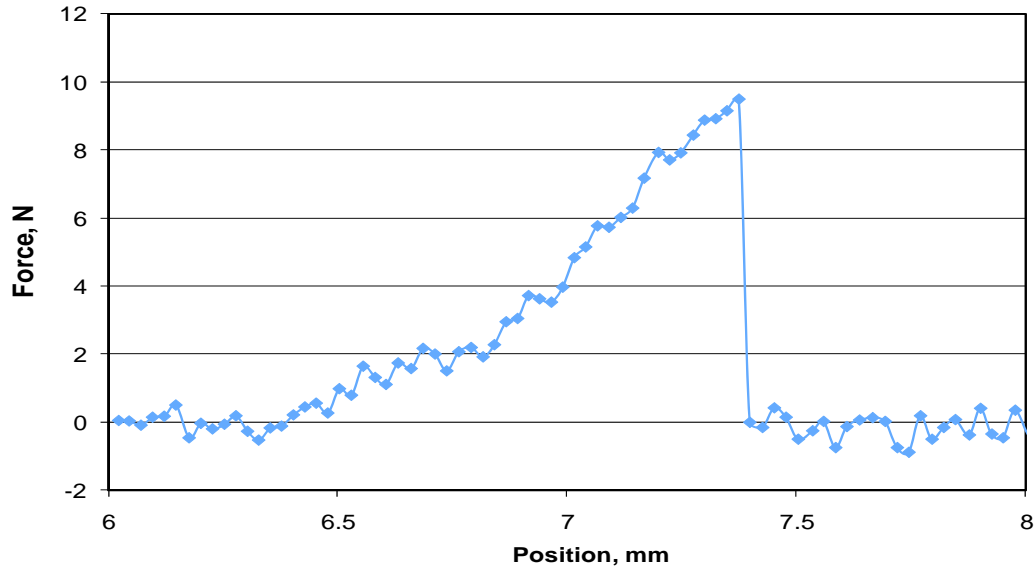


Figure 3.16: The initial force required to pull the wafers apart peaked at  $\sim 9.2$  N within 1 mm, seen in 3.14 a. A second sample required a force of  $\sim 11$  N, as shown in 3.14 b. The condensed glue bonded in the same manner as a conventional glue, which is unsuitable for the purposes of this study. Though the strength of the bond was significant, this line of experimentation was not pursued.

### 3.6.2: Nylon Immersion

The next method attempted was nylon immersion. This involved immersing the top wafer of the samples in a .0295 M nylon solution. Then the top wafer was placed onto the bottom wafer while this layer of solution on the lower wafer was still wet. The two samples were wrapped in foil and heated together under a 3 kg weight. This produced a binding pressure of 29.4 Pa given the  $\sim 1$  cm<sup>2</sup> test bonding area. The samples were placed in an oven at 200°C for 30 minutes.



3.17: The top wafer was immersed in a 0.0295 M solution of nylon, then placed on the bottom wafer and held in place by a 3 kg weight. Immersion proved ineffective as a method of bonding.

### 3.6.2.1: Results for Bonding with Nylon Immersion

This method, using nylon solution made from 0.0295 M of hexamethylene diamine in water and 0.0295 M of adipic acid in ethanol, gave a more even layer across the entire sample, but not a good bond. The internal pressure produced by the solvent boiling off often made the top wafer pop off in 3 out of 5 samples, destroying any impending bond. The weight was not sufficient to prevent this phenomenon from affecting the samples.

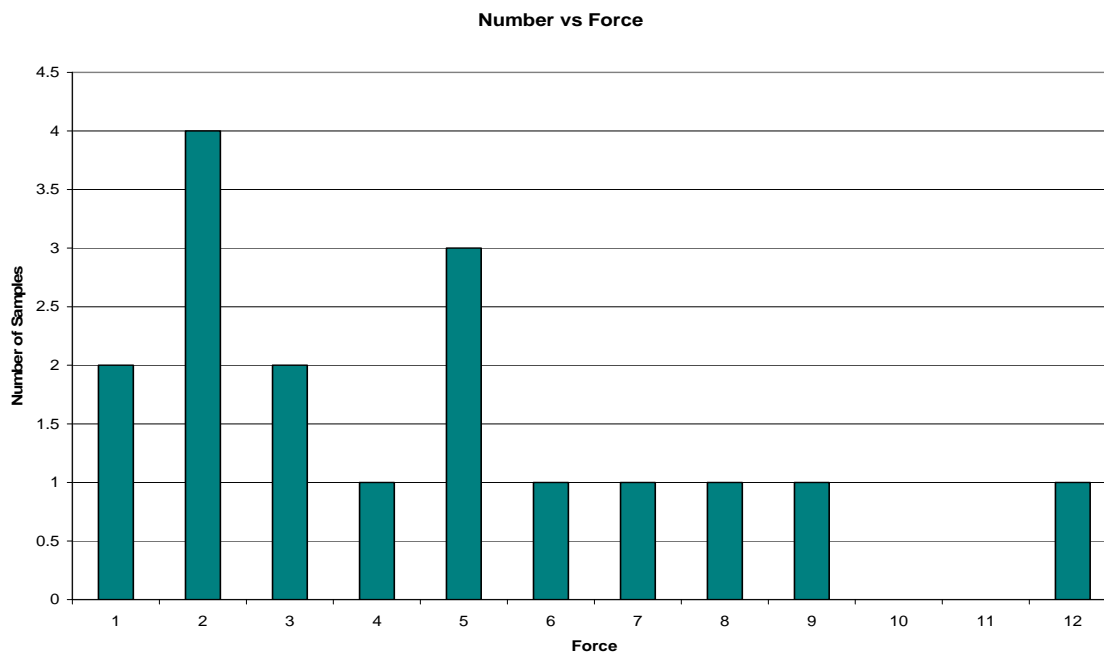


Figure 3.18: The bonding due to nylon immersion was not consistent, ranging from 1 to 12 N of force required to break the bonding.

Breaking the bond by this method required forces ranging from 1 to 12 N, or 2.9 to 34.81 psi. This showed the potential for a very strong bond, but the clear lack of clustering in the breaking force data in figure 3.18 indicates that the process requires further refinement for reliability and reproducibility. About 1 out of every 4 samples debonded without giving a

reading on the force table. This method was not considered further and was not included in the figure 3.18 above.

### 3.6.3: Clamped Nylon Bonding

The most effective and most consistent bond has been through ‘clamping.’ This method appears to be governed by self-assembly, i.e. it utilizes the energy minimization principle. Before polymerization, nylon forms an ionic salt. The formation of a crystalline salt is an energy minimization process. It is possible that the crystals fill across the micron-level spacing between the samples.

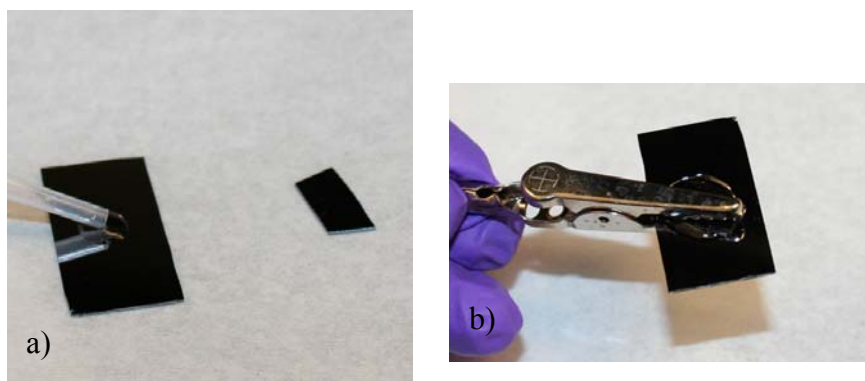


Figure 3.19: a) The solution is placed, in dilute form, onto the bottom wafer and b) the top wafer is clamped into place with an alligator clip. The solution is then allowed to dry in air to form a thin nylon salt between the layers before polymerization.

In this method, a drop of nylon 0.0295 M solution,  $\sim 0.05$  ml, was placed in its initial, dilute form onto the bottom sample by pipette. Then the top wafer was positioned in the middle of the drop and clamped into place with an alligator clip to prevent its dislocation due to internal pressure as shown in figure 3.19b. The samples were allowed to dry in air for 24 hours so that a crystalline lattice forms before polymerization. The crystalline pattern was

observed on a bottom wafer, where the solution was allowed to dry without a top wafer present, as seen in figure 3.29. Polymerization is induced by placement in an oven at 200°C for 30 minutes.

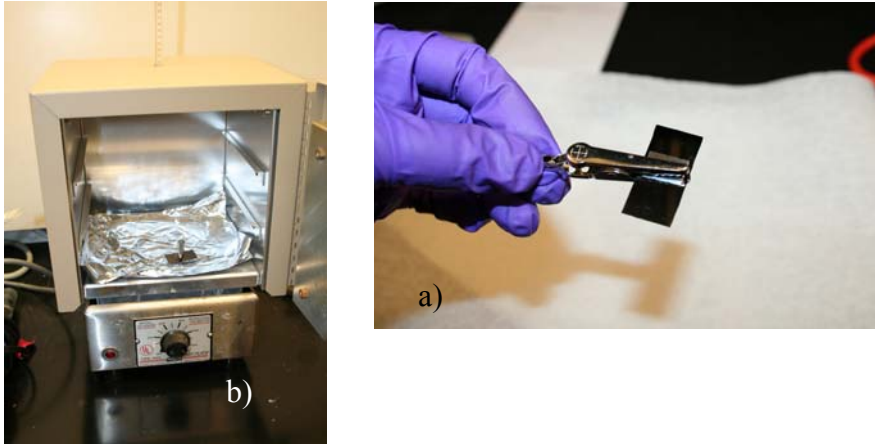


Figure 3.20: a) While clamped, the solution is allowed to evaporate overnight, so that the nylon forms a salt between the wafers. b) Then, still clamped, the nylon is heated to 200°C.

#### 3.6.3.1: Results for Bonding with Clamped Nylon

For clamped nylon, made from 0.0295 M of HMD in water and 0.0295 M of AA in ethanol, the bonding strength with most trials show definite clustering. This is evident in figure 3.21, with values of 8 to 13 N. A few, lower, outliers suggest that the reproducibility is not perfect. It is, however, superior to the other methods. In several cases, the pulling block came off before the wafers could separate, indicating a true covalent bonding.

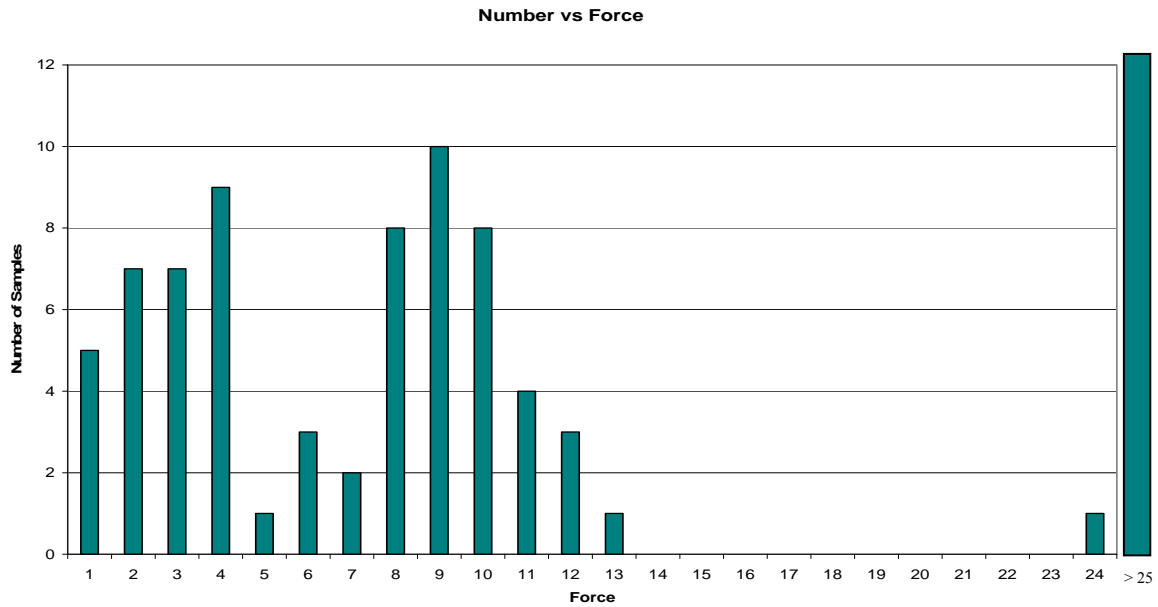


Figure 3.21: The force to break this bond was consistently higher than previous methods, centered around 4 and 9 N. This method proved more reliable and easier to fabricate. One pulling sample came off at 24 N.

Better oxidation results using the ozonator rather than the oxidizing solution gave better bonds, in later samples. In six cases, the pulling block came off before the nylon bonding broke. This means that the bond was stronger than the superglue bond that held the block onto the top sample. The force table in these cases showed a top force of 25 N, which was insufficient to break the nylon bond. Superglue was not viable as a bonding agent because it is not chemically inert, and does not have the same, ultimate bonding strength. Superglue can be removed with acetone, while the nylon nanoglue cannot.

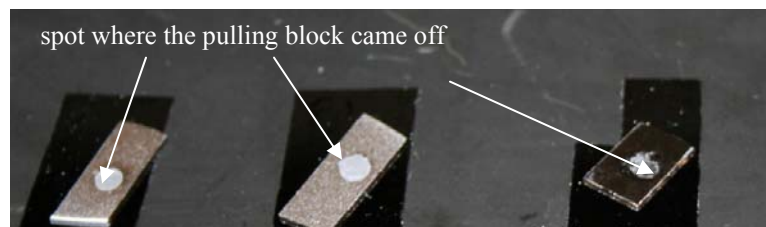


Figure 3.22: The force required to break the Si wafers apart was greater than the strength of the glue holding the pulling block on to the wafer. The cantilever sensor topped out at 24 N.

For the clamped study, some of the prepared samples were wedged apart using a single-sided razor blade as a wedge, driven by a hammer. The smaller, top wafers had a standard size, about one centimeter square. Each sample was photographed using bright field illumination (from above as usual) and dark field illumination (a flashlight was aimed from the side).

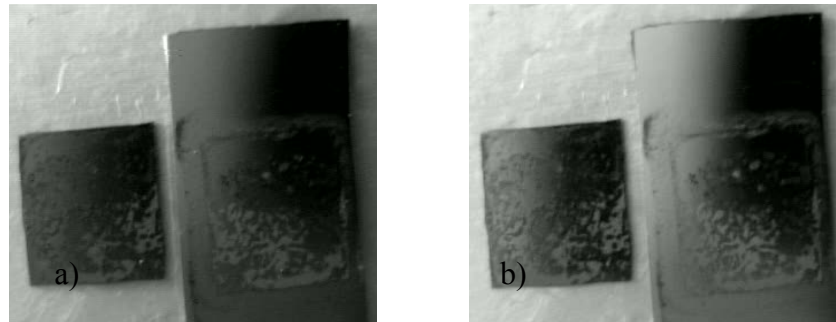


Figure 3.23: A separated sample in a) dark field and b) bright field illumination.

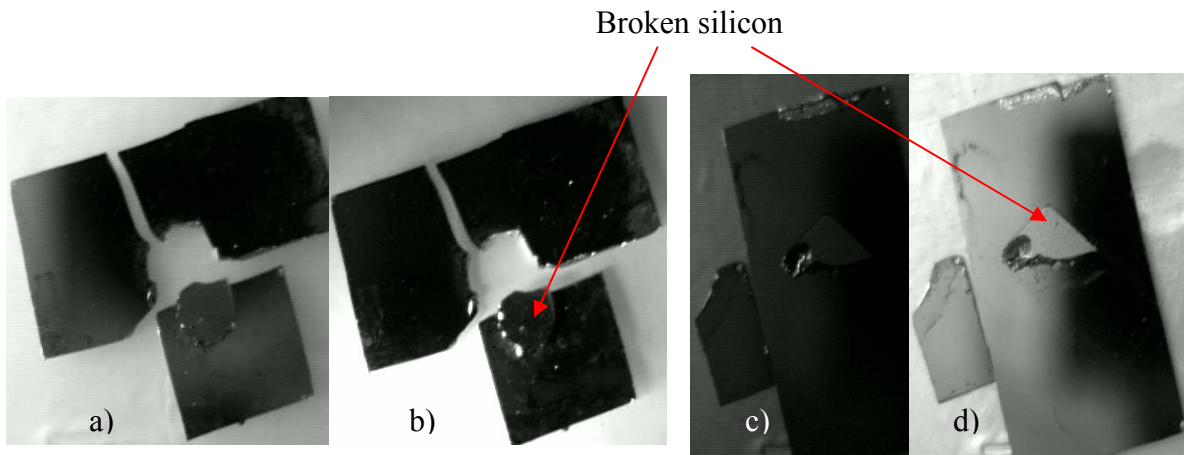


Figure 3.24: The bond was strong enough to break the silicon of the one of the wafers, leaving fragments still bonded to the opposite wafer.

Dark field illumination is standard to make topographic features more visible. This revealed the bonded areas, and allowed investigation into the nature of the bond.

About 1/4 to 1/3 had the top silicon break. The remains can be seen in the figures, where often quite a chunk of the top wafer remained bonded to the bottom wafer.

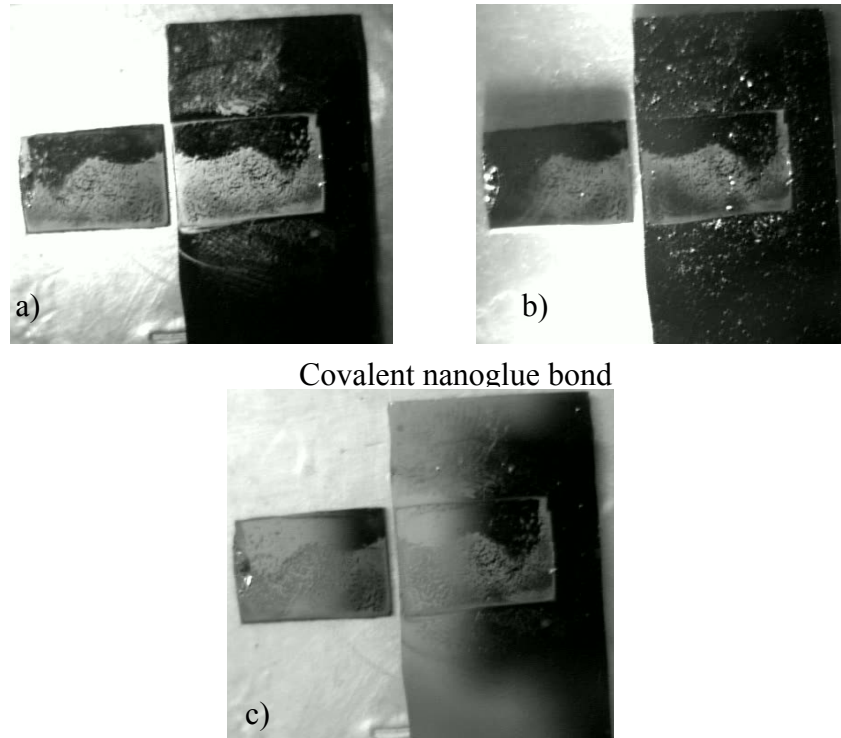
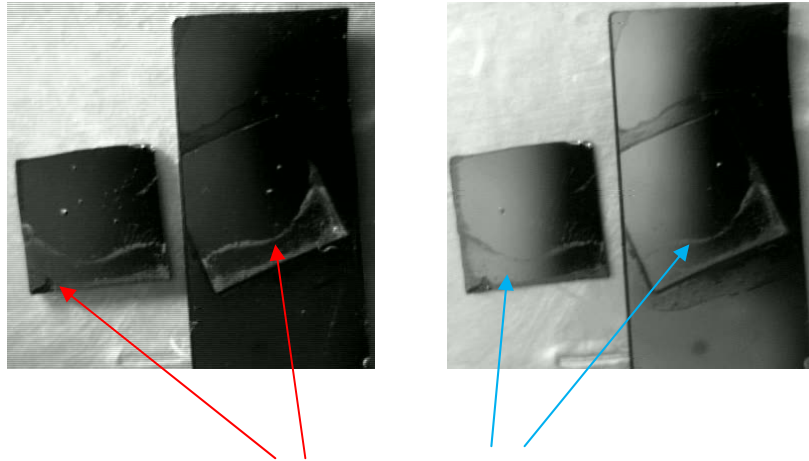


Figure 3.25: Different amounts of illumination show the depth of detail of the broken bond in the separated wafers.

None of these strongly bonded samples failed at the covalent nanoglue-silicon (or nanoglue-SAM-silicon) bond. We know this because all the figures show the same pattern on both sides, even when such a large de-bonding force was required. This strongly implies that the nanoglue is covalently bonded to the SAM and silicon, i.e. that it is a covalent nanoglue.



Identical pattern on both sides  
in dark and bright field

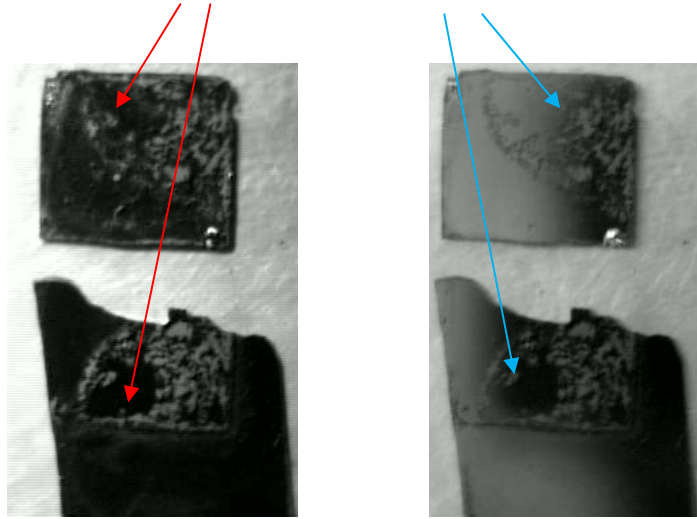


Figure 3.26: Identical patterns are a strong indicator of covalent nanogluue.

The pattern is incomplete, meaning that the bonding is not uniform, but that is simply a process optimization problem and beyond the scope of this work. The large forces needed to break the bond suggest that the material is covalently bonded from one surface to the other. This is consistent with a break in the nylon region rather than within the silicon wafers since nylon is weaker than silicon.

Data was taken of temperature stress on the bond, as the RF package can generate heat internally from general operation.

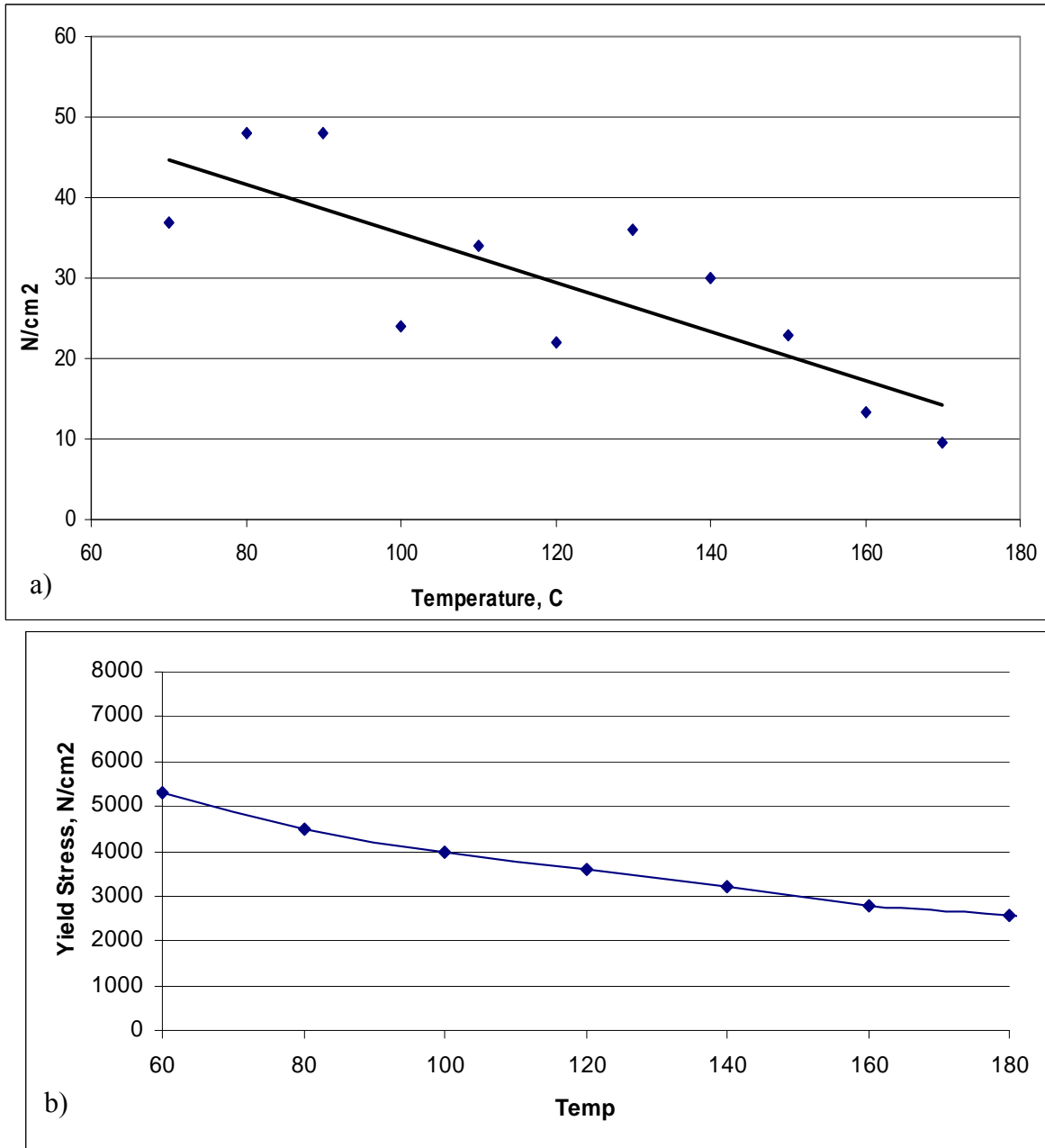


Figure 3.27: a) A temperature-dependent measurement was conducted to determine the threshold temperature for this type of bond. The bond begins to break down at around 170 deg C. b) There is a correlation between the temperature dependent strength of the bond and the yield stress studied by the Polymer Research Group. There is a downward trend in force due to a rise in temperature.

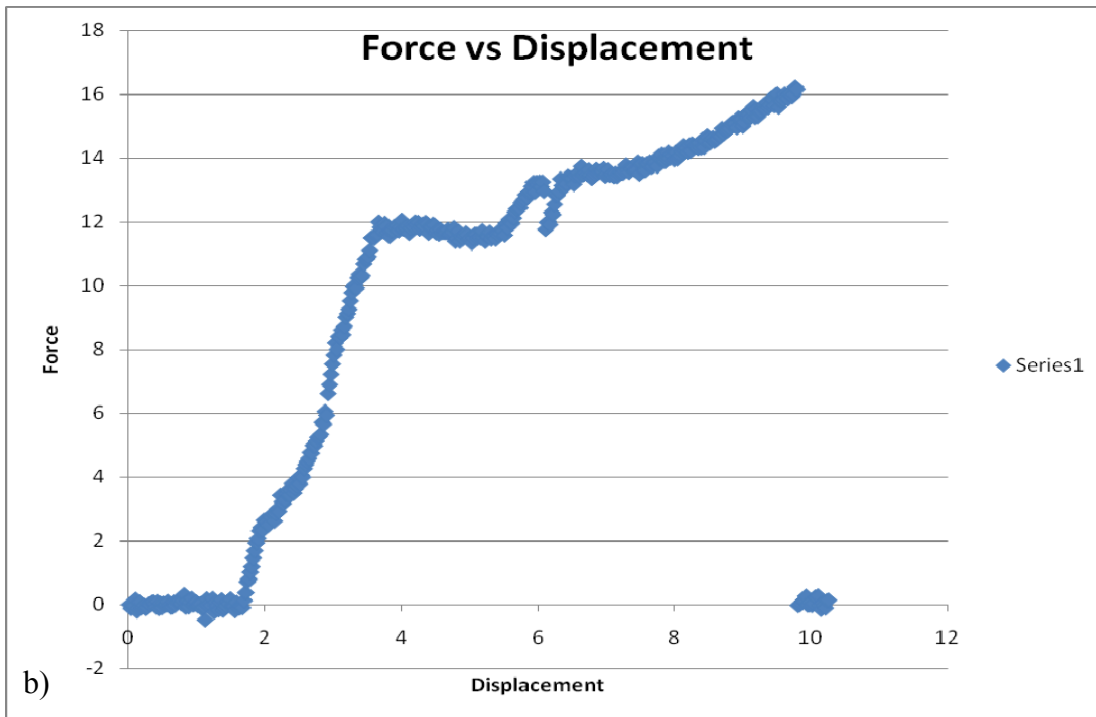
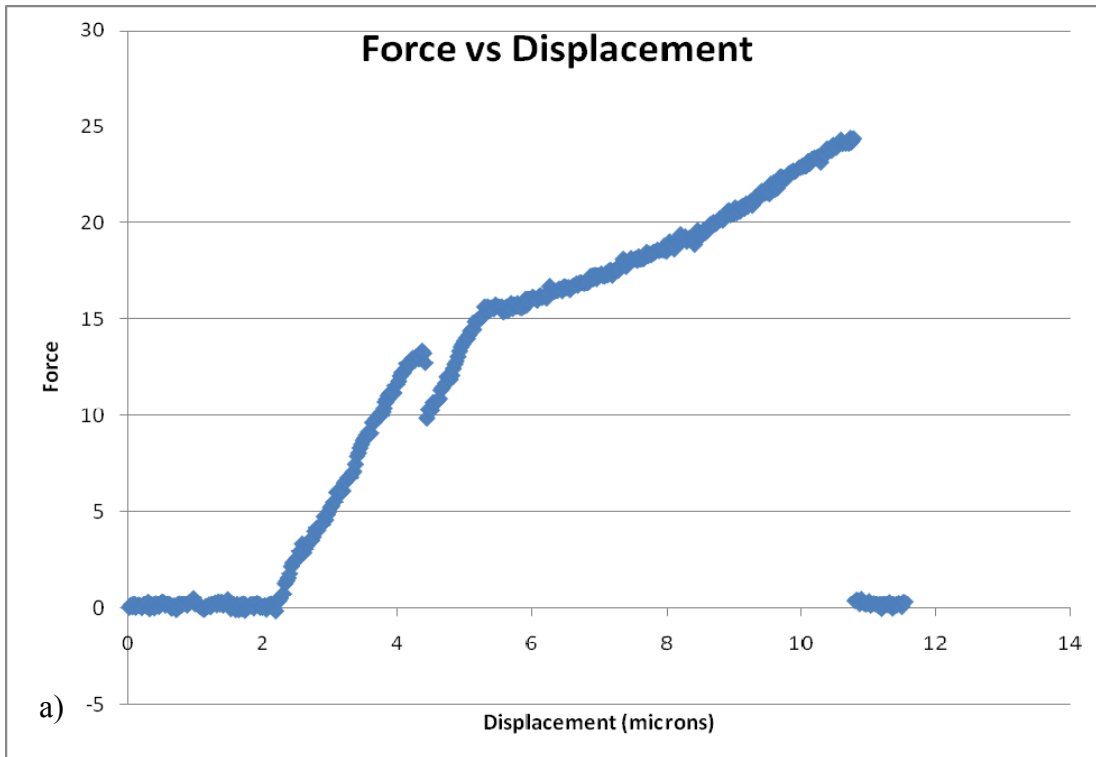


Figure 3.28: The graphs show instances where the bond did not break, but rather the pulling block, glued onto the top wafer, came off first.

#### 3.6.4: Spun-On Nylon

The last method of bonding using nylon 6,6 was spun-on nylon. To get a thinner layer and better facilitate a bond across the wafers, the nylon was spun on with the use of a spin coater. If the spinning was performed in an ambient lab environment, the layer dried out and crystallized before it adequately spreads into a thin layer. The bonding with such a layer failed. We modified the process to spin in a wet-box with relative humidity >85%. This allowed the formation of very thin layers without crystallization. The process was not completely optimized, so results were either quite poor or very good. We presumed that the process could be optimized to perform as well or better than the clamped method, but such optimization is not the aim of this dissertation. The thinner layer should allow a permanent bond that is close to the ideal 'bare' bond, while continuing to circumvent the height deficiencies of the SAMs.

Ellipsometry was used to measure the thickness of the spun on nylon. As with the clamped method, the solution was allowed to crystallize to minimize the free energy of the system. This bond was achieved only in an environment of 80% humidity, which allowed the spun-on solution to remain wet long enough for the wafers to be placed together before crystallization.

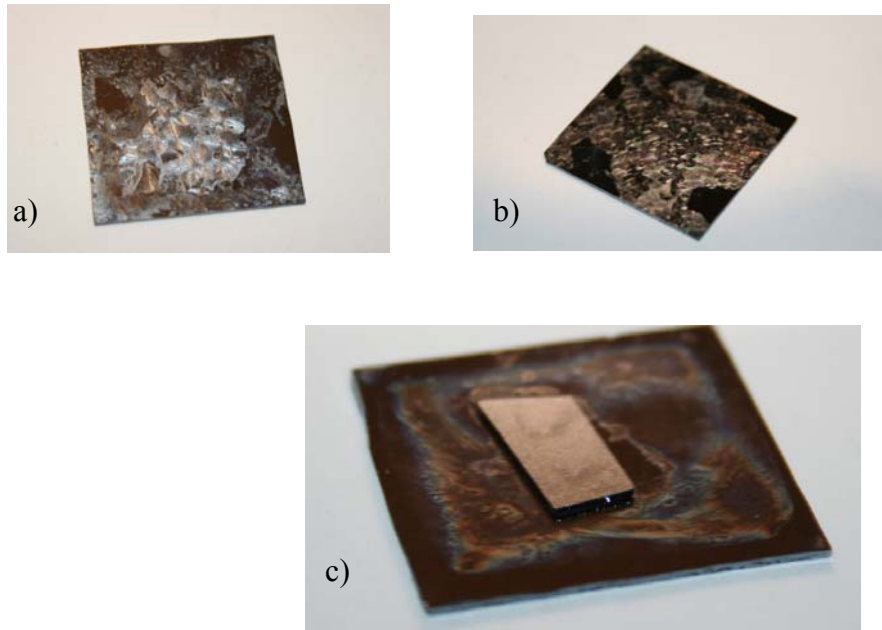


Figure 3.29: Spun-on nylon gave as good a bond as clamped nylon, while yielding the thinnest layer. The top pictures, a) and b) show the actual crystallization of the nylon salt, and the bottom image c) shows a rainbow pattern where the salt has polymerized to a nylon layer.

#### 3.6.4.1: Results for Bonding with Spun-on Nylon

This method gave the thinnest layer. Though not as successful as the clamped method, this method gave the best bond through short-fiber gap bridging. The visible driving off of water vapor indicated polymerization and the salt crystallization patterns disappeared. There was initially difficulty because the spinning process tended to cause drying of the thin nylon layer. Placement in a high-humidity environment solved this problem, allowing the spun-on layer to stay wet long enough for placement of the top wafer before the solution dried to a crystalline lattice. The samples bonded with this method required forces between 1.5 to 9.6 N to break the bonding, or 4.31 to 27.85 psi

Of the initial fourteen pulled samples, nine gave appreciable measurements, while the other five came off without giving a reading on the force table. Later results showed a bond between 1 and 10 N. In two cases, the pulling block came off before the wafers could break apart. There is a trend toward thicker values for higher concentrations, even though the distribution is wide. Presumably this wide variance is due to the drying out and crystallization process.

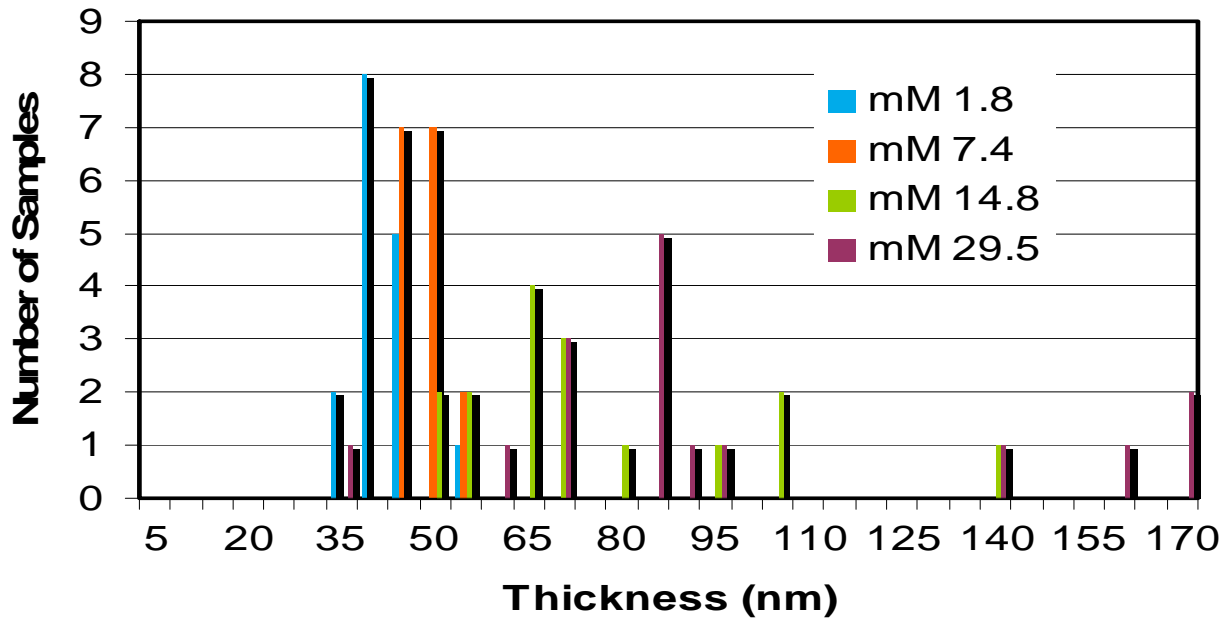
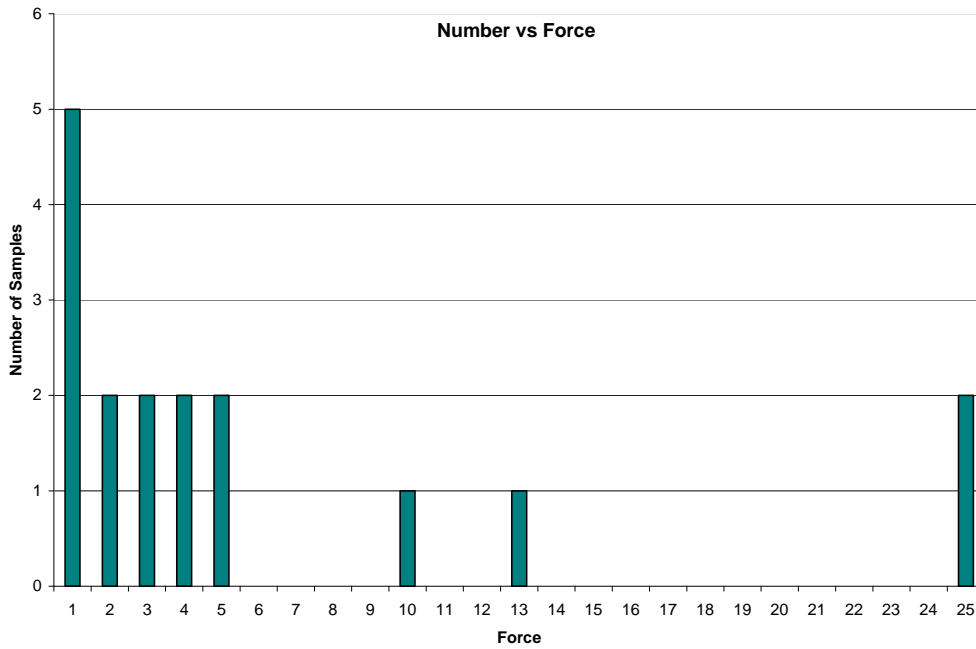
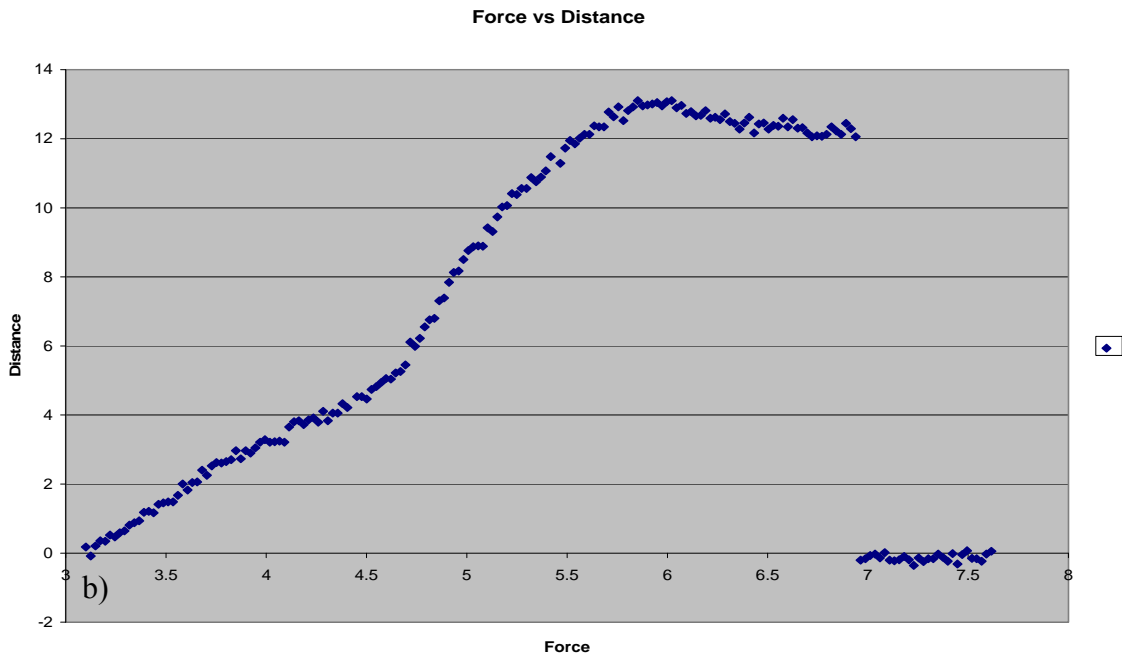


Figure 3.30: The thicknesses of the spun on nylon, measured with an ellipsometer, at different concentrations. Very thin layers of nylon were achieved, particularly with lower concentrations, but the lowest did not give a good bond.



a)



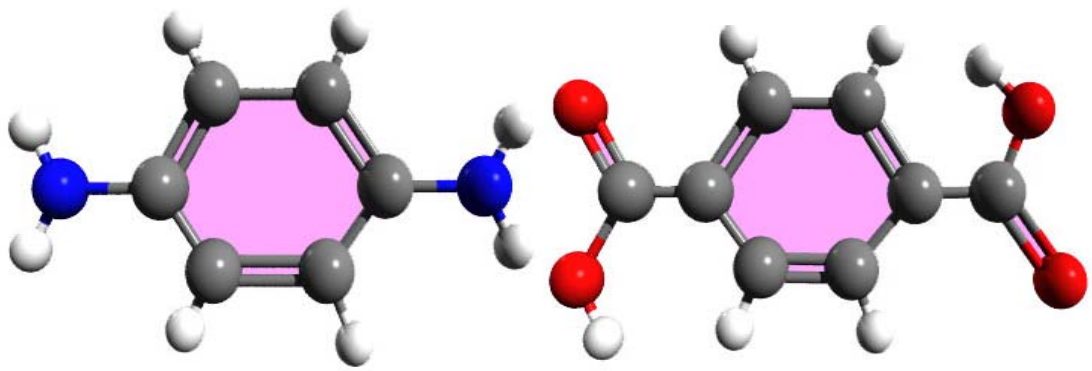
b)

Figure 3.31: a) Spun-on nylon was not as successful as clamped nylon, giving pulling forces mostly between 2 and 5 N. b) In one instance the pulling block came off, at 13 N, as shown below, but this does not give a definitive measure of comparable strength to dropped nylon.

### 3.6.5: Bonding Intermediary - Kevlar

Bonding involving the use of Kevlar, with different monomers, was studied. Kevlar is an extremely strong polymer, stiffer than regular nylon. There are also stronger inter-chain bonds in Kevlar that are more ordered than the inter-chain bonds in nylon, adding to the rigidity of the structure. These properties were thought to be a benefit and were tested as bonding agents between the SAMs of the RF package model.

Kevlar is an aromatic nylon composed of para-phenylene diamine and terephthalic acid. Terephthaloyl chloride is also used with para-phenylenediamine to make Kevlar.



Para-Phenylene Diamine

Terephthalic Acid

Figure 3.32: These molecules are the monomer constituents of Kevlar. The end functional groups are the same as nylon monomers, and the intervening structure is a benzene ring. The ring changes the properties of the monomers from those of regular nylon, making Kevlar more difficult to use.

Because of the benzene rings, Kevlar is stiffer than nylon 6,6 or nylon 6. Fibers of Kevlar consist of long molecular chains of poly(paraphenylene terephthalamide). There are inter-chain bonds that made Kevlar extremely strong. Longer fibers can also be grown due to this property.

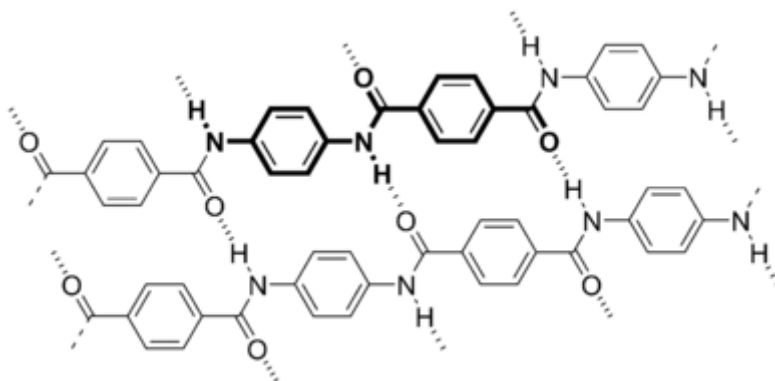


Figure 3.33: Kevlar forms rigid sheets through a form of hydrogen bonding between the long chains. Chemical Structure of Kevlar. *Cacycle, 2005*

The difficulty with producing Kevlar is finding a solvent that will dissolve the phthalic acid that is not overly toxic. In the past, hexamethylphosphoramide (HMPA) was used, but was found to be too toxic. Currently in industry, *n*-methyl-pyrrolidone and calcium chloride are used. This is because of the benzene ring, which makes terephthalic acid insoluble in water and alcohol at low temperatures. However, it is partially soluble in concentrated sulfuric acid, and can come out of solution without being altered by the sulfuric acid when water is added. Acids, even very strong ones, are generally compatible with SAMs, while strong bases are not.

To synthesize the Kevlar salt, a 0.2 molar solution was made of each monomer. Para-Phenylenediamine is soluble in water and has a molecular weight of 108.1 g/mol. To make the solution, 2.162 grams were added to 100 mL of water and heated to 130° C. Terephthalic acid has a molecular weight of 166.14 g/mol. To make the solution, 3.3228 grams were added to 5 mL of sulfuric acid, and then 95 mL of water was added.

The result was a colloidal suspension of partially dissolved particles.



Figure 3.34: Terephthalic acid will partially dissolve in sulfuric acid.

When mixed, a Kevlar salt forms in suspension. This salt is insoluble in water. The Kevlar was used as a bonding agent for holding the SAMs together. The Kevlar samples were heated to 289° C for 30 minutes to drive off the water, though unlike nylon 6-6, Kevlar does not have a melting point. This showed another difficulty with Kevlar – there was no polymerization temperature, because the terephthalic acid sublimates at high temperatures. It is believed that to achieve a bond with Kevlar, the bonding would have to be done chemically, using stronger solvents, rather than thermally.

#### 3.6.5.1: Results for Bonding with Kevlar

When pulled, the Kevlar samples gave the following results. Out of eight samples, five gave appreciable measurements, while three came off without registering a force on the meter. This bond was not as tight or reliable as nylon 6-6, ranging from 2 to 8 N.

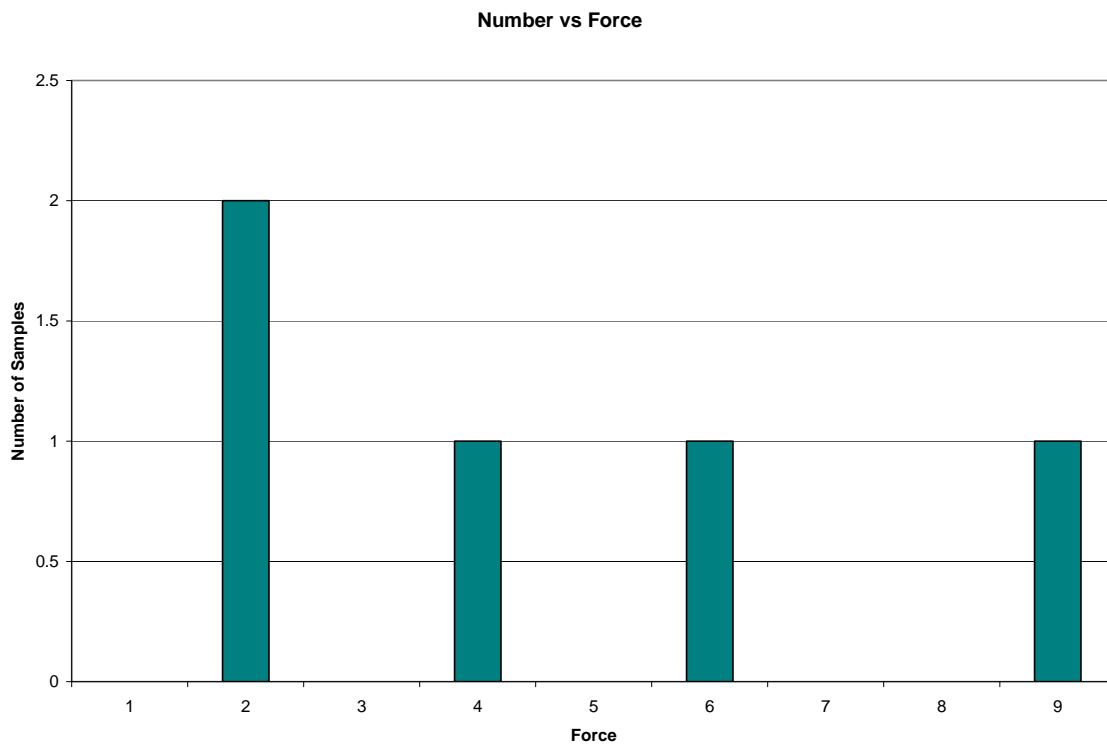


Figure 3.35: Results for Kevlar pulling. Kevlar did not give a satisfactory bond, due to the insolubility of the terephthalic acid. The solvents required were too hazardous for practical use. The bonds were not as strong as supposed, and polymerization was not assured, due to the fact that terephthalic acid sublimates at high temperatures.

Further work was not undertaken as the potential gains do not appear significant enough to find a process comparable with 1) devices on the sample, 2) the SAM layers, including both chemical and temperature limitations.

### 3.7: Conclusion

The theory of permanent bonding of silicon wafers in this study centers on covalent bonding between the long chain molecules that are adsorbed in monolayers (PEDA and 10-UTS) onto the surfaces of the silicon. The functional groups of these self-assembled monolayers (SAMs) can be made to react to form nylon, a covalently bonded polymer. The height of the SAMs, however, on the order of nanometers, requires either a very high grade of polishing on the Si surface or an intervening polymer layer.

Bonding without an intermediary, or 'bare' bonding, was strong enough to break sections of silicon from the wafer. But this type of bond, while ideal, could not be produced with consistency or with any ease of fabrication.

Intermediary bonding has been more successful than bare bonding. The intermediary fluid could also be used as the alignment fluid, from the previous phase of the fabrication process. Several methods were used to fabricate a bond with intermediate layers, some of which would prove as strong as the bare bond. These included nylon condensate, nylon immersion, clamped nylon, spun-on nylon, and Kevlar bonding. The most successful was clamped nylon, which gave a bond as strong as the bare bond (bonds up to 25 N and greater) and was the easiest to produce. A new oxidation method, ozonation, made these bonding procedures even more successful, and cut down on production time. Two cases, spun-on nylon and clamped nylon, share the property of allowing a crystal to form gave the best bond strength and reproducibility. Several cases were bonded strongly enough so that our measurement apparatus could not break the bond. We believe that this is due to solving the

orientation problem of the intermediate layer. Although the results did not have a high yield, we have demonstrated a proof of principle that covalent nanoglue is possible.

## CHAPTER 4: SELF-ALIGNMENT OF WAFERS

### 4.1: Introduction

Alignment between wafers is a critical aspect in the formation of the 3-D package. During this phase, micron-level precision is required in manipulation of the wafers. In previous studies of self-alignment, alignment orientation events of a millimeter-sized object have been observed. Capillary force has been shown to be a powerful alignment force on the sub-millimeter scale [Martin, 2001].

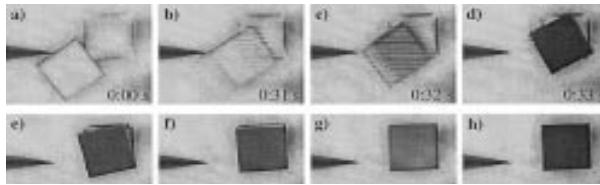


Figure 4.1: Frames of a self-assembly event. Part dimensions are 400X400X15  $\mu\text{m}$ . *U. Srinivasan, D. Liepmann, and R.T. Howe, J. Microelectromech. Sys 10 (1) 17-24(2001)*

The idea of sub-micron self-alignment between millimeter- and centimeter- scale objects is based on the concept of the minimization of the surface energy of a liquid, or capillary action due to surface tension. The surface tension is a tendency for the molecules in a liquid to move toward the center of the liquid formation, by use of intermolecular forces, in order to minimize the surface energy. Alignment on larger scales utilizing capillary force and some manual manipulation under low power microscopy has been accomplished [Byung-Ho, 2000]. Other methods of sub-millimeter self-assembly include a process that relies on gravitational and shearing forces by Smith et al., Nakakubo and Shimoyama's work using bridging flocculation and shape complementarity, and experiments by Cohen et al. employing a dry approach with electrostatic traps for self-assembly in vacuum with

ultrasonic agitation to overcome friction and adhesion [Srinivasan, 2001]. However, to achieve high assembly yield and high positioning accuracy, not only must a strong alignment force be used, but also a lubricating strategy must be employed [Srinivasan, 2001]. Experiments in dry alignment forces by Walker and the interfacial energies involved showed that the alignment based solely on these energies without the use of capillary forces would not overcome friction, as shown in figure 4.2 [Walker, 2006].

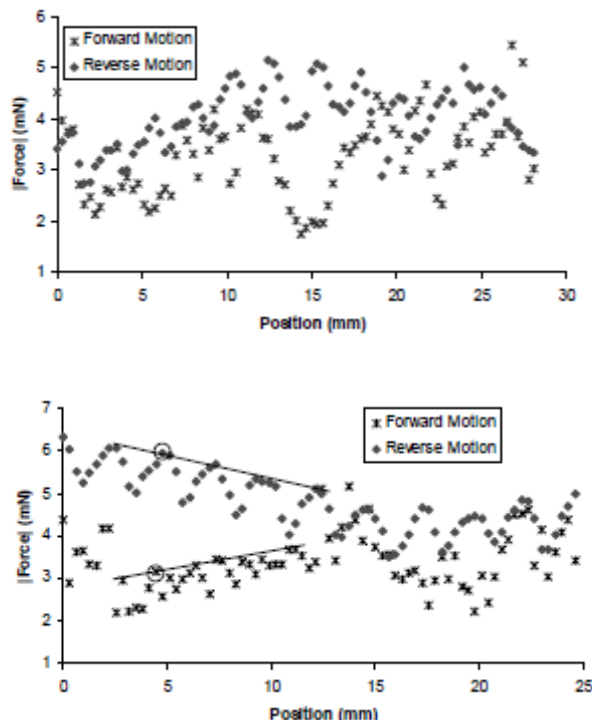


Figure 4.2: Wafer on wafer alignment, measuring static friction and the force exerted by dry hydrophilic and hydrophobic regions.

If two wafers with mirror-image hydrophilic regions are placed face to face, with liquid in between them at the hydrophilic region, then to minimize the energy of the liquid, the patterns must match with a certain precision. If the patterns are offset, the surface tension will exert a force on the top wafer to bring it back into alignment. Surface tension has been

shown to be capable of exerting strong alignment forces on the micron scale. We show the application of this ability to do work on the macroscopic scale here.

#### 4.2: Statement of the Problem

Self-alignment on the sub-micron and sub-millimeter scales, as previously stated, has been shown to be effective when capillary forces are employed. These forces, however, are proportional to the length of the solid-liquid interface, and decrease linearly with an increase in size, as stated in Srinivasan et al. With miniaturization, capillary forces become dominant; on larger scales, other forces such as pressure, which is proportional to the square of the length, and body forces, which is proportional to the length cubed, must be taken into account [Srinivasan, 2001]. Experiments in self-alignment of full wafer samples by capillary force are performed in this study to show the viability of using surface-tension based alignment in the presence of these types of forces to move wafer scale objects. Complete self-alignment without manual assistance for these larger scales through mask design is the goal of these experiments.

#### 4.3: Surface Energy

The alignment capillary forces have a free energy associated with them. This is illustrated by the tendency of the liquid surface to reach minimization when the aligned system is in a state of equilibrium, according to [Adam, 1930]. Work must be done to extend the liquid surface [Paul, 1962].

The surface contraction is caused by unbalanced intermolecular forces within the liquid, at the air-liquid interface. The molecules within the liquid exert an inward force on the molecules at the boundary, attracting them more powerfully than the dissimilar air molecules outside of the surface. The lack of balancing outside forces allows the molecules at the surface to pull together, forming a “skin” on the fluid [Paul, 1962]. Depending on the constraints, the liquid will continue to contract into a shape that allows for the minimum surface energy until the liquid’s tendency to resist compression stops the process [Paul, 1962]. The sum of the attractive forces within the liquid surface is called the surface tension.

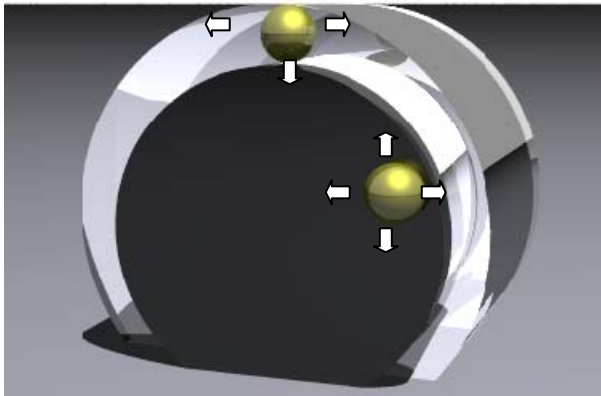


Figure 4.3: A representation of the surface tension within a water droplet on a hydrophobic surface. The molecules near the surface do not have attractive forces on the exposed side.

Sources state [Martin, 2001] that the surface tension has dimensions of force per unit length or, equivalently, energy per unit area. The quantity of mechanical work energy required per increase in the liquid surface area may be defined as:

$$\gamma \equiv \frac{\Delta E}{\Delta A}, \quad (4.1)$$

where  $\gamma$  is the surface tension,  $\Delta E$  is the change in energy, and  $\Delta A$  is the change in surface area [Paul, 1962]. In integral form, this equation can be written as:

$$E_{fluid} = \int_{\partial V} \gamma \cdot d\vec{a} \quad (4.2)$$

where  $d\vec{a}$  is the differential area of the side walls. The incremental area magnitude  $da$  is a minimum surface. This form is important for energy minimization.

First is presented an over-simplified model, where the curvature of the fluid has been idealized to a flat surface. The fluid then resembles a rectangular column between the top and bottom wafers.

At equilibrium, in the closed pattern, no fluid escapes from the pattern, and the fluid supports the weight of the top wafer. If no fluid leaves the pattern, the total volume of the fluid remains constant. The energy in the surface is represented by:

$$\Delta E = \gamma \Delta A \quad (4.3)$$

Where  $A$  is the area of the fluid surface. When the wafers are offset, there is a change in the height (a decrease) to preserve the consistency in volume.



Figure 4.4: Without the simplifying assumption that the vertical separation between the wafers is constant, the height decreases as the wafer is offset to preserve consistency in the volume of fluid.

For this pattern, where one edge of the area will remain constant, and the displacement is completely in the x-direction, the energy equation can be written as:

$$\Delta E = \gamma \Delta x \cdot l \quad (4.4)$$

The surface tension is defined as the force along a line of unit length, where the force is parallel to the surface, but perpendicular to the line. This gives a hint to the form of the force equation:

$$\frac{\Delta E}{l} = \gamma \Delta x \Rightarrow \Delta F = \gamma \Delta x \quad (4.5)$$

This is very similar to the spring restoring force

$$F = -kx \quad (4.6)$$

A theoretical model of the surface energy of the fluid in this system needs to take into account fact that the fluid is compressed between two solid surfaces, and that the upper wafer contributes to the internal pressure. The internal pressure generated by the weight of the top solid object will cause the side walls of the fluid to bulge outward, since water is nearly incompressible. The cohesion between the fluid and the two solid surface boundaries on the top and bottom also affects the shape of the fluid surfaces, and in turn, the surface energy.

The following equation relates the pressure inside and outside of the fluid compressed between two solids to the surface tension  $\gamma$ , and to the radii of curvature for a non-spherical surface [De Gennes, 2002; Martin, 2001]:

$$P_1 - P_2 = \gamma \left( \frac{1}{R_1} + \frac{1}{R_2} \right). \quad (4.7)$$

$P_1$  is the pressure inside the liquid,  $P_2$  is the pressure outside.  $R_1$  is one of the radii of the curvature of the liquid between the two wafers, and  $R_2$  is the second radius. The pressure  $P_1$  inside of the liquid is given by:

$$P_1 = P_2 + \rho g(z_1 - z_2) \quad [\text{Halliday, 1997}] \quad (4.8)$$

If  $p_2$  is the weight of the upper silicon wafer and  $z_1 = 0$  at the surface of the liquid at the interface with the solution and wafer, this equation becomes:

$$P_1 = p_{wafer} + \rho g(z_2) \quad (4.9)$$

The depth  $z_2$  will be taken to be the midpoint between the wafers. The parameter  $\rho$  is the density of the fluid, and  $g$  is the value of gravity. To support a wafer of silicon 1” square and 450 microns thick, the solution had to exert a pressure:

$$p_{wafer} = \frac{\Delta F}{\Delta A} = \frac{Weight_{wafer}}{Area_{hydrophilic}}. \quad (4.10)$$

At equilibrium, the surfaces (cross-sectionally) of the fluid take an energy minimizing shape. This shape must take into account the weight of the top wafer, which increases the internal pressure of the alignment fluid. The shape of the side-walls is determined by the cohesion of the liquid surface, the result of hydrogen bonds. This curve minimizes to a shape that must be calculated. Once the pressures are calculated, the shape of the boundary can be mapped graphically and compared to the experimental value. Once the pressure is known, a theoretical value for the surface energy can be calculated. This is left for future works.

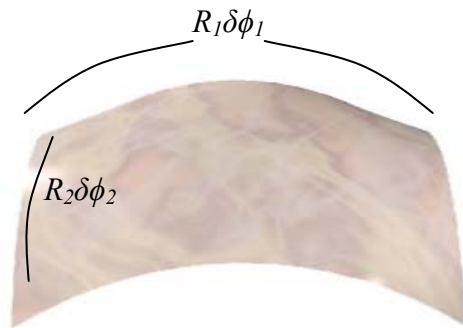


Figure 4.5: A representation of the radii of curvature of a liquid surface.

This area of the surface is some curve, to be determined, is defined by

$$\Delta A = R_1 \Delta \phi_1 R_2 \Delta \phi_2 \quad (4.11)$$

Where  $R_1$  is a function of  $\phi_1$  and  $R_2$  is a function of  $\phi_2$ . An illustration of this surface can be seen in figure 4.4. The fluid surface in our study is oriented so that  $R_1 \phi_1$  is in the  $x$ - $y$  plane, and  $R_2 \phi_2$  is in the  $x$ - $z$  plane as shown in figure 4.5. Therefore,  $R_1$  and  $\phi_1$  can be written as functions of  $x$  and  $y$ , and  $R_2$  and  $\phi_2$  can be written as functions of  $x$  and  $z$ .

$$R_1(\phi_1) \Delta \phi_1 = R_1(x, y) \Delta \phi_1(x, y) \quad (4.12)$$

$$R_2(\phi_2) \Delta \phi_2 = R_2(x, z) \Delta \phi_2(x, z) \quad (4.13)$$

Within the alignment pattern, the radius of curvature  $R_1$  that follows the edge of the pattern is modeled as a straight line, so that

$$R_1 \Delta \phi_1 = l \quad (4.14)$$

Where  $l$  is a constant with length  $\sqrt{x^2 + y^2} = y$ . If we assume that  $P_2$  is one standard atmosphere and  $R_2$  is a straight line that is much larger than  $R_1$ , the equation reduces to:

$$P_1 = \gamma \left( \frac{1}{R_1} \right) + P_{atm}. \quad (4.15)$$

Then, the relationship between the pressure and  $\gamma$  can be equated to the internal energy:

$$\Delta P * R_1 = \gamma = \frac{\Delta E}{\Delta A} \quad (4.16)$$

For the second radius of curvature,  $R_2$ , the parameter  $z$  is the separation between the wafers due to the fluid present in the alignment pattern. Assuming that the state of the fluid in the pattern is in equilibrium (no loss of fluid due to evaporation or drainage), the parameter  $z$  is

constant, so that changes in  $R_2$  and  $\Delta\phi_2$  depend only on changes in  $x$ . The surface tension equation can then be written in the following manner

$$\frac{\Delta E}{\Delta A} = \gamma = \frac{\Delta E}{yR_2(x)\Delta\phi_2(x)} \quad (4.17)$$

From this, the alignment force, which would result from the minimization of this energy, may be found by dividing out the length of the side that remains constant from both sides

$$F = \frac{\Delta E}{y} = -\gamma \left[ \frac{\Delta E}{R_2(x)\phi_2(x)} \right] \quad (4.18)$$

With a known shape for  $R_2\phi_2$ , before misalignment and at extreme misalignment (just before the surface breaks and reforms at another point on the alignment pattern) the initial and final energies can be calculated, and may be pursued in a later work. This also assumes a known surface tension,  $\gamma$ . The surface tension for DI water is known, but when concentrations of ethanol are added,  $\gamma$  changes. These values of  $\gamma$  can be found by contact angle.

Following, the area of the fluid surface is modeled using the calculus of variations, which is a tool for minimizing functions.

#### 4.4: Energy Minimization

The aligning force would be a result of the tendency for the fluid surface to minimize its energy in the exposed capillary walls. The minimized quantity of boundary molecules results in a minimized surface area. The mechanical work needed to increase a surface is  $dE = \gamma dA$ . Hence, at constant temperature and pressure, surface tension equals Gibbs free energy per unit surface area [De Gennes, 2002]:

$$\gamma = \left( \frac{\partial G}{\partial A} \right)_{T,P,n} = \frac{\partial E}{\partial A} \quad (4.19)$$

Where  $G$  is Gibbs free energy. The internal energy of the system is characterized by the surface energy of the fluid, which can be described by the integral form of the above equation:

$$E_{fluid} = \int_{\partial V} \gamma \cdot d\vec{a} \quad (4.20)$$

where  $\gamma$  is the surface tension, and  $d\vec{a}$  is the differential area of the side walls. The problem is to find the curve that describes the cross-section of the area of the water surface. The area of a strip of this surface is  $lds$ , where  $ds$  is given by:

$$ds = \sqrt{dr^2 + r^2 d\phi^2}, \text{ or } ds = \sqrt{1 + r^2 \phi'^2} dr; \quad (4.21)$$

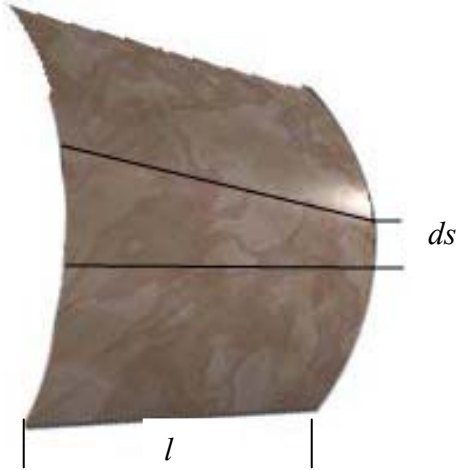


Figure 4.6: A graphical representation of the surface of the alignment fluid between the top and bottom alignment wafers. The straight edge  $l$  is in the  $y$ -direction, and the differential segment  $ds$  is in the  $x$ - $z$  plane.

$$da = l \times ds = l \sqrt{r^2 d\phi^2 + dr^2} \quad (4.22)$$

When the energy is at a minimum, the surface is also at a minimum.

$$E_{\min} = \int \gamma \cdot l dr \sqrt{r^2 \frac{d\phi^2}{dr^2} + 1} \quad (4.23)$$

Using the minimization method as spelled out in Goldstein,

$$I = \int_1^2 ds = \int_1^2 dr \sqrt{1 + r^2 \left( \frac{d\phi}{dr} \right)^2} \quad (4.24)$$

“The condition that the curve be the shortest path is that  $I$  be a minimum.” [Goldstein, 1980]

Let the integrand of  $I$  be defined as  $f$ :

$$f = \sqrt{1 + r^2 \phi'^2} \quad (4.28)$$

From the calculus of variations, the minimization of  $f$  is:

$$\frac{\partial f}{\partial \phi} - \frac{d}{dr} \left( \frac{\partial f}{\partial \phi'} \right) = 0 \quad (4.29)$$

For our calculation:

$$\frac{\partial f}{\partial \phi} = 0, \text{ and } \frac{\partial f}{\partial \phi'} = - \frac{r^2 \phi'}{\sqrt{1 + r^2 \phi'^2}} \quad (4.30)$$

The calculus of variations demands that:

$$\frac{d}{dr} \left( \frac{r^2 \phi'}{\sqrt{1 + r^2 \phi'^2}} \right) = 0 \quad (4.31)$$

For this to be an extremum, the following must be true:

$$\frac{r^2 \phi'}{\sqrt{1 + r^2 \phi'^2}} = a \quad (4.32)$$

where  $a$  is a constant of integration. Squaring both sides and factoring terms:

$$r^2 \phi'^2 (r^2 - a^2) = a^2 \quad (4.33)$$

Once the terms have been separated, the equation can be solved by integrating both sides,

$$d\phi = \frac{a}{r\sqrt{r^2 - a^2}} dr \quad (4.34)$$

$$\phi = a \int \frac{1}{r\sqrt{r^2 - a^2}} + b = \frac{a}{|a|} \sec^{-1} \frac{r}{a} + b \quad (4.35)$$

$$r = a \sec(\phi - b). \quad (4.36)$$

This is the relationship between the radius and the angle of the minimum curvature of the surface, where  $r = R_2$ . The actual shape of the surface,  $s$ , is given by:

$$s = r\phi = \phi \cdot |a \sec(\phi - b)| \quad (4.37)$$

The absolute value is required because the surface is the total displacement. This reduction of the surface to a minimum shape is the mechanism of alignment. Let  $a = l$  and  $b = \pi$ . The shape of the water surface in cross-sectional view is graphed below. There are boundary conditions at the point of contact between the water and the wafer, the same boundary conditions that give the parameters for the contact angle. This boundary condition is at the edge of the two different materials and it is unclear what the boundary condition will do, but the transition region will be very small.

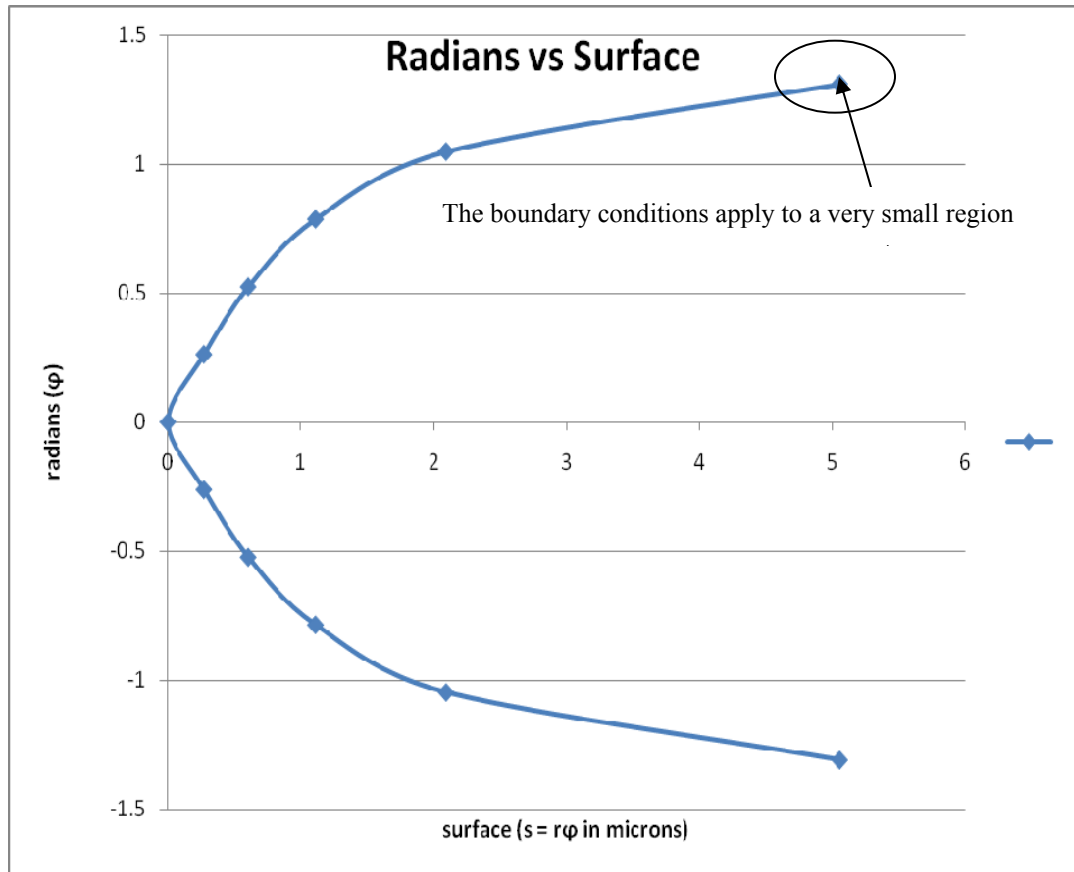


Figure 4.7: Calculated shape of the water surface according to the energy minimization process.

To find the force,  $R_2$  and  $\phi_2$  must be written in terms of  $x$  and  $z$ :

$$R_2 = -\sec(\phi - \pi) = \sec(\phi) = \frac{\sqrt{x^2 + z^2}}{x} \quad (4.38)$$

$$\phi = \arctan \frac{z}{x} \quad (4.39)$$

The force can then be derived from equation 4.5:

$$F = \frac{E}{l} = \gamma \phi \sec \phi \quad (4.40)$$

$$F = \gamma \arctan\left(\frac{z}{x}\right) \frac{\sqrt{x^2 + z^2}}{x} \quad (4.41)$$

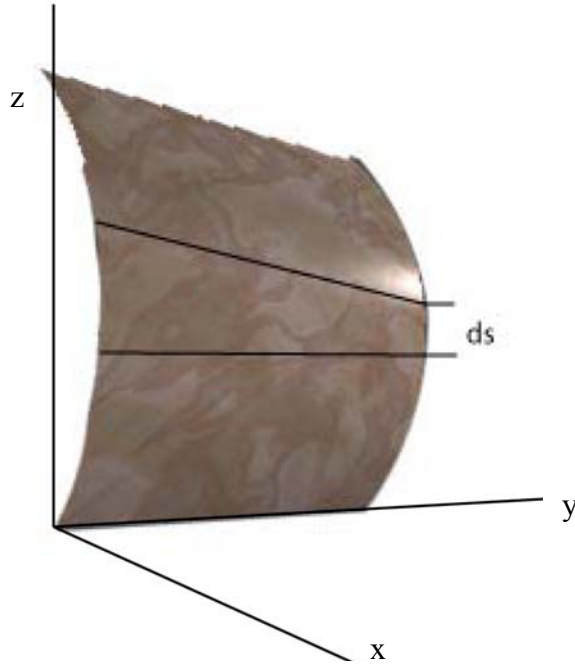


Figure 4.8: The coordinate system is oriented so that the wafer offset force can be shown completely in the x direction.

This calculated force is exerted by the surface of an individual fluid segment. The above force dissolves the stable alignment case. The length  $y$  depends on the length of the segment of the pattern being calculated. For the total force, all the contributions of the pattern must be added:

$$F_{total} = \sum_{segments} \gamma \tan^{-1}\left(\frac{z}{x}\right) \frac{\sqrt{x^2 + z^2}}{x} \quad (4.42)$$

Each side wall of the pattern that has a component perpendicular to the direction of motion of misalignment contributes to the alignment force. When the wafers are first pushed out of alignment, the exposed sides of the fluid are stretched water surfaces in air. These stretched

surfaces may slump over onto the hydrophobic regions, increasing the surface energy. The surface tension of a liquid on a solid surface is well documented, and can be found by calculation using contact angles.

#### 4.5: Change in Area

When the pattern is off-set from equilibrium, the surface area of the fluid increases. In this off-equilibrium situation, the cohesion between the fluid molecules resists the movement of the interior molecules to the surface. This same force causes wafers not originally aligned to come into alignment. The more complex the pattern, the more surface area is available to exert force on the top wafer. This means less curvature on each segment or that the linear model described before becomes more accurate. Because a parallelogram has the same surface area as a rectangle of the same height and base, only the surfaces that are at an angle to the vertical actually change in area and exert force on the wafer.

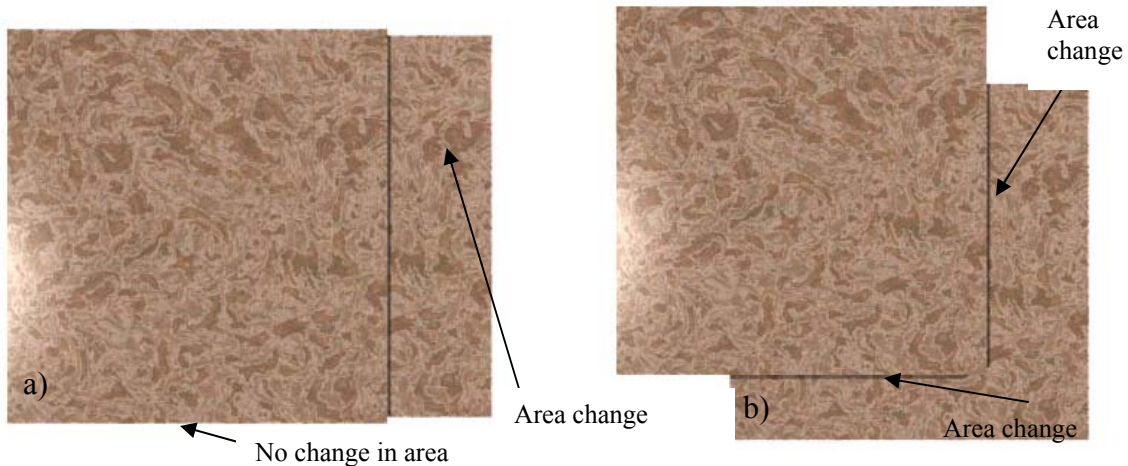


Figure 4.9: An illustration of wafers being pushed out of alignment. a) Only the water surfaces that make an angle to the vertical contribute to the alignment force. b) Both horizontal and vertical displacement, but edges parallel to the motion do not contribute.

Because the water surface is curved, due to imbalances in the internal and external pressures, the surface deforms as the horizontal force is applied to the top wafer, but it is postulated that the area, and thus the energy, changes at a slower rate until the surface has reached a flattened-out limit. The surfaces that are changing in area cannot flatten out and still support the upper wafer, so the surfaces parallel to the motion of the top wafer support it. Given that the surface is on the order of microns along the periphery, this limit should be reached within a few microns of movement. Once the surface flattens out, the area begins to change, as does the energy, since it is directly proportional to the area. All the segments of the pattern that are parallel to the motion of the top wafer theoretically do not contribute to the restoring force. These segments support the upper wafer. With small displacements, it is assumed that there is negligible change in height of the upper wafer position, and therefore no change in the area of these parallel segments. This assumption may not hold for larger displacements.

Assuming a constant separation between the wafers, the change in area of the surfaces when there is only displacement in the  $x$ -direction, can be calculated as follows. Only surfaces that leave the vertical experience a change in area.

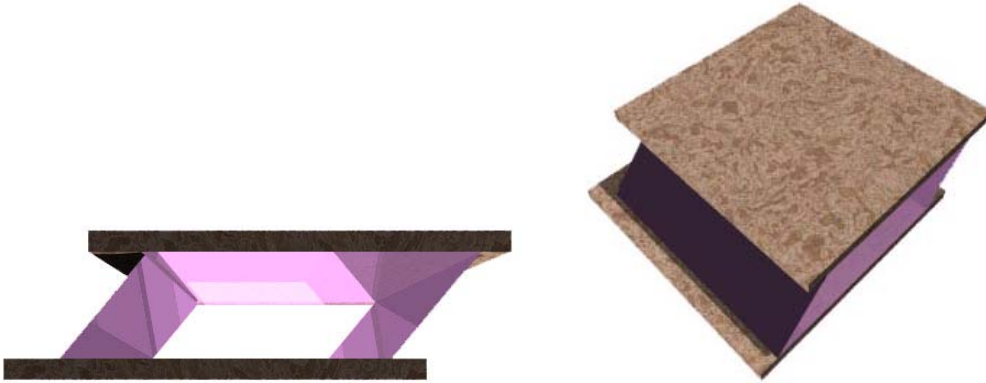


Figure 4.10: The water surface, once it reaches the “elastic” extent of the curved surface, begins to flatten out and the area of the surface begins to increase, thereby increasing the surface energy.

Segments of the pattern that leave the vertical contribute to the restoring force. To find the change in area, certain parameters need to be known. These include the height of the water column, the length of the segment, the displacement of the top edge of the water column, and the angle that the between the side and bottom edges of the water. Given the height  $z$ , the displacement  $x$ , and length  $l$ ,

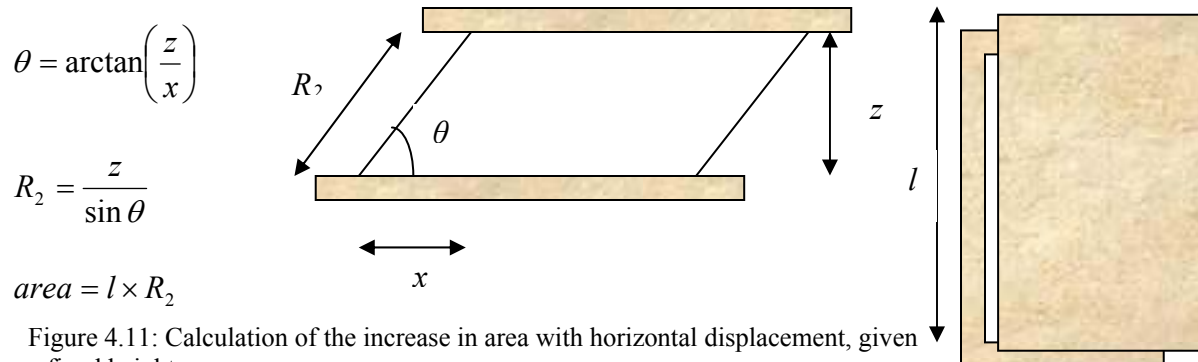


Figure 4.11: Calculation of the increase in area with horizontal displacement, given a fixed height.

The orientation of the pattern to the applied force impacts the displacement of the surfaces from the vertical. If the vector of the applied force is set as the normal to a standard line, then the orientation of the pattern with relation to that line gives the angle from which there is relative displacement from the vertical, and thus the area change can be calculated.

Assuming no compression of the fluid (all of the motion is parallel to the ground plane), then the fluid surface makes an angle  $\theta$  with the displacement vector  $x$ . The new area, calculated from the length times the radius of curvature, of the surface is given by:

$$Area = l \times \frac{z}{\sin \theta} = yR_2 \quad (4.43)$$

Where  $R_2$  is a function of  $x$  and  $z$ , as previously stated. As the wafer is pushed out of alignment, the radius  $R_2$  changes. Assuming that the  $z$ -component of  $R_{2z}$  remains constant, as  $R_{2x}$  changes, then  $\theta$  changes and  $R_2$  increases.



Figure 4.12: Assuming that the vertical separation between the wafers is constant, as the horizontal component changes, the area increases.

If  $R_{2z}$  is known, then  $\theta$  can be found by measuring the  $R_{2x}$  displacement.

$$\tan \theta = \frac{R_{2z}}{R_{2x}} = \frac{z}{x} \quad (4.44)$$

$R_2$  can be found by a simple trigonometric relation.

$$R_{2x} = R_2 \cos \theta \quad (4.45)$$

When the top wafer is displaced in both  $x$  and  $y$ , the displacement of the water surface from the vertical may be more easily described in polar space coordinates. In this case, the radius of curvature is equivalent to the radius in the coordinate system.

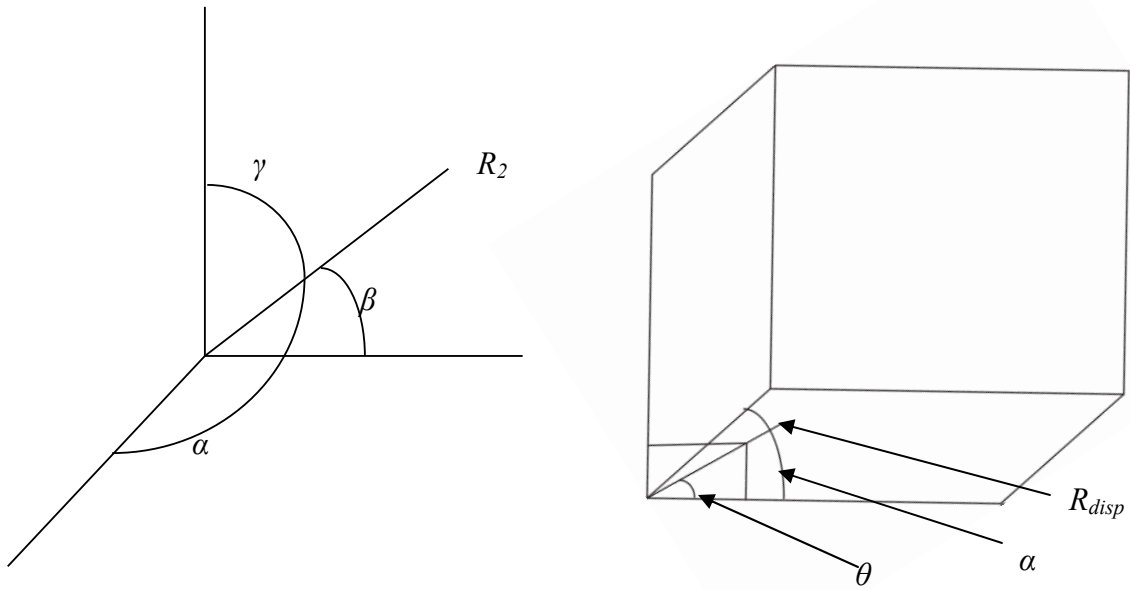


Figure 4.13: Polar space coordinates are convenient to describe the fluid edge as it is displaced in  $x$  and  $y$ . The displacement of the wafer due to the force table is  $R_{disp}$ .

The area of each water plane is represented by the equation for the area of a parallelogram, base times height. But there are more surfaces leaving the vertical, though not to the same extreme in either axis.  $R_2$  is related to  $x$  and  $y$  by:

$$x = R_2 \cos \alpha \quad (4.46)$$

$$y = R_2 \cos \beta \quad (4.47)$$

The segment  $R_{disp}$ , is the total displacement of the wafer by the force table. This quantity can be related to  $R_2$  by the  $x$  component:

$$x = R_2 \cos \alpha \text{ and } x = R_{disp} \cos \theta_0 \quad (4.48)$$

$$R_2 = \frac{R_{disp} \cos \theta_0}{\cos \alpha}$$

$$\text{where } \alpha = \cos^{-1} \left[ \frac{x}{\sqrt{x^2 + y^2 + z^2}} \right] \text{ and } \theta_0 = 45^\circ \quad (4.49)$$

For the same alignment pattern pushed out of alignment at different orientations (corner to corner misalignment as opposed to edge to edge misalignment) it is postulated that the alignment force is corrected (or modified) only by the new angles with respect to the motions, no matter the orientation. The segments of the pattern in which the water surface makes some angle to the vertical along the x and y axes will do so more slowly than if all the motion were along only the x axis. In other words,  $R_2 = \frac{x}{\cos \alpha}$  changes more slowly than

$R_2 = \frac{x}{\cos \theta}$  as shown in figure 4.13.

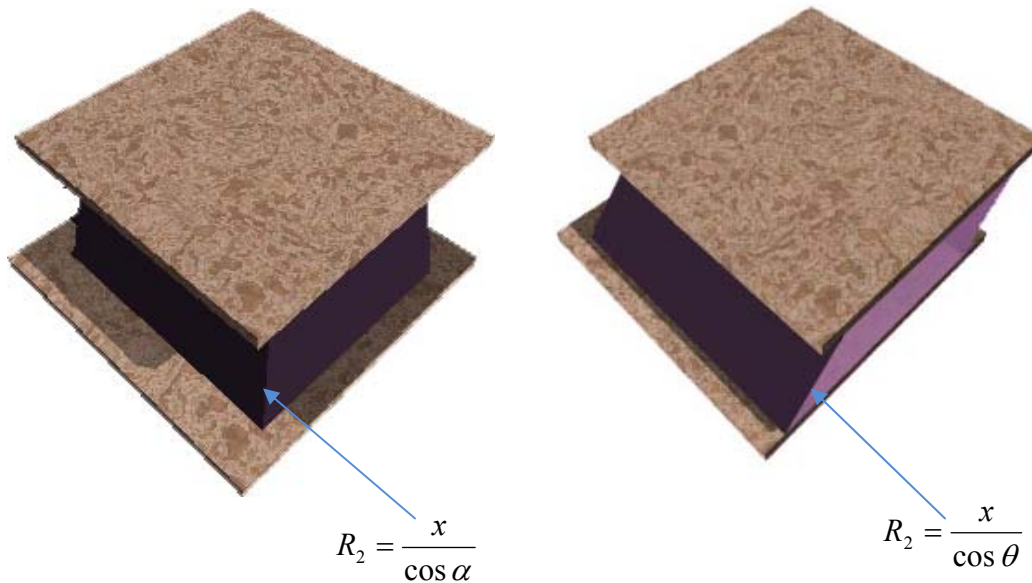


Figure 4.14: A comparison of the displacement of the water edge in x to the displacement in x and y.

The constant length  $l$  can no longer be assumed to be just in the y direction; there will be a constant length  $l_y$  for the surface with its length in the y-direction, and a constant length

$l_x$  for the surface with its length in the  $x$ -direction. The pattern is set up so that most of the surfaces that have lengths with components in both the  $x$  and the  $y$  direction will change in  $x$  and  $y$  in equal amounts (the constant lengths of the surfaces are at  $45^\circ$  to the edge of the wafer). A practical illustration of this will be given in the following chapter.

#### 4.6: Contact Angle Model and Data

The contact angle of a liquid on a solid surface is one of the most effective ways of measuring the surface energy of the fluid. For a hydrophilic surface, such as clean silicon, deionized water has a contact angle of  $33^\circ$ - $35^\circ$  [Wasserman, 1989].

In previous work, it was shown that the interfacial energies of the boundaries of a liquid, a vapor and a solid surface were given by:

$$\gamma_{SL} + \gamma_{LV} \cos \theta - \gamma_{SV} = 0 \text{ [Ulman, 1991]} \quad (4.50)$$

A mixture of water and ethanol had a profound effect on the interfacial energy of the liquid boundary. Because ethanol was less cohesive than water, the mixture has a lower surface energy than water, but higher than unadulterated ethanol. Therefore, the contact angle decreased as more ethanol was added to the mixture, because there was more adhesion to the solid surface as opposed to cohesion within the liquid. A rough predictive model can be built from the Good-Girifalco-Fowkes equation [Walker, 2006]:

$$\cos \theta = -1 + 2 \sqrt{\frac{\gamma_{SV}}{\gamma_{LV}}} \quad (4.51)$$

The  $\gamma_{LV}$  for deionized water was given in [Chaudhury, 1991] as  $\gamma_{H_2O} = 72.94$  mN/m and the contact angle is  $\theta = 55.6^\circ$  for a silicon sample with PEDA adsorbed onto the surface. This

gives a solid surface energy of 44.6 mN/m for PEDA. The surface energy of the aqueous ethanol mixture as measured in [Vazquez, 1995] was as shown in

Table 4.1: Table 4.1: Measured values of the surface tension, based on concentration of ethanol to water [Vazquez, 1995].

Surface Tension of Ethanol + Water	
$\gamma/(\text{mN/m})$ at 20°C	
mass %	surface tension $\gamma$
0	72.75
10	47.53
20	37.97
30	32.98
40	30.16
50	27.96
60	26.23

These values were based on percentage by mass, which differs from percentage by volume, because the density relationship of the solution as the percentage changes is nonlinear. In other words, because ethanol is less dense than water, at higher concentrations of ethanol, the overall solution will be less dense. However, the values can give a ball-park figure for where the surface tension graphs should plateau. The predicted values calculated are listed below:

$$\gamma_{LV} = \gamma_{SV} \left[ \frac{2}{\cos \theta + 1} \right]^2 \quad (4.52)$$

Table 4.2: Calculation of the surface tension based on contact angle, and concentrations of ethanol in water.

Aqueous Ethanol					
Concentration %	Contact Angle	Surface Tension mN/m	Concentration %	Contact Angle	Surface Tension mN/m
0	55.4467	72.638	0	56.14	73.574
10	52.5	68.931	10	50	66.105
20	45	61.217	20	37.885	55.726
30	36.69	54.947	30	32.653	52.582
40	29.85	51.163	40	27.47	50.088
50	27.3167	50.023	50	20.075	47.438
60	23.213	48.442	60	15.568	46.282

The contact angles were taken for dilutions of aqueous ethanol ranging from 0% to 60% by volume. The contact angles and the associated surface tensions were as shown in Table 4.2. There was not good agreement between the experimental values by mass, and those calculated by volume. The calculated values were higher by more than 20mN/m for the first set of data, and more than 19 mN/m for the second set of data. There was more than likely a propagation of error from the measured valued for the contact angle.

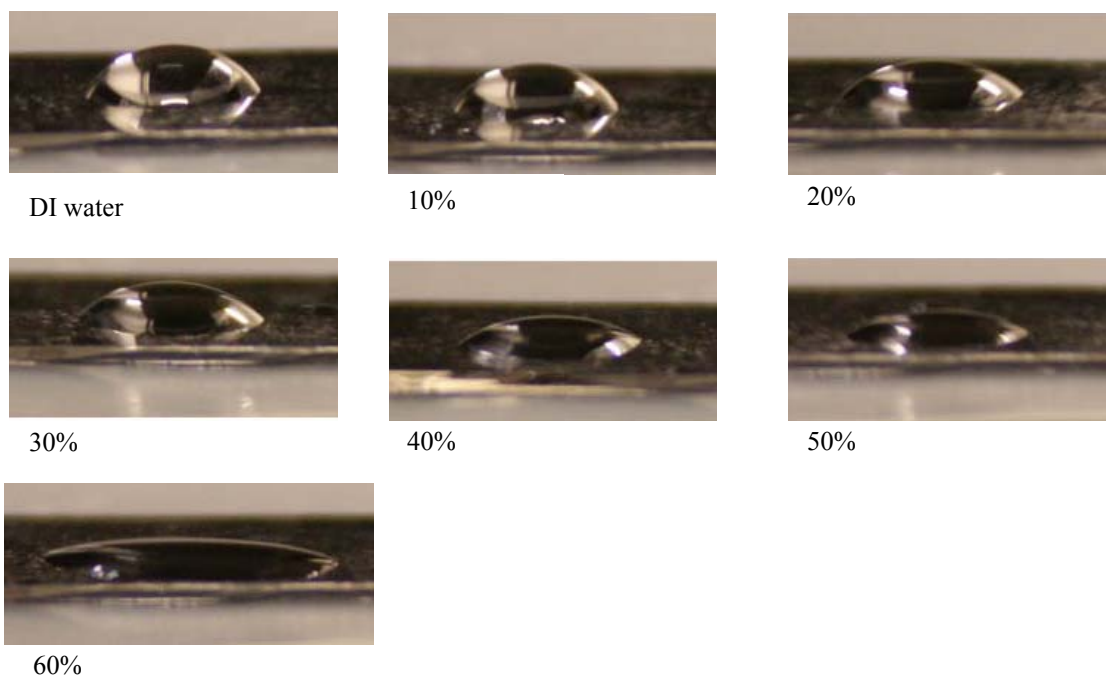


Figure 4.15: Images of contact angles for solutions of ethanol in water, by volume, on a hydrophilic surface (PEDA). Increasing the concentration of ethanol results in a decrease in contact angle. Below 60 %, a meaningful contact angle could not be discerned.

These values of contact surface tension and contact angle will be useful in computing the theoretical alignment forces.

#### 4.7: Measurements of Water Interface

The detection of the edge of the water droplet or aqueous ethanol droplet in the Nikon TE2000 microscope relied upon distinguishable features on the top and bottom slide surfaces that allow identification of the top and bottom boundaries of the fluid.

To see the boundary, water was placed between two glass samples. At 20x objective lens and a total of 200x magnification, the focus was varied so that the interface, a white line as viewed in the movie, advances to the front of the interface. We found that the interface can

only be seen through half of the focusing process. This is likely due to the lensing effect of the side closer to the objective defocusing the image on the side farther away.

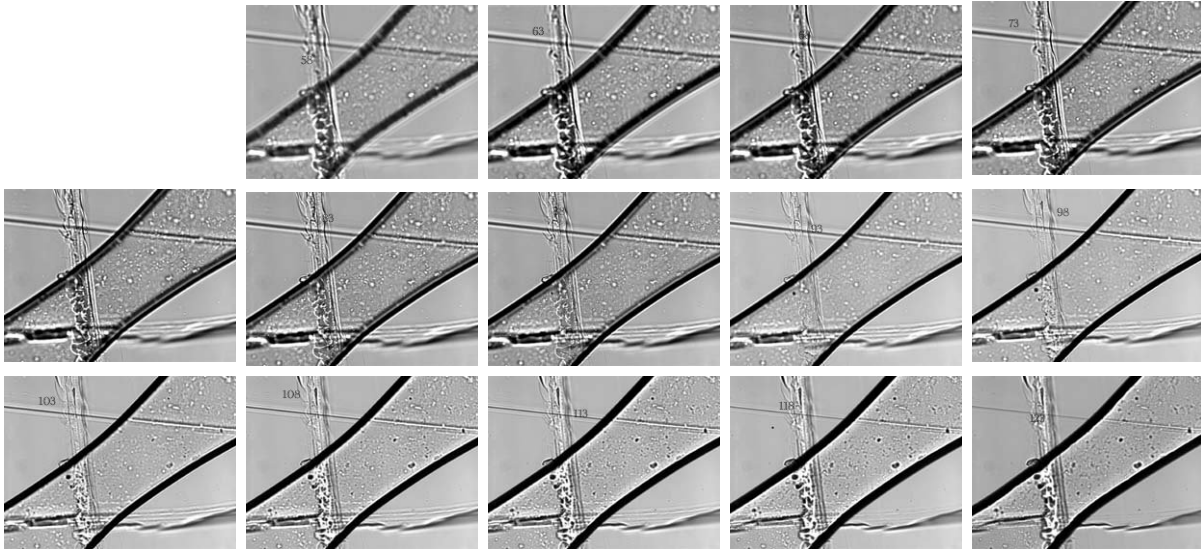
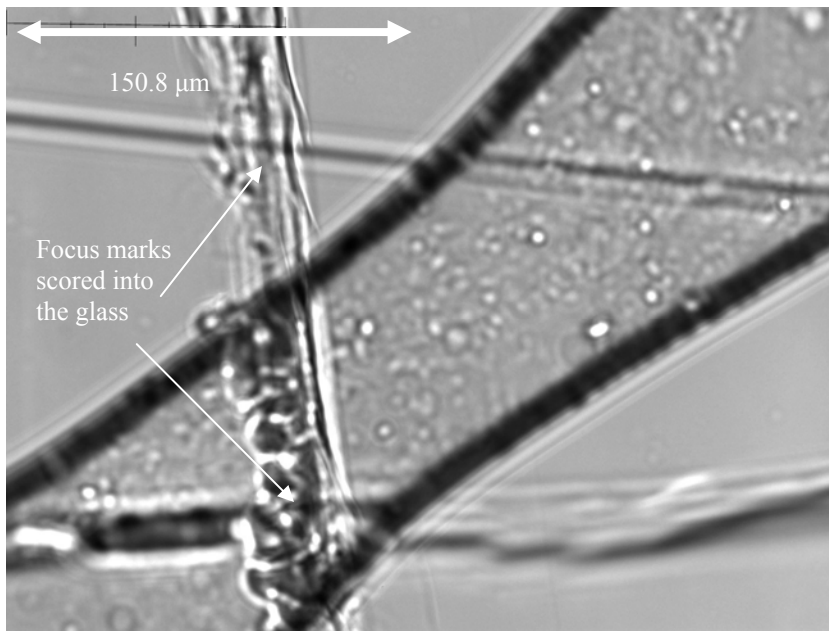


Figure 4.16: The pale line that advances with the change in focus is the water edge being measured. After a certain point, the water edge is occluded.

Since the slide is glass, it is mainly silicon dioxide, similar to the oxide layer on cleaned silicon wafers. Focus marks on the slides or silicon wafers are required to differentiate the surfaces and allow the measurement of the distance between the wafers. These were made by scoring the two glass samples with a diamond tip glass cutter, in perpendicular directions. These marks can be seen as imperfect lines in the images. The average measured height for the separation of the wafers due to the column of fluid is 120 micrometers.

Images were taken in 5 micron intervals, then later measured and analyzed using Adobe Photoshop and Gimp 2.6. The edge of the fluid was measured with respect to the entire edge shadow of the fluid, to find the overall shape.

The measured shape was a good approximation of the calculated shape, with inconsistencies explained by errors in measurement, which were not as precise as desired, due to the indistinct nature of the both the shadow edges and the water edge. For the water drop between the slides with no hydrophilic pattern, it is reasonable to assume that the fluid surface is symmetrical, and the un-measurable portions can be approximated and duplicated from the observable side.



Curve vs Height

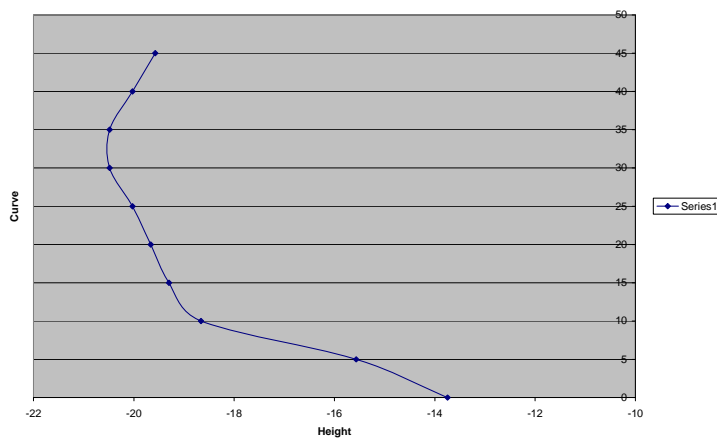


Figure 4.17: Focus marks were scored into the glass slides in 4.17a. In 4.17b, the curve was plotted to ascertain the shape of the water edge.

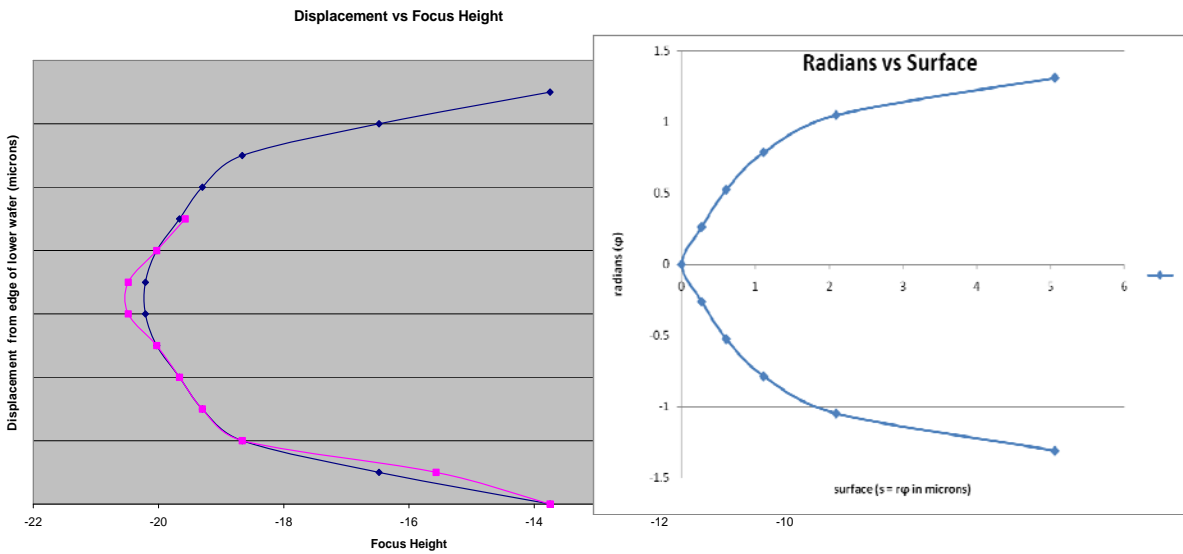
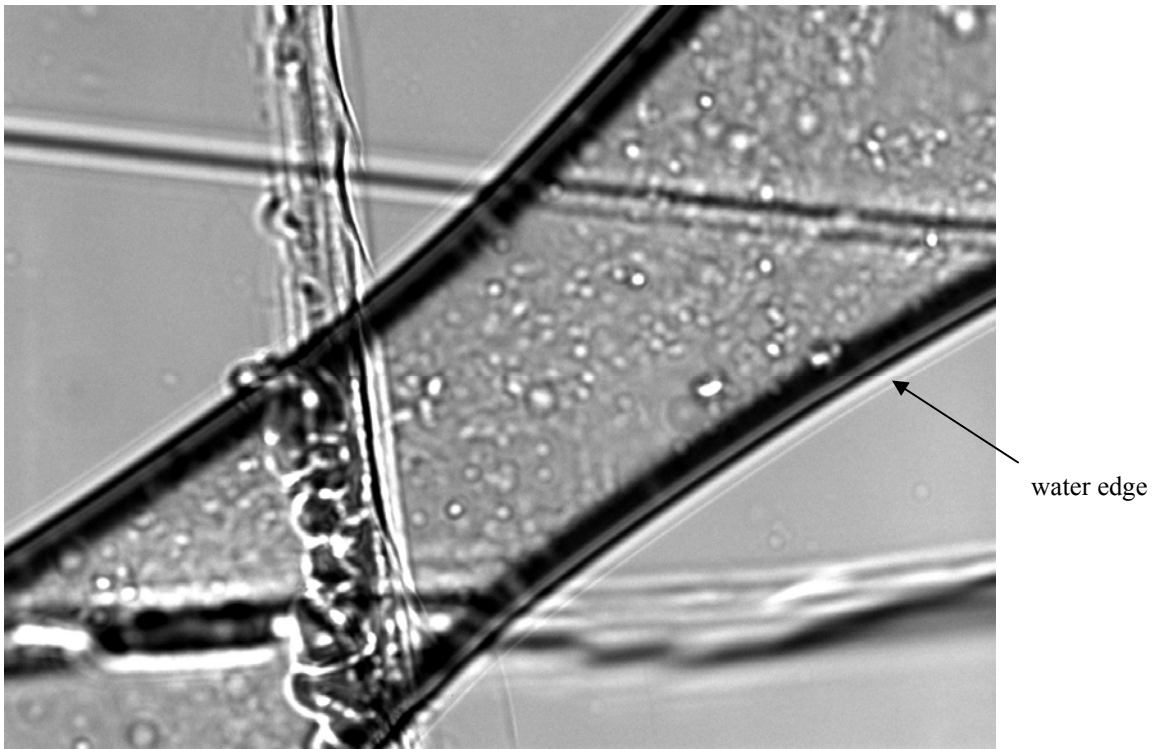
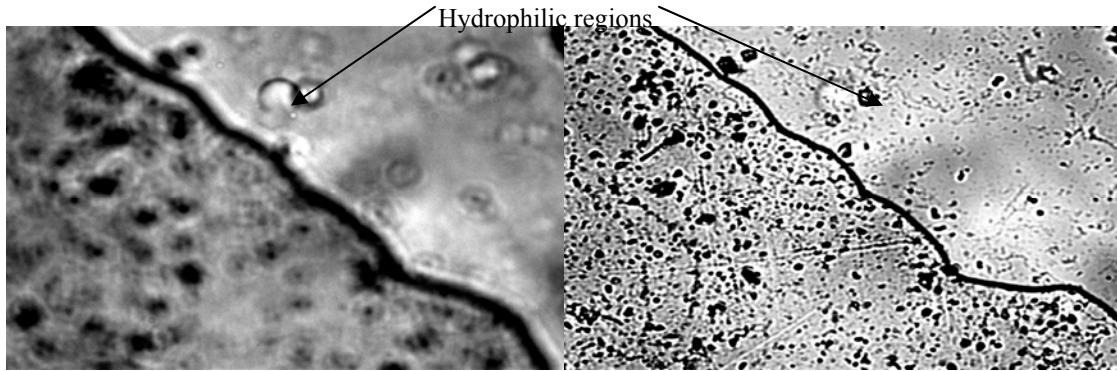


Figure 4.18: The white line shows the water edge that advances as the focus to the microscope is adjusted. Above is a comparison of the water edge measurement and the calculated shape predicted by energy minimization. There is reasonable agreement between the shapes.

Images taken of the fluid with the alignment pattern on glass show some differences in behavior from the images of fluid between clean glass wafers. In the pattern, the hydrophilic region holds onto the fluid, while the hydrophobic region shuns it. A clear line can be seen at the boundary between these regions. The liquid interface measurements can be seen in the graph below:



Displacement vs Focus Height

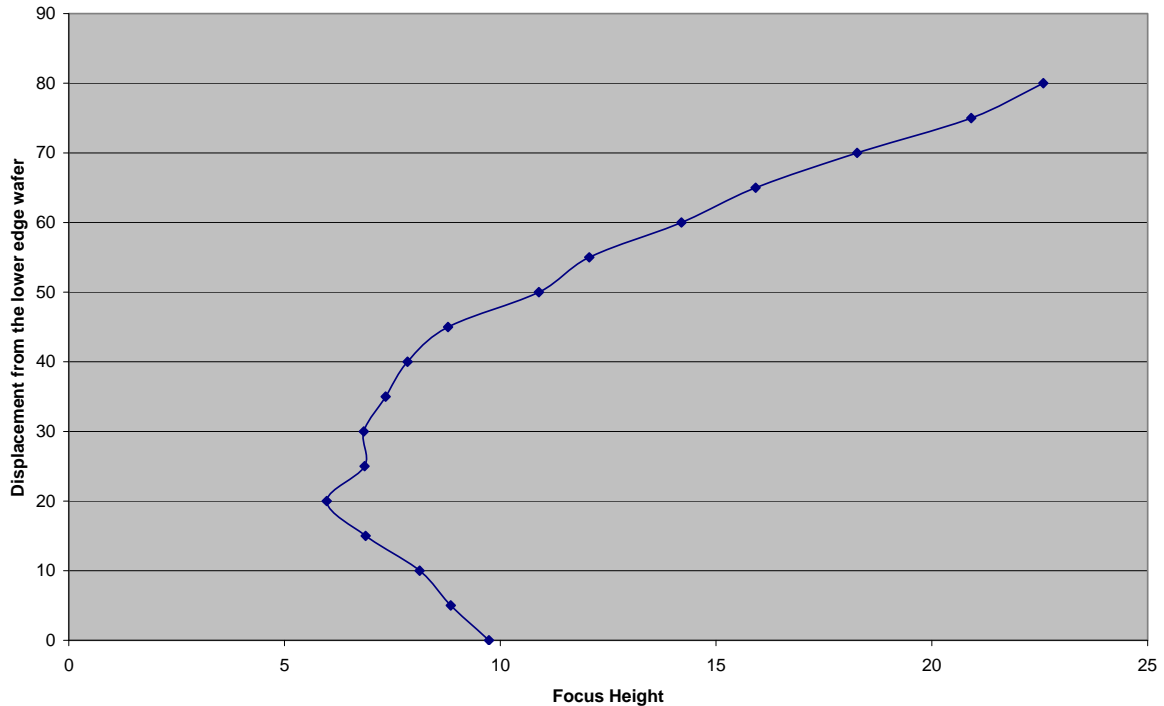
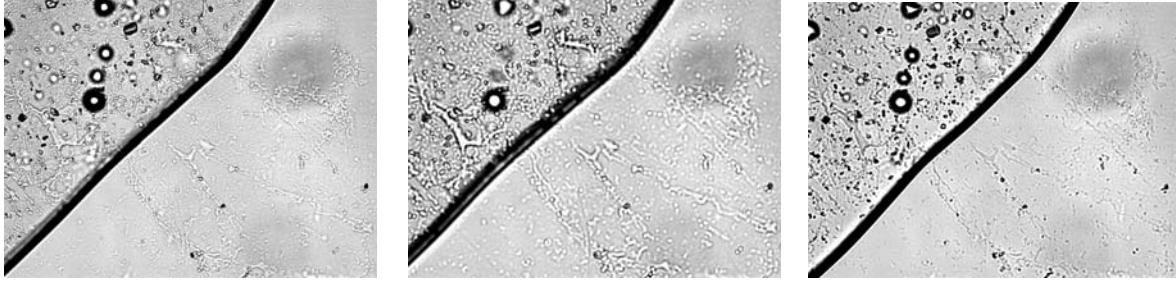


Figure 4.19: The water is confined to one side of the image by the hydrophilic and hydrophobic regions. The shape of the water edge should be the same, however.



**Displacement vs Focus Height**

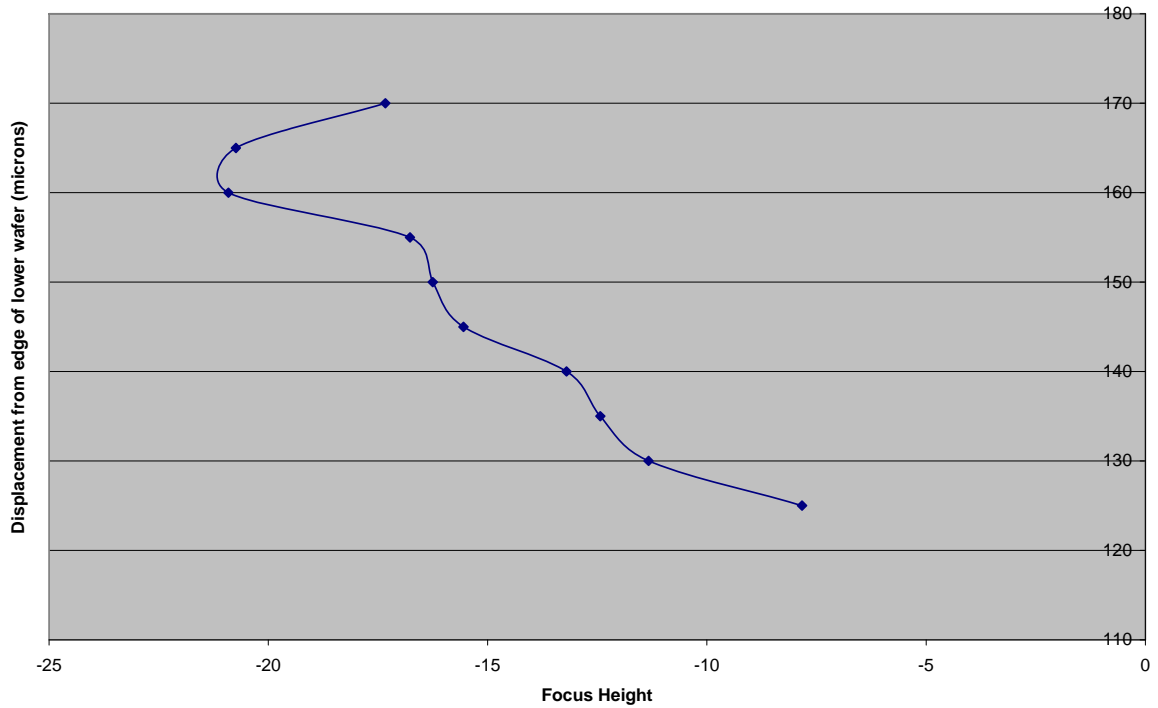


Figure 4.20: The pale line that marks the advancing water edge within the complete shadow can be seen to move to the forward edge of the shadow, but disappears after the halfway point. The graph shows another approximate shape of the water edge, but the shape is incomplete.

There were difficulties in imaging the water surfaces. The heat of the illumination increased the rate of evaporation of the fluid between the wafers. Contaminants on the sample interfered with the water edge, and the surface tension of the fluid. Surface

imperfections also interfered with the pattern. These difficulties contribute to the errors in water edge measurement.

#### 4.8: Measurement of the Unaligned Wafers interface.

When the wafers are deliberately pushed out of alignment, we expect to measure either portion of the curve graphed in figure 4.20c, for a small displacement, or a side of a parallelogram, for a large displacement. Because a shift in the wafers should represent a change in the angular limits, it is presumed that the off-set does not significantly change the shape of the fluid surface. With definite limits of integration, the model can be tested against the measured curve. The top wafer was displaced  $\sim 158.75$  microns using an 80 turn per inch precision screw. The figure below is a progression of the top view of the water edge as the focus is changed.

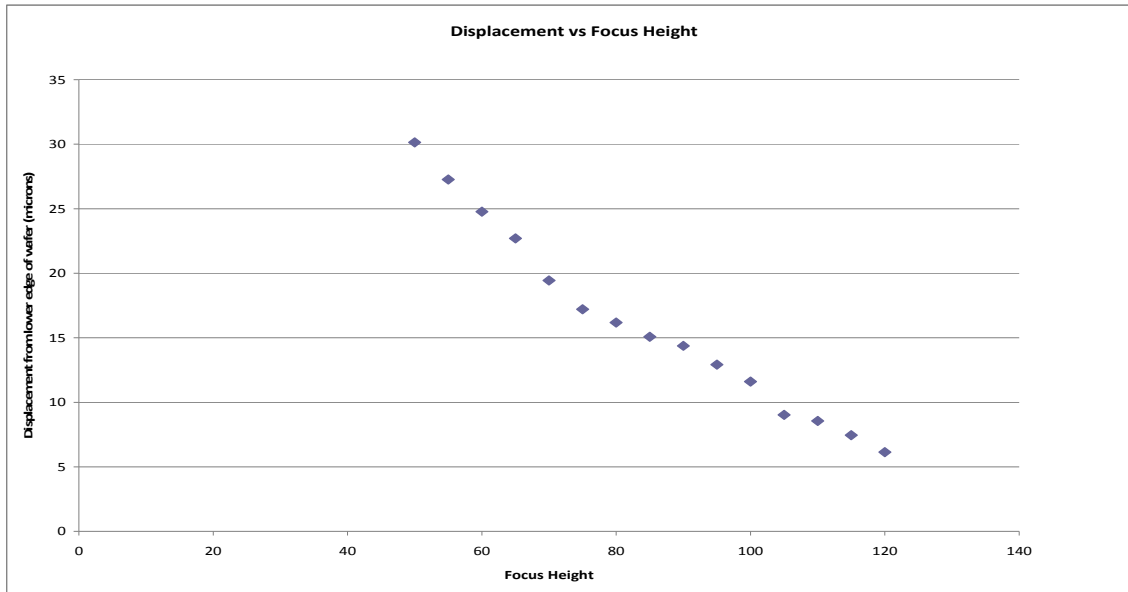


Figure 4.21: When the curve is misaligned, the water edge seems to take on a shape that suggested an almost flat line. Difficulties in measurement included evaporation of the fluid, as seen here in successive images.

#### 4.9: Conclusion

Alignment between wafers is a critical aspect in the formation of the 3-D package. During this phase, micron-level precision is required in manipulation of the wafers. Methods of wafer alignment include use of capillary force in sub-millimeter structures, gravitational sub-millimeter self-assembly, bridging flocculation and shape complementarity for self alignment, employment of dry, electrostatic traps for self-assembly in vacuum with ultrasonic agitation to overcome friction, previous work in wafer-level alignment using dry hydrophilic and hydrophobic alignment forces and our present method, use of SAMs and a lubricating solution to create an alignment pattern of wettable hydrophilic and hydrophobic regions. Experiments in dry alignment forces by Walker and the interfacial energies involved showed that the alignment based solely on these energies without the use of capillary forces would not overcome friction.

Experiments in self-alignment of full wafer samples by capillary force are performed in this study to show the viability of using surface-tension based alignment in the presence of these types of forces to move wafer scale objects. Complete self-alignment without manual assistance for these larger scales through mask design is the goal of these experiments. The alignment capillary forces of the fluid used between the wafers have a free energy associated with them. Our method relied upon a process that minimizes this energy. A model of the fluid surface was calculated using the method of variations, supposing a curved surface, a balance between the surface coming to a minimum shape and the compression limit of the fluid.

The detection of the edge of the water droplet or aqueous ethanol droplet in the large microscope relied upon distinguishable features on the top and bottom slide surfaces that allow identification of the top and bottom boundaries of the fluid.

To see the boundary, water was placed between two glass samples. At 20x magnification, the focus was varied so that the interface, a white line as viewed in the movie, advances to the front of the interface. It is postulated that the interface can only be seen through half of the focusing process. Images were taken in 5 micron intervals, then later measured and analyzed using Adobe Photoshop and Gimp 2.6. The edge of the fluid was measured with respect to the entire edge shadow of the fluid, to find the overall shape. The measured shape was a good approximation of the calculated shape, with inconsistencies explained by errors in measurement, which were not as precise as desired, due to the indistinct nature of the both the shadow edges and the water edge. For the water drop between the slides with no hydrophilic pattern, it is reasonable to assume that the fluid surface is fluid surface is symmetrical, and the un-measurable portions can be approximated and duplicated from the observable side.

Contact angles for solutions of ethanol in water were measured. Experimental values of the surface tension for similar concentrations of ethanol were found in literature.

## CHAPTER 5: ALIGNMENT MEASUREMENTS

### 5.1: Methods of Alignment Measurement

The challenge of creating a self-alignment system entails making a pattern of hydrophilic and hydrophobic SAM surfaces on our wafer substrates. This system allows the top wafer to move so that its pattern aligns with the pattern on the bottom wafer with micrometer precision once the fluid (either water or aqueous ethanol) had been introduced into the patterns. The self-alignment mechanism allows the stacked layers of the 3-D package to move without physically manipulating the wafers in the stack. There are several conditions that the alignment process must meet in order to be successful.

The self-alignment pattern needs to be an unlocking pattern, with blocked paths that will only open as alignment is attained. This prevents one part of the wafer from contacting the other before alignment is obtained. The friction caused by such contact will prohibit good alignment.



Figure 5.1: These patterns have a large initial capture area and narrow flow channels. Large corner areas allow the fluid to collect, and the small flow channel features let the fluid drain completely when alignment is achieved. This is shown when the wafers are off-set more than one time and eventually fail to realign. For experimental data collection, the final flow channels have been eliminated, so that realignment can be measured several times. The removal of these edge channels slows the release of water from between the wafers, but does not stop it completely.

Each stage of alignment releases fluid to the next set of areas of the pattern and minimize the surface energy of the fluid until final alignment that leads to a release of extraneous fluid from between the layers. Alignment relies on capillary action to enable the aligning fluid to move through the hydrophilic paths. The pattern needs to allow both lateral and rational motion to aid in energy minimization. Finer and finer details at the edges of the pattern are isolated until “unlocked” by alignment.

The fluid in the alignment pattern is required to provide the buoyant action of the fluid on the top wafer.

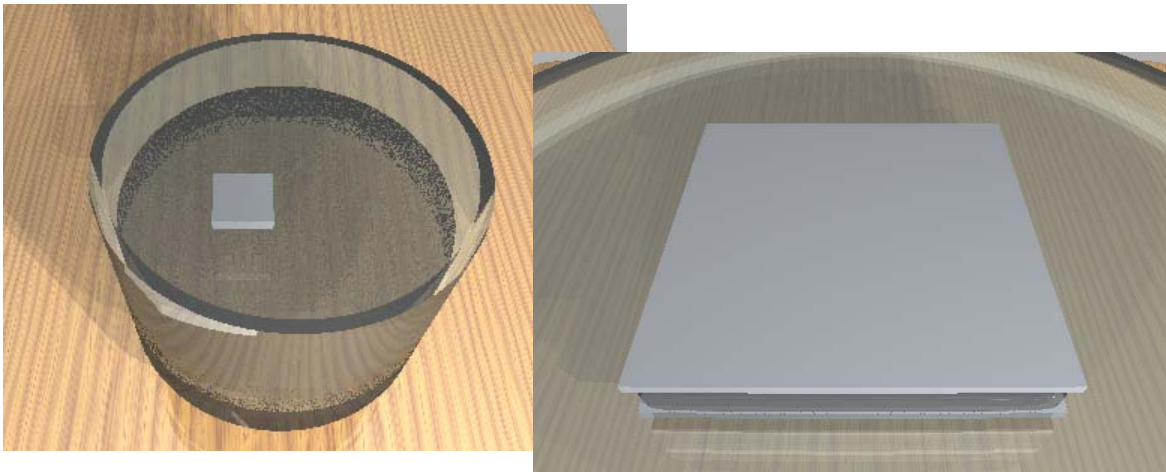


Figure 5.2: Illustration of buoyancy of silicon wafer due to the alignment fluid. The fluid supports the weight of the top wafer in this simulation.

Silicon is denser than water or aqueous ethanol. In a beaker with sufficient fluid the surface tension can cause the top wafer to float, as shown in figure 5.2 a. The same phenomenon needs to occur for the narrow channels of fluid between the wafers that do not cover the entire surfaces. When there are flow channels that go all the way to the edge of the pattern, the weight of the top wafer eventually forces all of the fluid out of the pattern. This is an

open pattern. When the edge of the pattern is closed, so that there are no flow channels out of the pattern, the fluid is retained longer, but still escapes eventually from between the wafers due to leaks or evaporation.

These wafers must move independently of each other so that one alignment phenomenon between two wafers does not interfere with other alignment phenomena occurring between other wafers in the stack at the same time. The ability of the stack to self-align using features engineered into the design will cut costs on development of machines to perform the same task, and cut production time of the RF module.

The size of the vias requires that the layers must align with micrometer precision. The vias that carry information between the wafers measure on the 10-20 micron scale. The precision required presents its own challenge in the design transfer. There is the possibility of error in the photolithography process, such as non-uniform/under exposure of the photoresist before the oxidation process. Another such error can occur in centering the pattern on the wafer, making the edges of the design inexact.

The creation of the hydrophilic pattern using oxidation requires the use of ozone. The oxidation solution tends to dissolve the photoresist. Oxidation by ozone is cleaner and does not strip the photoresist, but if the ozone coverage is not even and constant, part of the pattern might not oxidize to hydrophilicity. This problem might be corrected by further ozone exposure, but there is a risk of removing the SAMs layer entirely.

The self-alignment procedure included mask design, sample wafer fabrication, redesigning and recalibration of the force table and measurement of the alignment force.

## 5.2: Force Table Redesign

The apparatus needed to measure the restoring force of the surface tension was the modified force table. The sensor was changed from a large force cantilever to one capable of sensing very small forces and very small changes in the amount of force being applied to the sensor by the aligning mechanism. The table configuration was also modified from a pulling force measurement mode back to a pushing force mode. In this mode, the deflection of the sensor had to be taken into account, as this deformation had an effect on the data.

To modify the table, the L-rail stage with restraining clamps was removed and the original platform-stage was replaced. The 20 lb cantilever was replaced with a 1 oz sensor. The force table VI was recalibrated to give accurate readings for the more sensitive sensor.

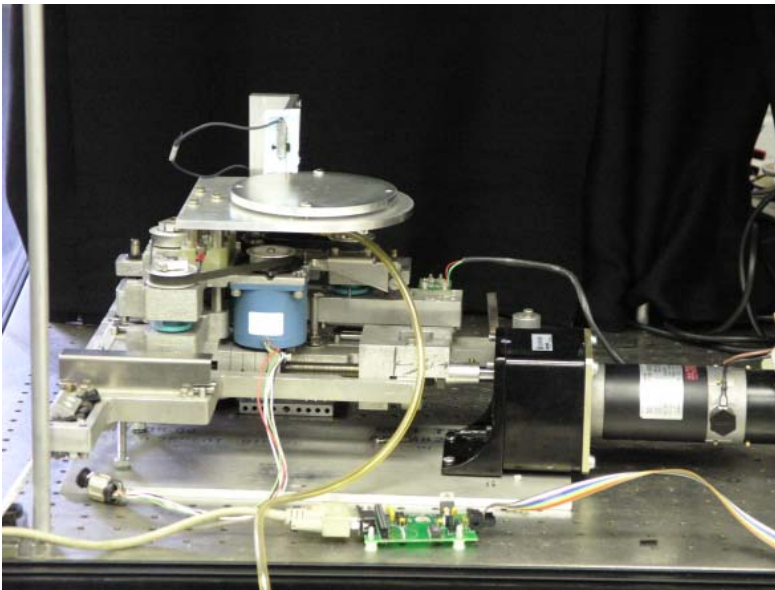


Figure 5.3: The force table was rebuilt to its original configuration to measure the alignment force between the wafers with the intervening fluid acting as the driving mechanism.

The motor moved in steps of approximately 20 microns per turn. The stage, rather than the force meter arm, could be made to move forward or backward, at need.

### 5.3: Mask Design

The previous alignment procedure called for hydrophilic regions of bare silicon and hydrophobic regions of vinyl, the functional group terminating the non-reactive end of the 10-UTS SAM.

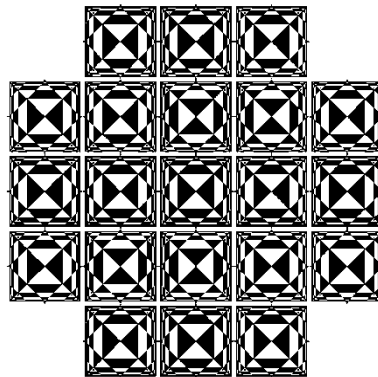


Figure 5.4: Alignment patterns from previous study by Walker. There are actually 21 identical patterns in this figure, laid out to maximize the 'real estate' of a 3" wafer.

The design requirements for the previous alignment study included [Walker, 2006]:

- Large capture area
- Greater forces near critical alignment
- Small features away from center
- Non-periodic features
- Hydrophilic zones large enough to maintain water sufficient to suspend top wafer

In Walker's study, a thin layer of a solution of ethanol and water was placed on the lower wafer. The top wafer was placed so that its pattern matched the pattern of the bottom wafer. Then the system was disturbed to misalign the wafers. The system had a capture range of a few millimeters.

For the next phase of alignment, several parameters must be modified. First, more precision is needed in the measurements. The previous imaging procedure based on a ½” CCD camera (NTSC) attached to a low power ‘dissection’ microscope had a precision of about 20 microns. This measurement can be improved by using a more powerful microscope with the infrared filter removed. With samples made of double side polished silicon, it should be possible to see the alignment through the silicon using an infrared source. An alternative is to produce the pattern in glass, which should have the same surface properties as the wafer.

Next, more hydrophilic and hydrophobic materials are needed. These materials also need to be the SAMs that are to be used for bonding. In this case, the hydrophilic regions need to be carboxylic acid terminated SAMs and amine-terminated SAMs, and the hydrophobic regions need to be either methyl- or vinyl-terminated SAMs.

Finally, flow channels need to be an integral part of the pattern design. There actually need to be two versions of the design, one with flow channels all the way through, and one with only interior flow channels, with the exterior ones removed so that the alignment can be shown to be repeatable with the same wafer many times.

The originally redesigned mask consisted of curved segments, but the process that manufactures the hard masks requires straight lines and sharp corners for maximum precision.

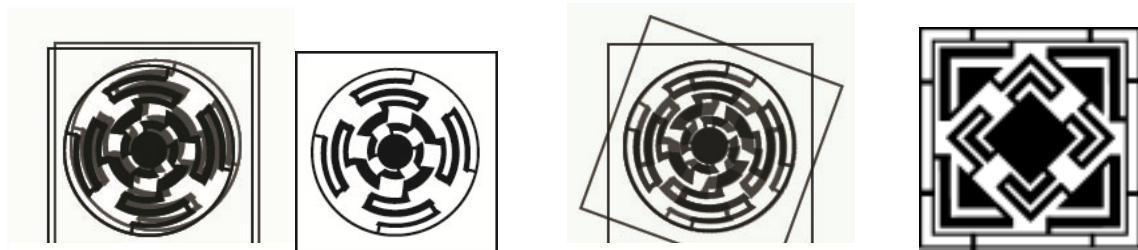


Figure 5.5: The early designs for the mask with flow channels eventually evolved into the angled pattern for greater precision in mask fabrication.

The mask incorporated the diminishing capture features at the out edges in a similar fashion to previous mask designs in the unlocking pattern.

#### 5.4: Alignment Pattern Fabrication

To make the alignment pattern of hydrophilic and hydrophobic regions, the following procedure was used. The wafers were cleaned according to previous descriptions. A self-assembled monolayer, terminated with a hydrophobic functional group, was deposited on the wafers. In this case, the functional group was vinyl, since a 10-UTS layer was put down. Then, using our photolithographic process, the alignment pattern was placed over the SAM with a positive photoresist mask that covers the areas that were designated to be hydrophobic. The exposed areas would be hydrophilic.

For the carboxyl pattern, the exposed region needed to be ozonated for a short duration and then hydrolyzed. This process broke the vinyl double bond between the carbon atom and the oxygen and replaced it with a hydroxyl group. The photoresist is then removed.

For the PEDA pattern, the exposed region would be ozonated for a longer duration, to remove the self assembled monolayer entirely. Since the photoresist is much thicker than the SAMs, it should not be completely removed before the SAM is. With bare silicon, the wafer can be put back into deposition in PEDA solution. Then the photoresist would be stripped off, taking the excess PEDA with it.

For convenience in initial trials, alignment was achieved with top and bottom wafers fabricated with mirror-image patterns derived solely on 10-UTS SAMs. The photolithography process included spin-coating the samples with photoresist, baking for 3

minutes at 115° C, placement in the mask-aligner and exposure to UV for 7.5 seconds, then development in Microposit Developer 319. The samples were rinsed in DI water, dried with nitrogen and placed in the ozonator for 11 minutes and 30 seconds. They were then rinsed in the photoresist stripper for 30 seconds, and in two different DI water rinses, the first to remove the remaining chemicals, and the second to hydrolyze the surface. This process formed carboxylic acid in the exposed areas.

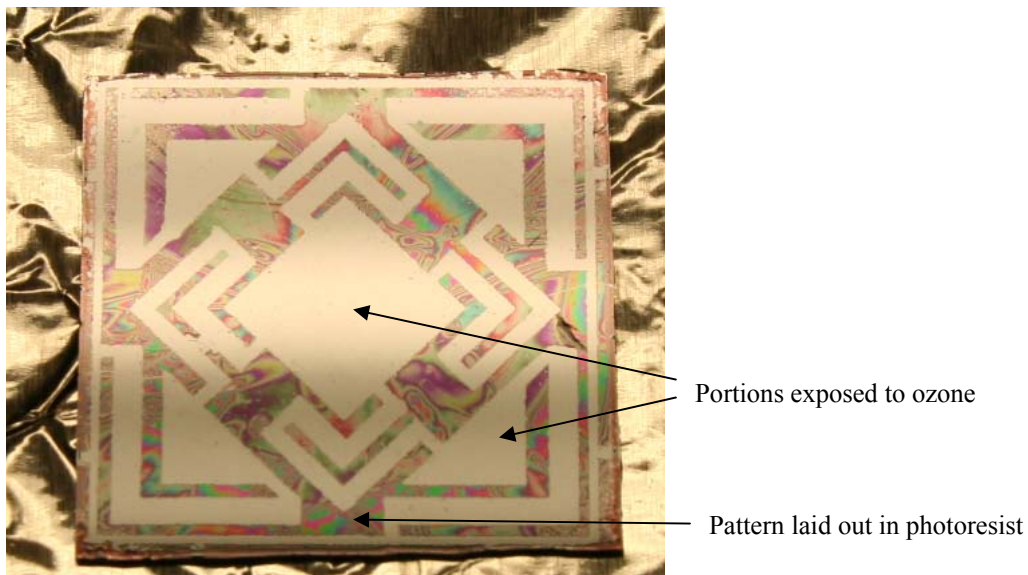


Figure 5.6: The alignment pattern has been developed on the SAMs coated wafer. The silver portions are the silicon with SAMs, and the reddish portions are the photoresist. This wafer is ready to be ozonated to make the pattern active.

### 5.5: Theoretical Calculations of the Alignment Force

The complex model of the actual alignment pattern presents more of a challenge for computing the area changes that give rise to the restoring force, because of its complexity. Since not all of segments of the pattern are parallel to the edge of the wafers, and the segments are of varying widths, changes in orientation contain will still contain both parallel and non-parallel surfaces. Table 5.1 shows the measurements for different segments of the

actual pattern. Table 5.2 shows the predicted relationship between the force and the displacement, where the surface tension behaves like a spring constant.

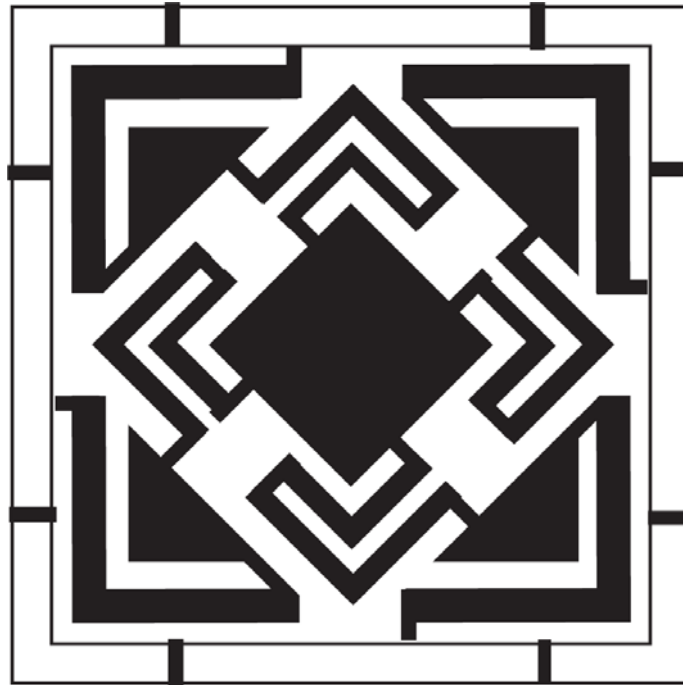


Figure 5.7: Lengths of the alignment pattern. Many of the lines are at  $45^\circ$  to the edges, so that both the x and y cosines must be taken into account. Below are the measurements of the periphery of the different shaded areas.

Table 5.1: Lengths of the different areas of the pattern.

Dark Regions	x (microns)	y (microns)	Dark Regions	x (microns)	y (microns)
Center	6062.98	6062.98	8th branch front	1529.08	1529.08
1st branch front	1325.88	1325.88	8th branch back	1099.82	1099.82
1st branch back	419.1	419.1	9th branch front	0	8204.2
2nd branch front	3228.34	3228.34	9th branch back	0	8874.76
2nd branch back	2113.28	2113.28	10th branch front	0	6990.08
3rd branch front	2809.24	2809.24	10th branch back	0	9649.46
3rd branch back	2476.5	2476.5	Periphery	0	25046.94
4th branch front	1846.58	1846.58	Periphery back	0	25664.16
4th branch back	485.14	485.14	Hypotenuse	5600.7	5600.7
5th branch front	4401.82	4401.82	Leg 1	0	5831.84
5th branch back	3228.34	3228.34	Leg 2	0	5831.84
6th branch front	3863.34	3863.34	Front 1	0	1069.34
6th branch back	3675.38	3675.38	Front 2	0	2151.38
7th branch front	1498.6	1498.6	Back	0	731.52
7th branch back	980.44	980.44			

Table 5.2: Prediction of restoring force.

x =0 .8 mm	$\gamma$ (N/m)	F (N)
	0.0726	1.02745
	0.0661	0.93546
	0.0557	0.78827
	0.0526	0.74440
	0.0500	0.70761
	0.0474	0.67081
	0.0463	0.65528

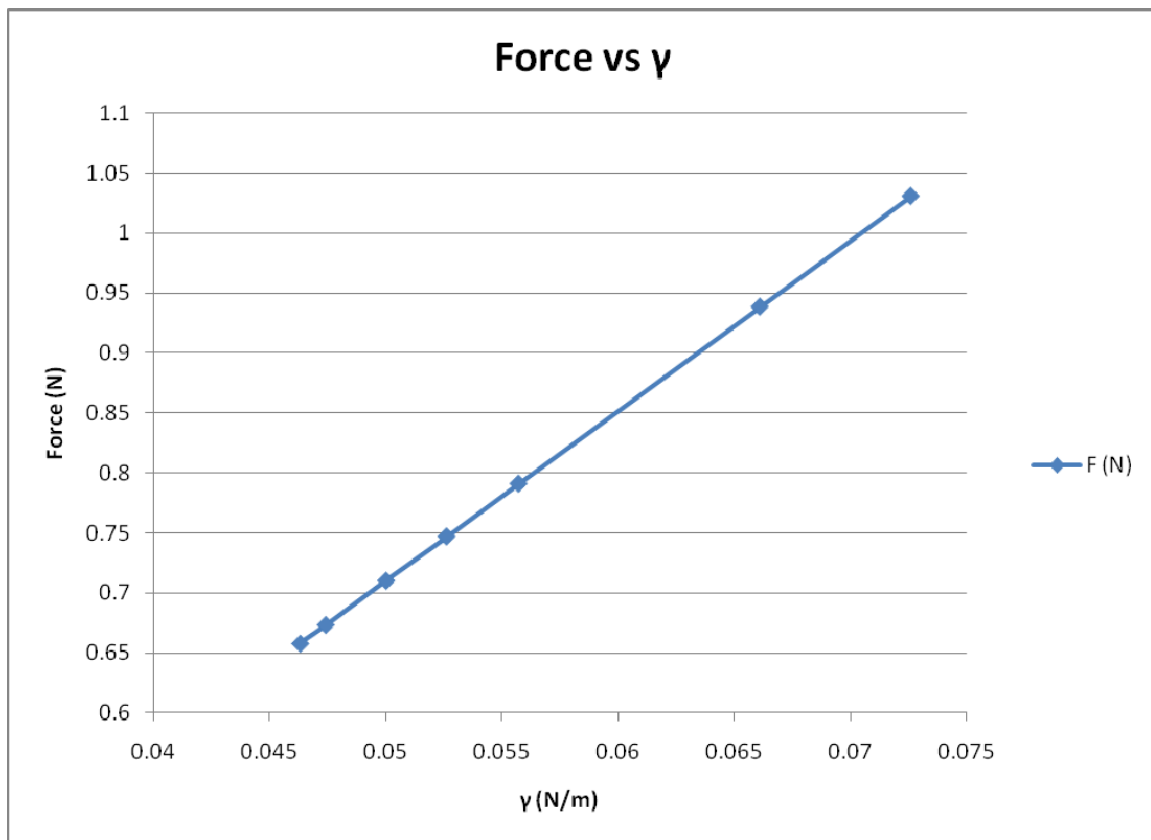


Figure 5.8: The force equation in Chapter 4 (Eqn. 4.43) predicted a relationship of direct proportionality between the surface tension and the force of alignment, akin to a spring restoring force.

The force equation gives good agreement with the measured forces at 0.8 mm. There is a clear relationship between the surface tension and the force exerted.

#### 5.6: Experimental Procedure

For alignment, experiments were conducted as follows. The stage was covered with parafilm. The parafilm was cleaned with HPLC grade isopropanol and dried with nitrogen. This film was to protect the wafers from dust and other contaminants that would destroy the pattern if they were to settle on the wafer surface. The LabView VI that controlled the motor was initiated, and the stage was positioned with the cantilever arm approximately in the center.

The wafers were stored under DI water, in beakers sealed with parafilm, to keep the patterned surfaces from drying and free from dust. Once removed from the beakers, they were dried with nitrogen and one wafer was placed pattern-side up on the stage. A drop of DI water, or aqueous ethanol was placed in the middle of the pattern (approximately in the middle of the wafer). Then the top wafer with the mirror image pattern was placed and allowed a relaxation alignment time of  $\sim 1$  second. If necessary, the stage height was adjusted, so that the force meter cantilever only came in contact with the top wafer. The wafer stack was positioned 1 mm from the force meter and the motor was set into motion. As soon as the stage was set in motion by the VI, force measurement data and position were simultaneously collected. The stage was allowed to advance about 3 mm, by which time the pattern alignment had broken (the pattern was off-set sufficiently that similar features were

no longer congruent). The VI saved the data as a rich text file, which was easily converted to an excel file for later analysis.

The pattern showed a strong alignment tendency for a few seconds, then, as intended, the liquid escaped through flow channels until the top wafer came to rest on the bottom wafer. If dried and rewetted (with a small drop of DI water in the center ~ 0.05 mL) the alignment forces came into play again.

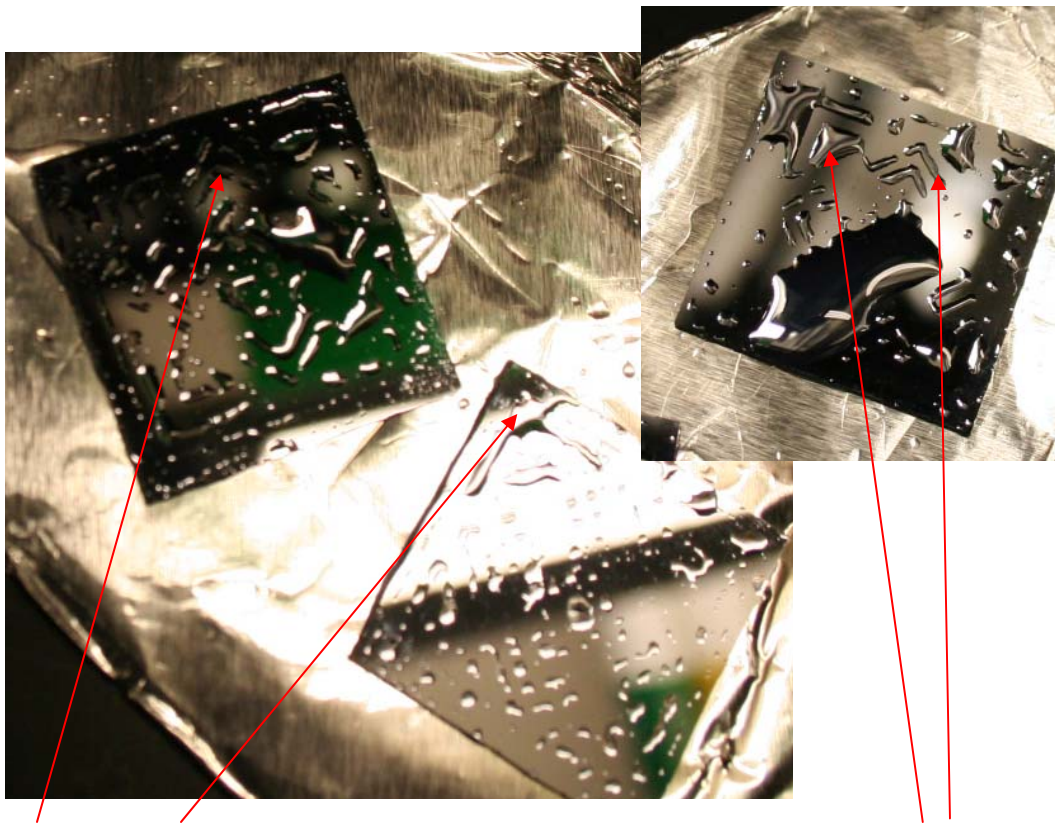


Figure 5.9: Portions of the pattern can be seen here, as the hydrophilic surface holds on to the DI water temporarily.

The nylon 6-6 solution showed an even stronger alignment tendency than plain DI water alone, and the alignment pattern could be seen more clearly with nylon 6,6 solution. Use of

the nylon solution, however, destroyed the pattern, as diamine molecules bonded with the exposed carboxylic acid functional group.

### 5.7: Force vs Displacement

As stated previously, the restoring force exerted by the liquid is generated as the area changes. The change in area is related by cosine to the change in displacement, as shown in figure 5.5. From the contact angle data, as the fluid mixture contains greater and greater concentrations of ethanol, the restoring force should diminish, as the surface energy gets smaller. This is due to the fact that the addition of ethanol weakens the cohesion of the fluid. On a graph of force versus displacement, the graph was expected to have a shallower slope when more ethanol was present. It was also expected that the force would level off at an increasingly lower value with increasing concentration. From previous investigation, the projected leveling off of the force plateau should have occurred at the corresponding surface tension calculation for concentrations of ethanol (as discussed in Chapter 4). This has not proven to be the case, and it is possible that the unintentional introduction of dust into the solution could have affected the results, since the experiments were not done in a clean room environment. Dust and other contaminants migrate to the surface of the liquid, breaking the surface tension. This can have a profound effect when measuring the alignment forces, lowering the readings by an order of magnitude. Evaporation of the ethanol from solution could also be partly responsible for inconsistencies in the readings. The speed of the force table, too, could have had an effect on the measurement of the break-away force. The faster the table moves, the more quickly the surface tension can be broken.

The following graphs are significant for the first dramatic change in slope of the force versus distance curves. Measurements were taken with different concentrations of ethanol, from pure DI water to 60% ethanol, in steps of 10% by volume.

Figures 5.10a and 5.10b show the raw data and the data after taking a rolling average. This was done to clearly show the behavior of the data points. Figure 5.11 showed the force versus displacement for DI water and 10% ethanol. The expected plateaus were 1.03 and 0.938 N, from table 5.2, but 5.11a showed one large peak, at 1.1 N and the remaining leveling out at  $\sim 0.3$  N. Figure 5.11b at 10% showed consistent plateaus between 0.175 and 0.2 N. In figures 5.12 and 5.13, 20%, 30%, 40% and 50% ethanol graphs showed no consistent grouping or slopes. Figure 5.13a, at 60% ethanol, showed one large, anomalous peak, and then some consistency at 0.2 N. Of note is the change of slope within each set of concentrations. This is attributed to dirt or some other contaminant affecting the surface tension of the alignment fluid. Figure 5.10 is one of the best plots, taken near the end of the experimental measurements.

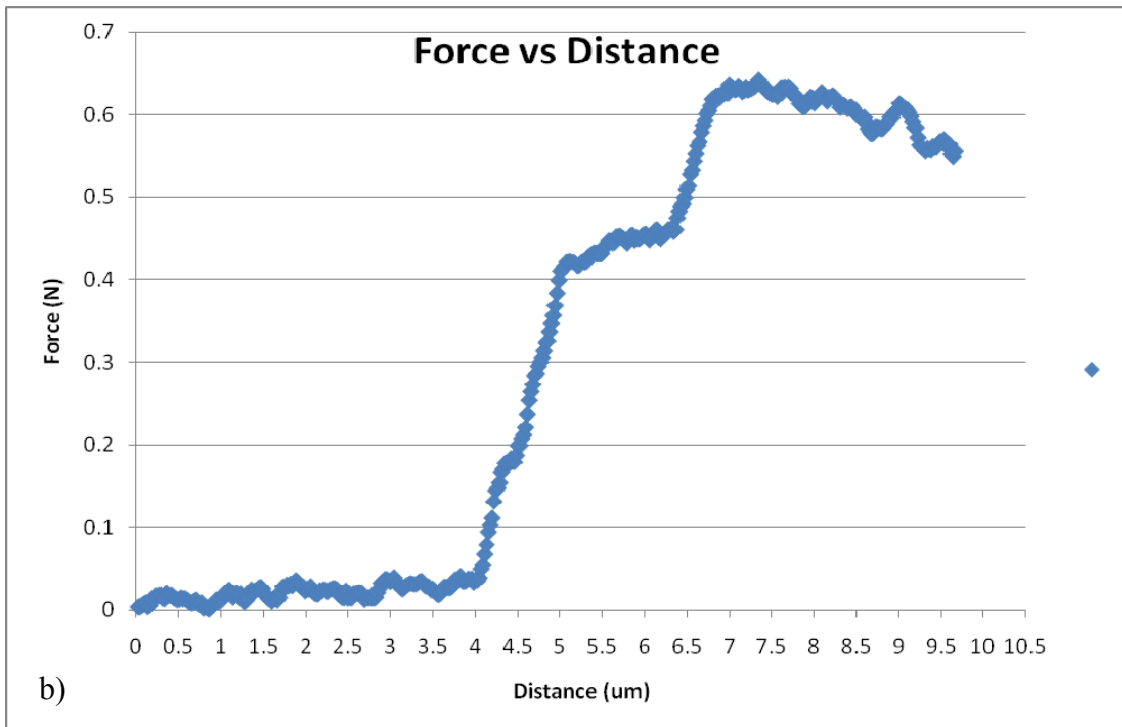
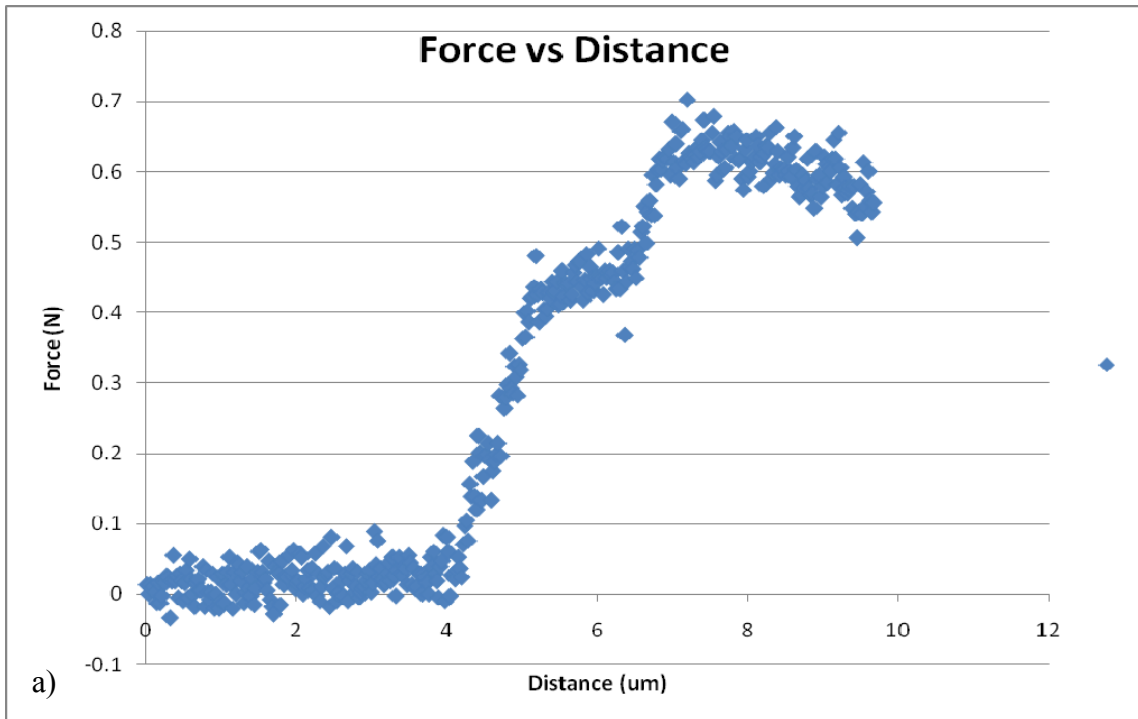


Figure 5.10: DI water (0 concentration of ethanol). a) The top graph is the actual raw data, and b) the bottom graph shows the behavior of the data using a rolling average of 10 values.

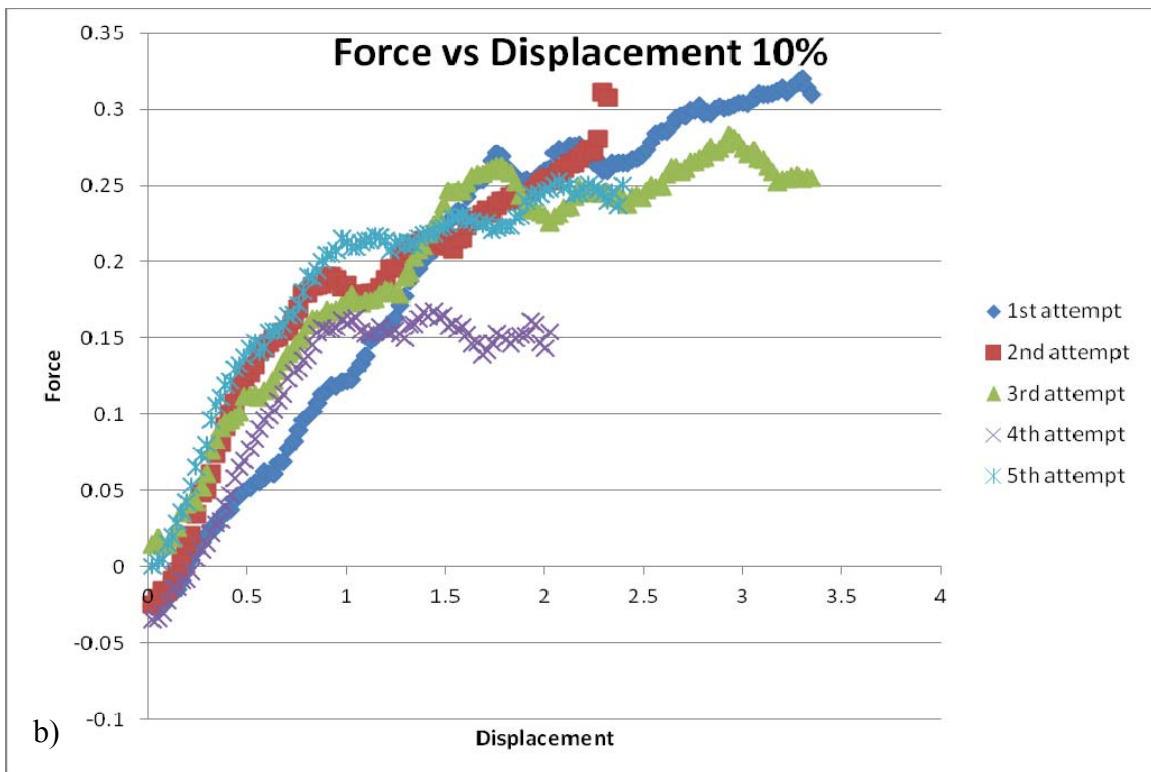
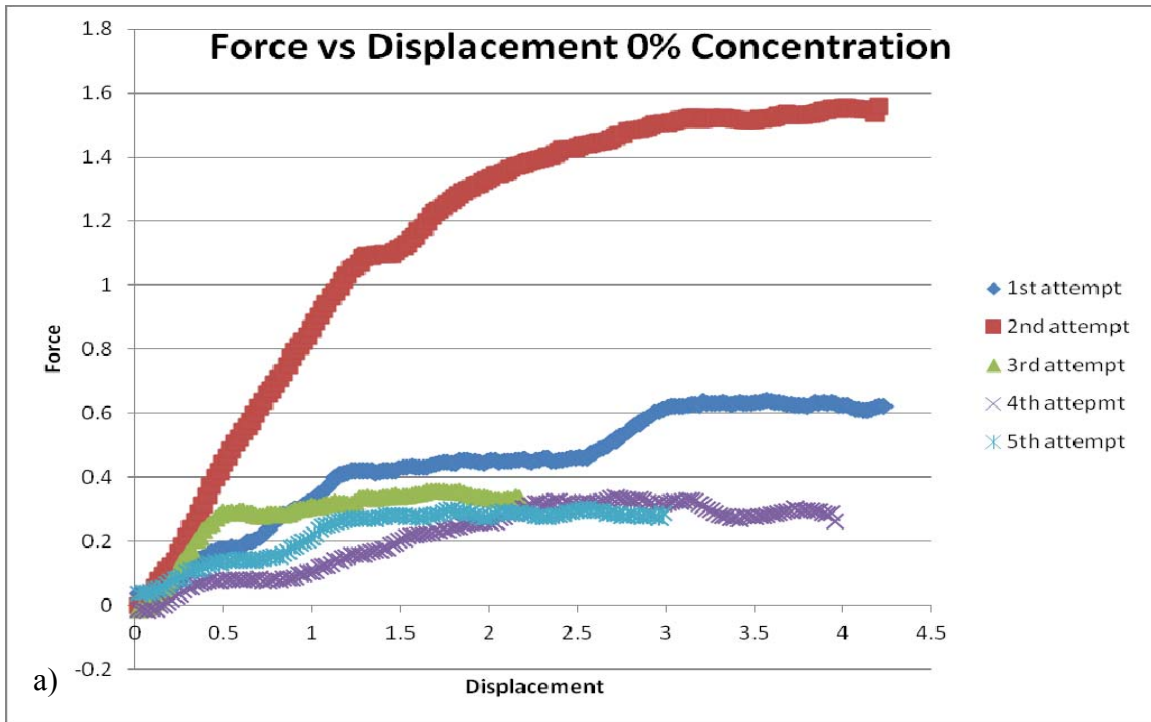


Figure 5.11: a) Above Deionized water force vs displacement chart (0 % concentration). The largest slope was 0.9. b) Below, 10 % concentration chart. The largest slope was 0.3.

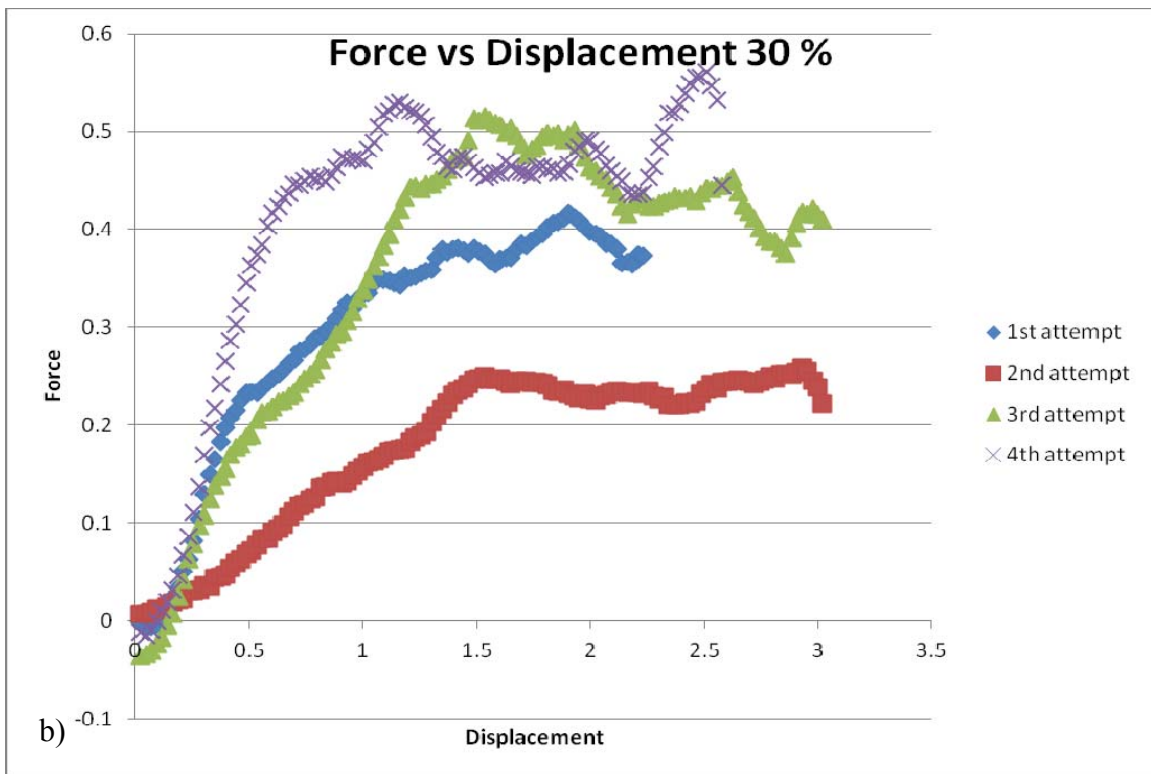
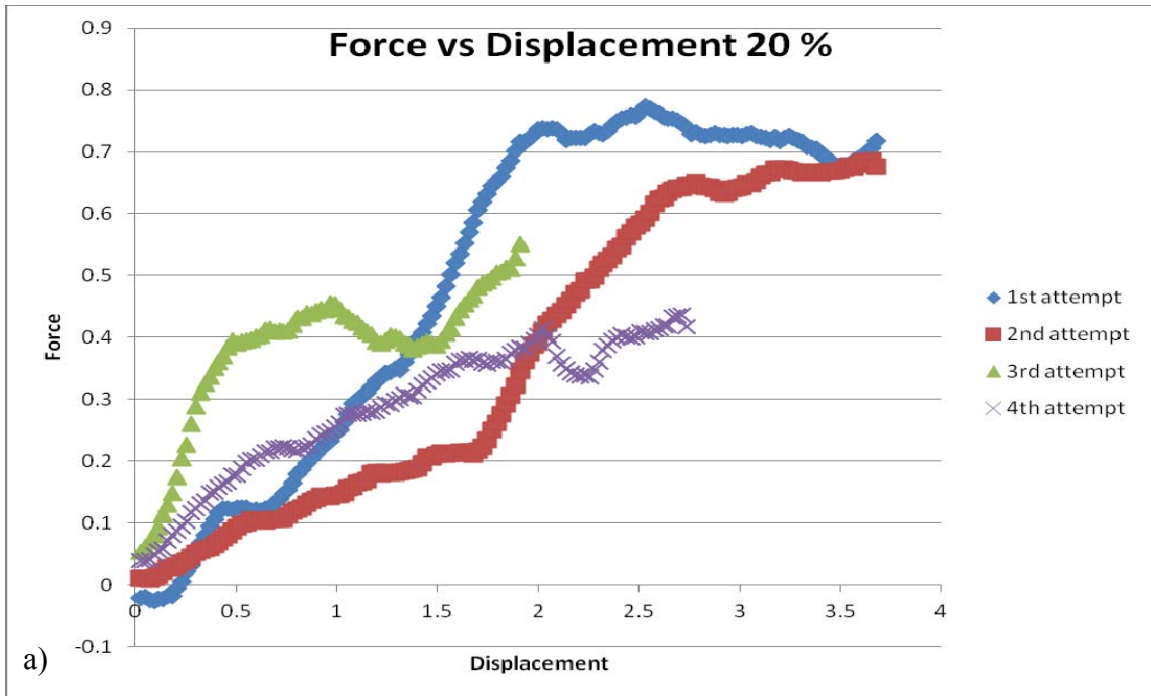


Figure 5.12: a) Above 20 % water force vs displacement chart. The largest slope was 0.89. b) Below, 30 % concentration chart. The largest slope was 0.85.

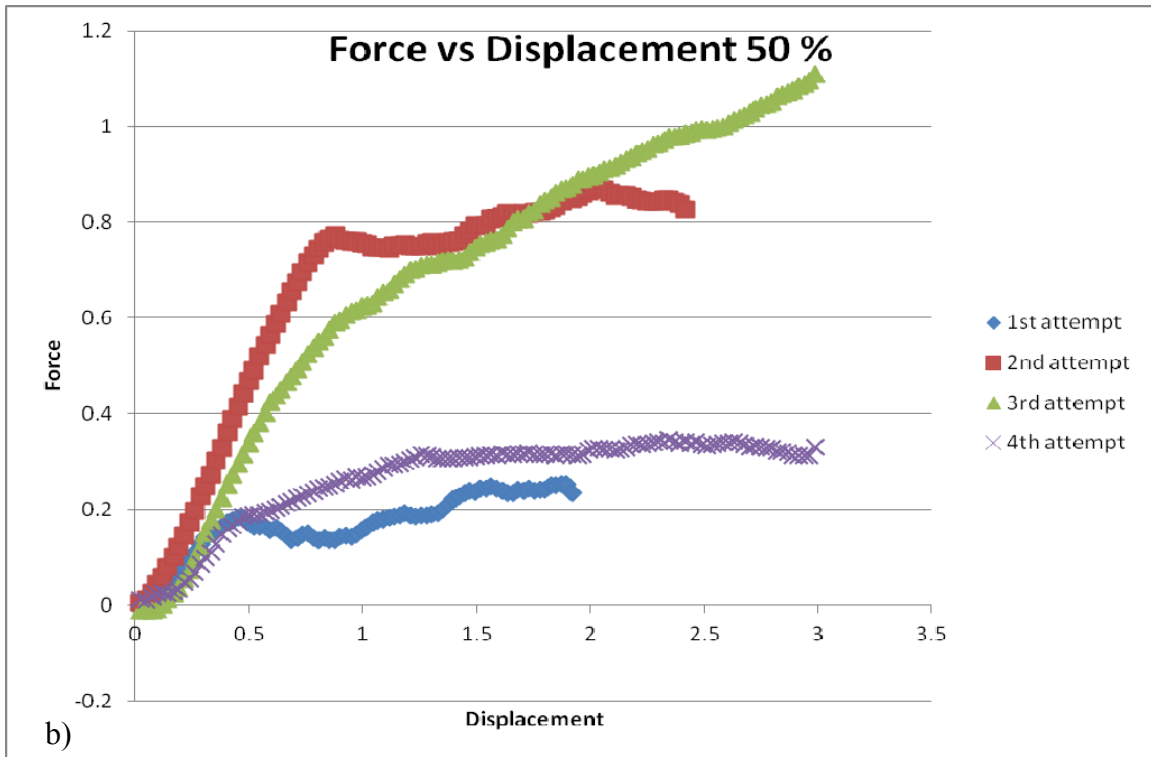
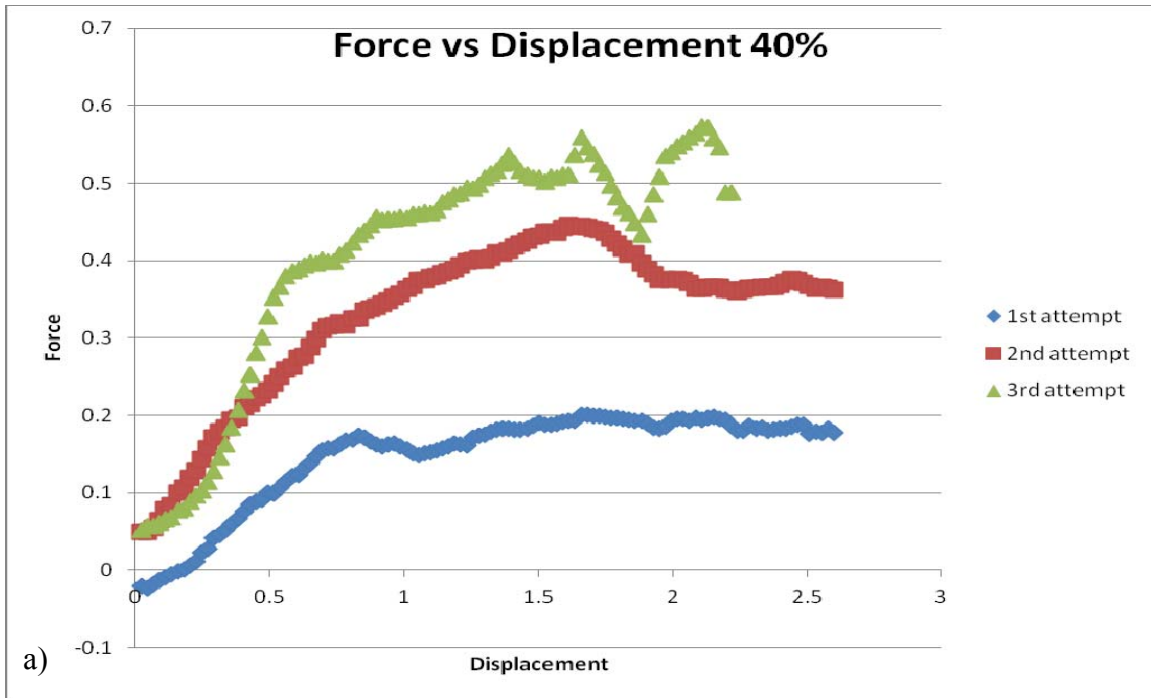


Figure 5.13: a) Above 40 % water force vs displacement chart. The largest slope was 0.6. b) Below, 50 % concentration chart. The largest slope was 1.0.

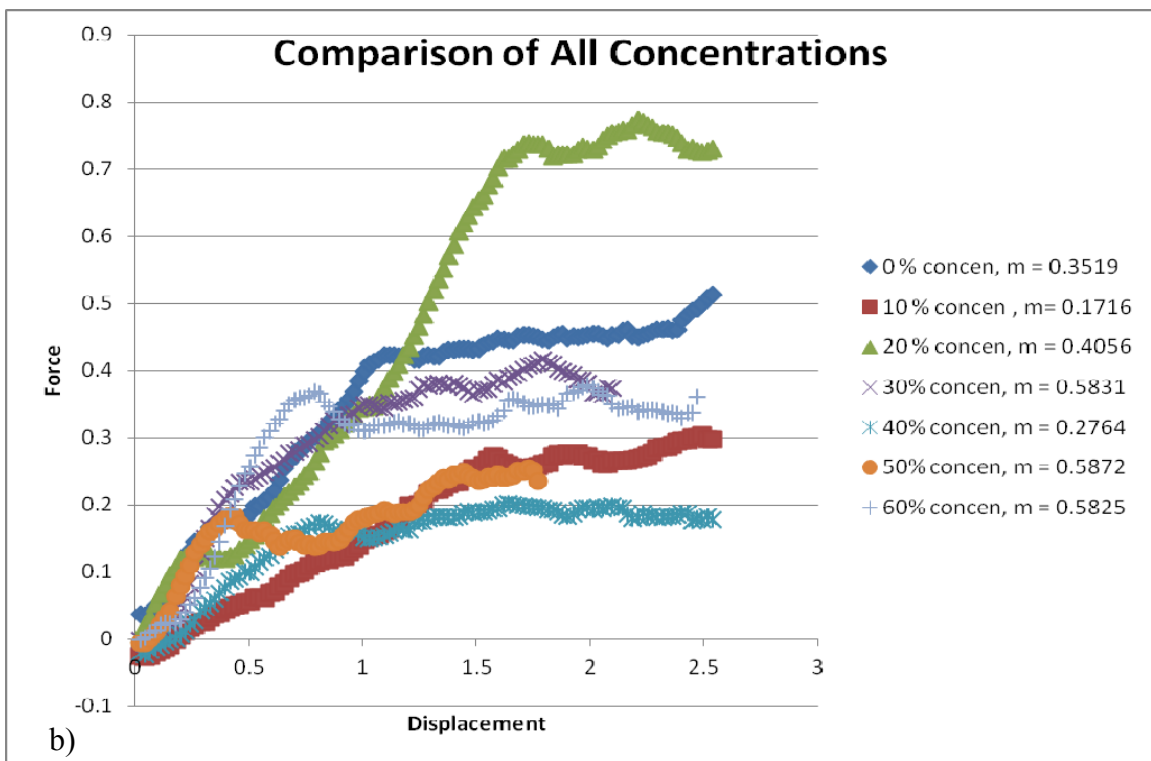
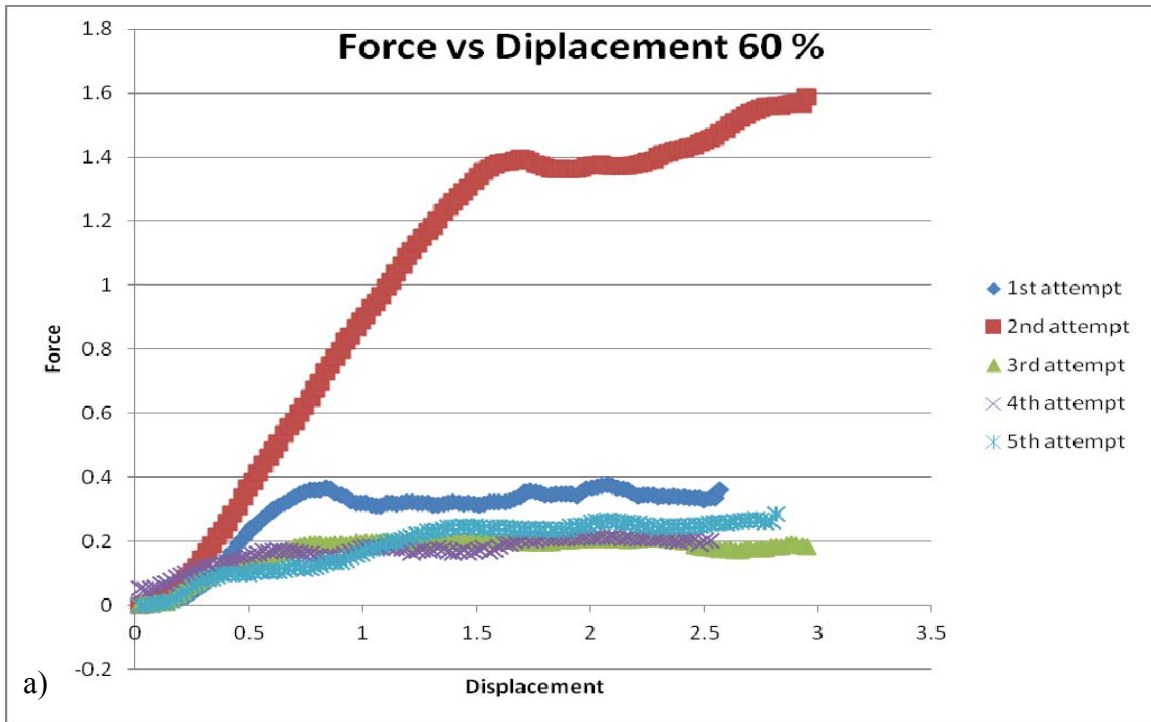


Figure 5.14: a) Above 60 % water force vs displacement chart. The largest slope was 0.98. b) Below, a comparison of all concentrations and their slopes. The largest slope was at 50% concentration at 0.5872.

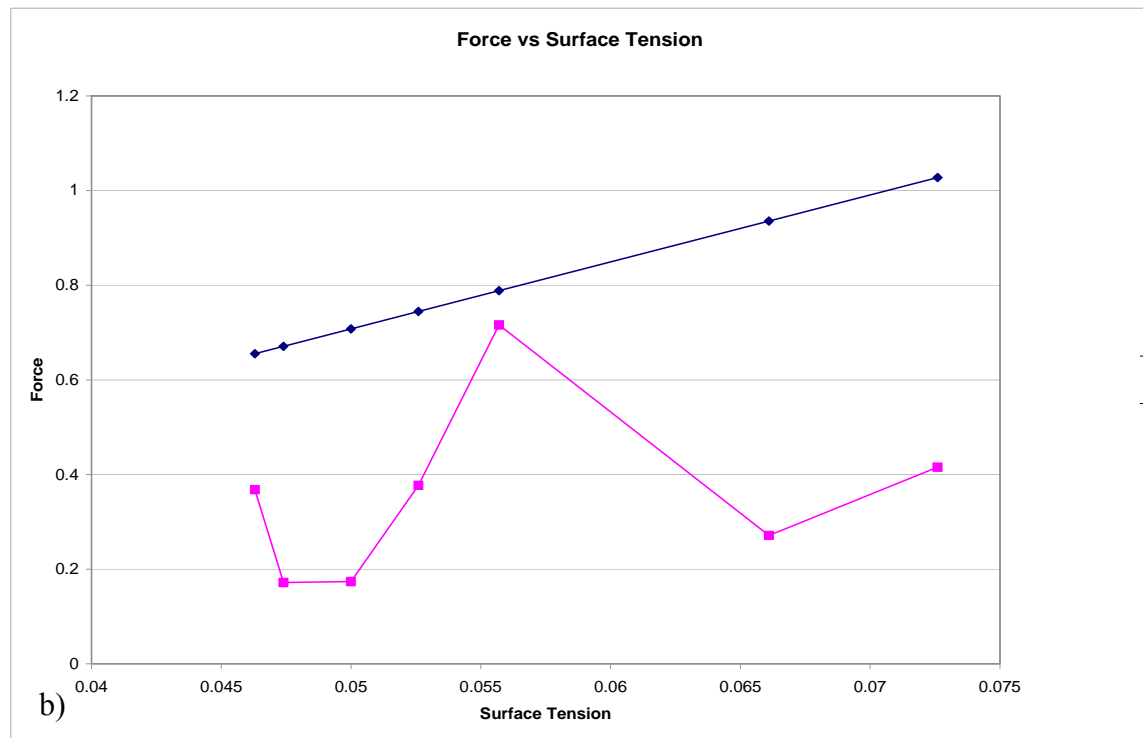
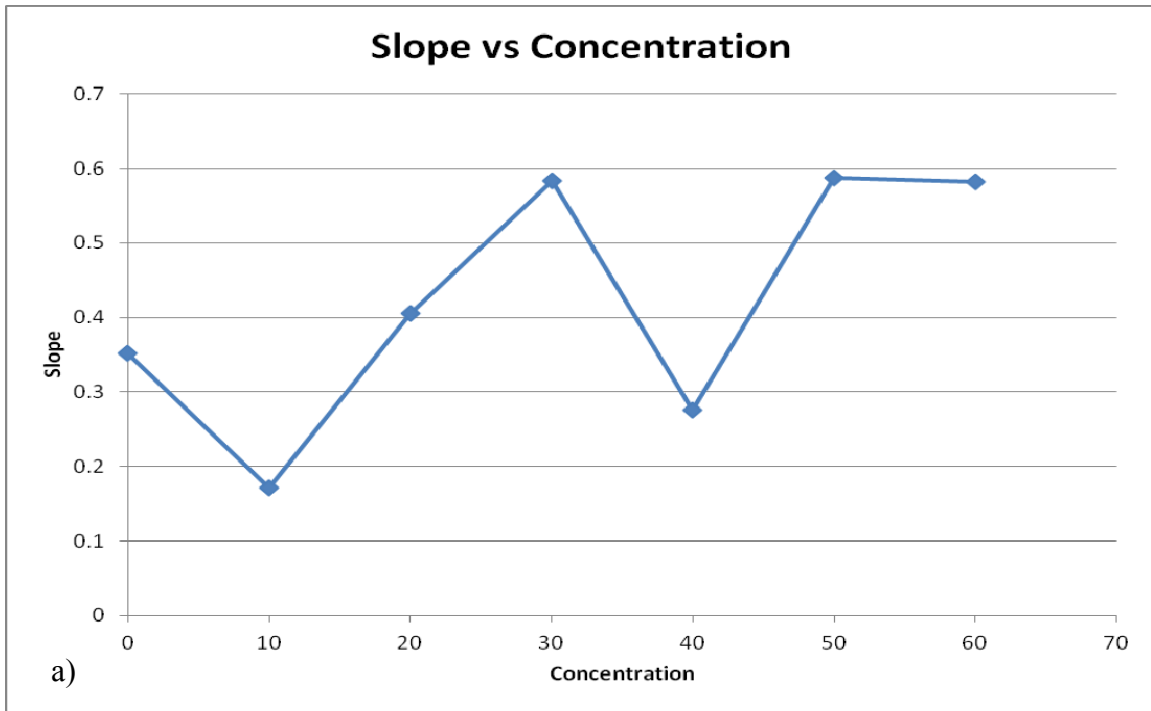


Figure 5.15: a) The slope showed an upward trend with increasing concentration, indicating consistency in the predicted surface tension. b) There was a correlation shown in the measured force with respect to the surface tension.

Future tests may show a stronger dependence of slope on concentration. Here, there seems to be the indications of an inverse relationship.

#### 5.8: Accuracy of measurement

Accuracy in the measurement was previously determined by alignment marks. These marks were integrated into the pattern, and at the aluminum deposition stage, these metallized alignment marks were protected from the stripping process with photoresist. In the previous study, a 20 micron alignment precision was achieved.

To measure the accuracy of the pattern alignment of our present samples, glass wafers were prepared. The edges were aligned and viewed through a TE5000 microscope. Because of the thickness of the glass slides used, the top wafer could not be viewed directly, but was seen as a shadow, as shown in figure 5.16. When misaligned, the shadow becomes extended, and light areas appear where there is significant spacing between the top and bottom wafers.

A precision of 8.6 microns or less was achieved within my research experimentation. Here, edge to edge examination is used to determine the accuracy of the pattern. Since the edges of the glass samples are not clearly defined at 20x magnification, the difference in overall width of the edge-shadow was contrasted before and after misalignment, using Gimp 2.6.

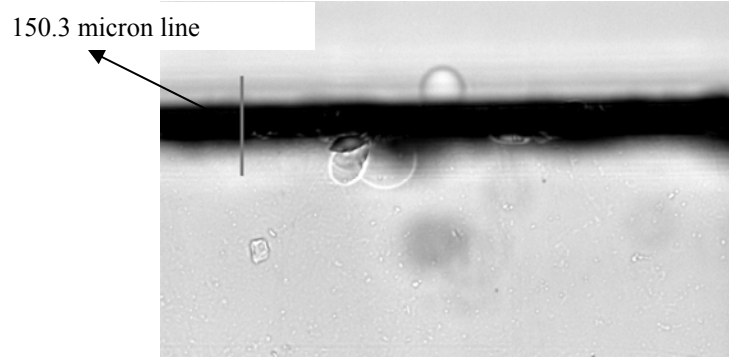
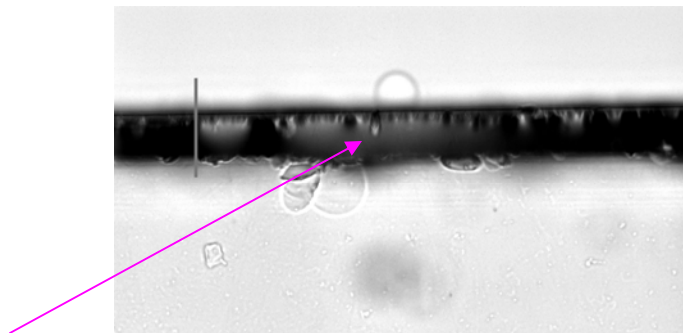
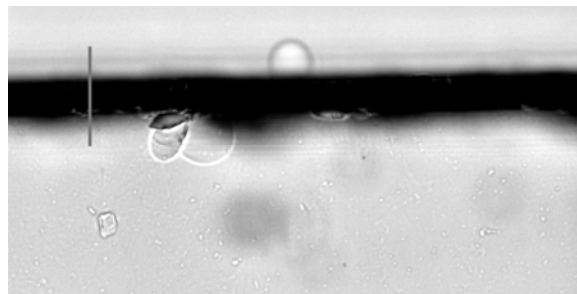


Figure 5.16: Here, the average edge-shadow width is 47.2 microns. The pale gray line is the 150.3 micron measuring guide.



The glass wafers are displaced by about 77.6 microns. Light area indicates space between the edges of the wafers.



The alignment pattern restores the wafers to give a shadow of average width of 53.4 microns. The difference in edge-shadow, and thus the alignment accuracy is about 6.2 microns.

Several trials were carried out to measure the alignment accuracy. In one such trial, the wafers were initially aligned, and an image was made as a reference.

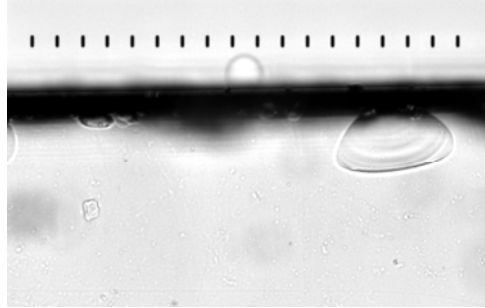


Figure 5.17: Guide marks were made, using Adobe Photoshop, on the image of the edge to aid in measurement of the edge shadow. For this initial alignment, the average width of the shadow was 50.51 microns. This image was made at 20x magnification.

The wafers were misaligned, and allowed to relax back into alignment. Images were taken after each relaxation time, approximately 2.5 seconds. In this trial, the wafer was misaligned four times, and images of the realigned edges were captured and measured.

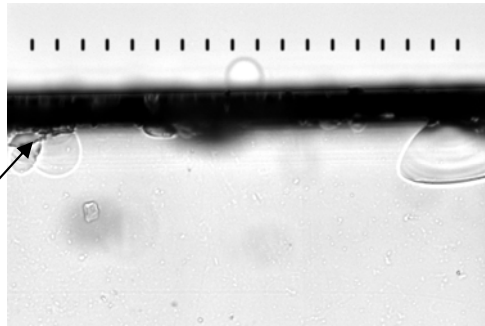


Figure 5.17: a) First realignment. The same guide marks were placed and measurements were taken in approximately the same places as the initial alignment image to get an idea of how well the pattern brings the wafers back to the original rest position. The placement of the guide marks is only approximate because the wafers shift during misalignment. The average shadow width is 59.14 microns.

Distinguishing features show were the wafers have shifted due to manual manipulation of misalignment.

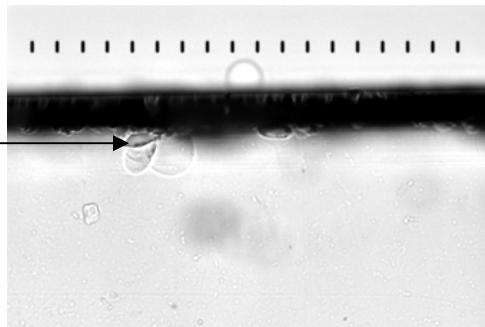


Figure 5.17: b) Second realignment. The average shadow width is 55.51 microns at relaxation.

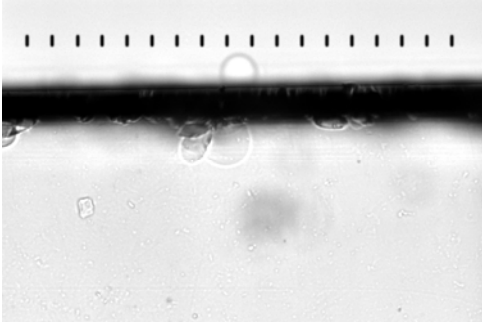


Figure 5.17.c: Third realignment. The average shadow width is 53.5 microns at relaxation.

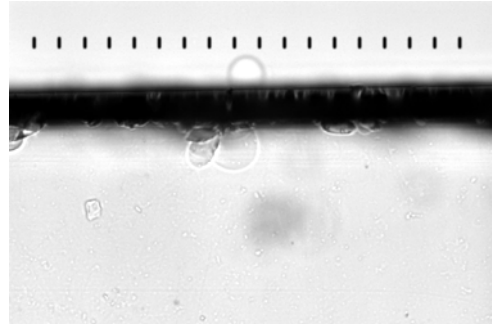


Figure 5.17.d: Fourth realignment. The average shadow width is 55.8 microns at relaxation.

The average difference in shadow width did not exceed 20 microns, which is within the tolerance stipulated by the spacing of the vias. In the graph below, the greatest differences in relaxation shadow were between the initial alignment and the first realignment, which had an average difference of 8.6 microns between shadow widths. Each subsequent realignment brought the edges back into better alignment, with average differences of 5.0 microns, 3.0 microns, and 5.3 microns.

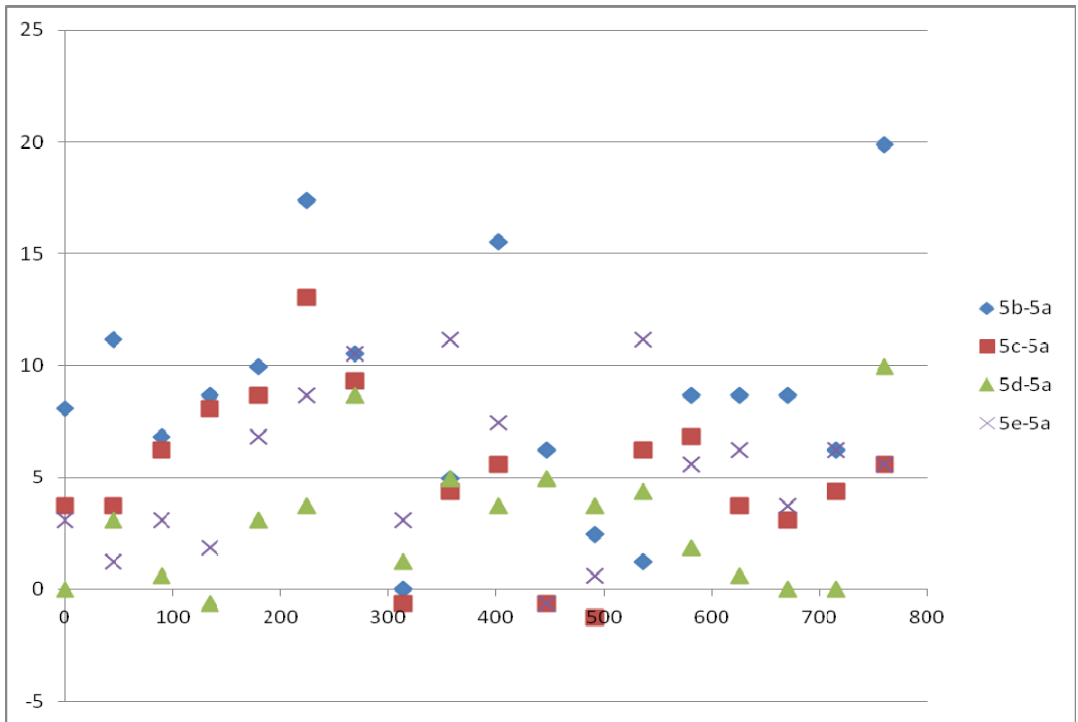


Figure 5.18: The spread of the difference in shadow widths was within the tolerance specified by the RF package design.

### 5.9: Combining Alignment and Covalent Nanoglue

In order to complete the package, the bonding would have to be accomplished as soon as the alignment takes place. Therefore, the alignment should use constituents that can be integrated into the wafer design. These constituents are SAMs layers, covalently bonded to the wafers, that will also be used in the bonding process. The bonding fluid will then also be the alignment fluid.

The SAMs constituents used in alignment are also used in bonding. SAMs adsorbed onto the wafer surfaces can be used to create the alignment pattern, and the alignment fluid can be used as the solvent for the nylon monomers necessary for bonding. A small weight can temporarily replace the clamp for the crystallization phase of the bonding, and when the

nylon salt, which forms a temporary ionic seal between the wafers, has formed, the clamp can be put into place for the polymerization phase.

Two wafers were successfully aligned and bonded, using only the carboxylic acid terminated SAMs. The PEDA may actually be superfluous, as the nylon monomers can as readily bond 10-UTS to itself as to the PEDA. However, because the alignment wafers were approximately the same size and shape, pulling these two wafers apart by the force table to determine the strength of the bond proved impossible. They could not be manually pried apart without assistance.

Future research should include the characterization and measurement of the integration package using IR optical technologies.



Figure 5.19: The integrated package using the alignment pattern and the nylon bonding two wafers with alignment patterns that have been successfully aligned and bonded.

## 5.10: Conclusion

One key to aligning wafers is the alignment pattern. The previous pattern had large capture areas in the center and finer details for the refinement of alignment at the edges. The current alignment pattern retains these features, but introduces the concept of large flow channels and an unlocking design to allow excess fluid to escape as alignment is achieved. These improvements have been shown to allow an alignment that falls within the tens of micrometer precision that is required by the original design specification of the RF package.

Another key to successful alignment is the materials used in creating the alignment patterns. The areas of hydrophilic and hydrophobic tendencies were made possible through the use of self-assembled monolayers, also specified by the design of the package. These SAMs, with modifiable functional groups in some cases, serve the dual purpose of facilitating alignment and integrating bonding materials.

The alignment pattern, as previously stated, was constructed in such a way that most of the angles were either  $45^\circ$  or  $90^\circ$  to the line of the moving edge of the wafer, if the wafers are displaced with the edges perpendicular to the applied force. The alignment pattern is meant to unlock, so that the fluid should escape once total alignment is complete.

## REFERENCES

- Adam, N. K. (1930). *Physics and Chemistry of Surfaces*. Oxford: The Clarendon Press.
- Ambrose, E.J., Elliott, A., and Temple, R. B. (1949). "The Use of Polarized Infra-Red Radiation in the Study of Doubly Oriented Long-Chain Polymers." *Proceedings of the Royal Society of London. Series A, Mathematical and Physical Sciences*. 199, 183-198.
- Benkart, P., Heittmann, A., Huebner, H., et al. (2005). "3D Chip Stack Technology Using Through-Chip Interconnections." *IEEE Design & Test of Computers*. 22.6, 512-518.
- Bettleheim, F., Brown, W., March, J. (2001). *Introduction to General, Organic and Biochemistry* (6<sup>th</sup> ed.). Australia: Brooks/Cole.
- Brady, J., Holum, J. (1981). *Fundamentals of Chemistry* (2<sup>nd</sup> ed.). New York: John Wiley and Sons.
- Brown, C. J. (1965). "Further Refinement of the Crystal Structure of Hexamethylenediammonium Adipate." *Acta. Cryst.* 185.
- Byung-Ho Jo, Linda M. Van Lerberghe, Kathleen M. Motsegood, and David J. Beebe, D. J. (2000). "Three-Dimensional Micro-Channel Fabrication in Polydimethylsiloxane (PDMS) Elastomer." *Journal of Microelectromechanical Systems*. vol. 9, no. 1.
- Caroti, G., Dusenbury, J. H. (1956). "Effect of drawing on the infrared dichroism of nylon 66 filaments." *Journal of Polymer Science*. 22, Issue 102, 399-407.
- Cassie, A. B. D.; Baxter, S. (1944). "Wettability of porous surfaces". *Transactions of the Faraday Society*. 40, 546.
- Davis, W. R., Wilson, J., et al. (2005). "Demystifying 3D ICs: The Pros and Cons of Going Vertical." *IEEE Design & Test of Computers*. 22.6, 498-510.
- De Gennes, P., Brochard-Wyart, F. Quere, D. (2002). *Capillary and Wetting Phenomena – Drops, Bubbles, Pearls, Waves*.
- Fourikis, Nicholas. (1997). *Phased Array-Based Systems and Applications*. New York: John Wiley and Sons, Inc.

- Fourikis, Nicholas. (2000). *Advanced Array Systems, Applications and RF Technologies*. San Diego: Academic Press.
- Goldstein, H. (1980). *Classical Mechanics*, (2<sup>nd</sup> Edition). Reading, Massachusetts: Addison-Wesley Publishing Company.
- Hallen, Hans. NSOM User's Manual. NCSU
- Halliday, D., Resnick, R., Walker, J. (1997). *Fundamentals of Physics*, (5<sup>th</sup> Edition). New York: John Wiley & Sons, Inc.
- Hirokawa, S., Ohashi, T., Nitta, I. (1954). "The Crystal Structure of some Polymethylenediammonium Adipates. I. Hexamethylenediammonium Adipate." *Acta Cryst.* 7, 87.
- Kittel, C. (2005). *Introduction to Solid State Physics*. (8<sup>th</sup> ed.) Berkeley: John Wiley and Sons.
- Lee, W., et al. (2006). "Design of T/R Module for the Wideband Active Array Antenna." *Antennas and Propagation International Symposium*. 863-866.
- Lu, A., Chua, K. M., Wai, L. L., Wang, J. J., Zhang, Y. P. (2004). "Integrated Antenna Module for Broadband Wireless Applications." *Electronics Packaging Technology Conference, 2004. EPTC 2004. Proceedings of 6<sup>th</sup>* Page(s): 240 - 243
- Macan, J., Bernardic, I., Orlic, S. (2006). "Thermal Degradation of Epoxy – Silica Organic – Inorganic Hybrid Materials." *Polymer Degradation and Stability*. 91, 122-127.
- Mailhot, B., Morlat-Therias, S., et al. (2005). "Study of the Degradation of an Epoxy/Amine Resin, 1 Photo- and Thermo-Chemical Mechanisms." *Macromolecular Chemistry and Physics*. 206, 575-584.
- Martin, B. R., Furnange, D. C., Jackson, T. N., Mallouk, T. E., Mayer, T. S. (2001). "Self-Alignment of Patterned Wafers Using Capillary Forces at a Water-Air Interface." *Advanced Fundamental Materials*. 11, No. 5, October.
- Moussessian, A., Del Castillo L., Edelstein, W., Hatake, T., Huang, J., Madsen, S. et al. (2005). "Transmit/Receive Membranes for Large Aperture Scanning Phase Arrays." *Antennas and Propagation Society International Symposium. 2005 IEEE* Volume 1A, Page(s): 330 – 333.
- Neiman, M. B., Kovarskaya, B. M., et al. (1962). "The Thermal Degradation of Some Epoxy Resins." *Journal of Polymer Science*. Vol. 56, 383-389.

- Netzer, L., Sagiv, J. (1983). *Journal of American Chemical Society*. 105, 674-676.
- Paul, M. A. (1962). *Physical Chemistry*. Boston: D. C. Heath and Company.
- Rubin, M. B. (2001). "The History of Ozone: The Schonbein Period, 1839-1868." *Bull. Hist. Chem.* 26 (1).
- Schwartz, D. K. (2001). "Mechanisms and Kinetics of Self-Assembled Monolayer Formation." *Annu. Rev. Phys. Chem.*
- Sharfrin, E. (1960). "Constitutive relations in the wetting of low energy surfaces and the theory of the retraction method of preparing monolayers." *The Journal of Physical Chemistry*. 64 (5): 519-524.
- Srinivasan, U., Liepmann, D., Howe, R. T. (2001). "Microstructure to Substrate Self-Assembly Using Capillary Forces." *Journal of Microelectromechanical Systems*, vol. 10, no. 1.
- Terfort, A., Bowden, N., Whitesides, G. M. (1997). "Three-dimensional Self-Assembly of Millimetre-Scale Components." *Nature*. 386, 162-164.
- Vazquez, G., Alvarez, E., Navaza, J. M. (1995). "Surface Tension of Alcohol + Water from 20 to 50 °C." *Journal of Chemical Engineering Data*. 40, 611-614.
- Von Gunten, U. (2003). "Ozonation of drinking water: Part I. Oxidation kinetics and product formation". *Water Res.* 37, 1443-1467.
- Von Gunten, U. (2003). "Ozonation of drinking water: Part II. Disinfection and By-product formation in presence of bromide, iodide and chlorine." *Water Res.* 37, 1469-1487.
- Walker, E. M. (2006). "Alignment of Silicon Wafers for 3D Packaging." North Carolina State University.
- Wasserman, S. R. (1989). "Structure and Reactivity of Alkylsiloxane Monolayers Formed by Reaction of Alkyltrichlorosilanes on Silicon Substrates." *Langmuir*. 5, 1074-1087.
- White, H. E. (1948). *Modern College Physics*. Van Nostrand.